PEOPLES' FRIENDSHIP UNIVERSITY OF RUSSIA NAMED AFTER PATRICE LUMUMBA

Federal State Budgetary Institution of Science

«Institute of Organic Chemistry. N. D. Zelinsky, Russian Academy of Sciences»

(IOC RAS)

As a manuscript

Dipheko Tshepo Duncan

Ethanol Conversion into Oxygenates Over K-modified, Co(Ni, Fe)-promoted MoS_2 Catalysts Supported on Activated Carbon Materials

Specialty:

1.4. 4. Physical Chemistry

Dissertation

For a PhD Degree in Chemical Sciences

Scientific Supervisor
Doctor of Chemical Sciences (Physical Chemistry)
Alexander G. Cherednichenko

Moscow 2023

РОССИЙСКИЙ УНИВЕРСИТЕТ ДРУЖБЫ НАРОДОВ ИМЕНИ ПАТРИСА ЛУМУМБЫ

Федеральное государственное бюджетное учреждение науки "ИНСТИТУТ ОРГАНИЧЕСКОЙ ХИМИИ ИМ. Н.Д. ЗЕЛИНСКОГО РОССИЙСКОЙ АКАДЕМИИ НАУК" (ИОХ РАН)

На правах рукописи

Дифеко Тшепо Дункан

Конверсия этанола в оксигенаты на K-модифицированных Co(Ni, Fe)-MoS_2 катализаторах, нанесенных на углеродных носители

Специальность
1.4. 4. Физическая Химия

Диссертация
на соискание ученой степени
кандидата химических наук

Научный руководитель
доктор химических наук (физическая химия)
Чередниченко Александр Генрихович

Москва, 2023г

TABLE OF CONTENTS

INTRODUCTION

Relevance of the research topic

The significant increase in global energy consumption, greenhouse gas emissions, and global warming caused by the usage of fossil fuels is driving ongoing research into alternative and renewable fuels with minimal environmental effects. Furthermore, current energy dependency on fossil fuels causes significant instability in the global market since worldwide stocks of fossil fuels are depleting, resulting in relative price volatility. Currently, ethanol is seen as a potential rival to those generated from fossil fuels, and it is considered one of the finest biofuels for transportation. It may, in fact, be used directly or blended with gasoline to enhance fuel combustion in transportation, resulting in fewer CO_2 emissions and lowering greenhouse gas emissions in the environment. Additionally, ethanol is not only regarded as a superior fuel but also as a very versatile chemical product. It is a vital raw material for both food processing and the manufacture of chemical products, and it is especially significant in the pharmaceutical industry. Its uses are growing every day, and it has become a key part of research around the world.

The development of appropriate catalysts, the type of support and promoter materials, and the operating conditions for ethanol conversion to improve oxygenate yields and selectivity have all attracted interest. The influence of non-noble promoter atoms on ethanol dehydrogenation has been explored. Conventionally, ethanol dehydrogenation is primarily carried out over Cu-based catalysts because of their high selectivity for dehydrogenation products. Nonetheless, the application of Cu-catalysts is often restricted by their rapid deactivation, mostly generated by sintering due to the relatively low melting point of Cu metal and, to a lesser extent, sulfur poisoning. This property makes them especially unsuitable for sulfur-containing feedstocks and other alternative hydrocarbon sources. Furthermore, additional ethanol dehydrogenation catalysts to produce oxygenated hydrocarbons include metals (Pd, Rh, Pt, and Ru) based on alumina. However, because platinum group metals are more expensive, alternative catalytic systems based on non-noble metal catalysts have been developed. Co and Ni non-noble metal-based catalysts, on the other hand, are gaining traction owing to their inexpensive cost and enhanced catalytic activity.

Catalytic systems such as MoS_2 have therefore been shown to be a viable alternative to noble metals in various processes such as hydrogen evolution, higher alcohol synthesis (HAS), and other oxygenated hydrocarbon synthesis. Metal sulfides are a low-cost alternative that can be highly robust, sulfur-tolerant, and simple to recycle and/or reactivate given the right reaction conditions, making (Co) MoS_2-based catalysts intriguing for a renewable and/or post-peak oil economy. In addition, unlike other catalytic systems, sulfide catalysts are more resistant to CO_2 attack, have high activity for the water-gas shift (WGS) reaction, and have a substantial tolerance to coke deposition.

To date, there is no reliable data on supported transition metal sulfides, K-(Me)MoS_2 as a catalytic system for the ethanol dehydrogenation reaction (where Me = Co, Ni or Fe). The insight into the reactions of ethanol on MoS_2 can open the door to a new set of intriguing ethanol transformations, including dehydrogenation and dehydrogenative coupling. Leading to the investigation of the role of support, promoter atoms, and catalyst textural properties on catalytic activity, conversion, and product distribution.

The aim of the work is to synthesize novel modified and promoted MoS_2 catalysts on various carbon-containing materials, as well as to clarify the effect of their structure and properties on the efficiency of the ethanol conversion process into oxygenated products. To achieve this goal, it is necessary to solve the following tasks:

1. Synthesize noval modified and promoted K-(Me)MoS_2 (where Me = Co, Ni, or Fe) catalysts on various carbon-containing supports.

2. To study the structure and properties of catalysts based on K-(Me)MoS_2 using energy dispersive X-ray analysis (EDX), scanning electron microscopy (SEM), high-resolution transmission electron microscopy (HRTEM), low-temperature adsorption-desorption of N_2, X-ray photoelectron spectroscopy (XPS), X-ray fluorescence analysis (XRF), and other methods of physicochemical studies.

3. To investigate the influence of the nature of the promoter metal on the catalytic activity of K-(Me)MoS_2 catalysts in the presence and absence of a modifier to establish the composition-properties-activity relationship in ethanol conversion reactions.

4. To study the influence of the properties of the catalyst, including the acidity of the support and its textural properties, on the catalytic characteristics and the formation of promoted and modified MoS_2.

5. To investigate the effect of an inert and reactive atmosphere (i.e., He and H_2) on the yield of various oxygenates in the ethanol conversion reaction using catalysts based on K-(Me)MoS_2.

6. To present and justify the general scheme of chemical transformations of ethanol into various products, including oxygenates, using heterogeneous catalysts based on K-(Me)MoS_2.

Scientific novelty

1. For the first time, a comprehensive study of MoS_2-based catalysts promoted by transition metals, as well as potassium-modified (K-modified) catalysts deposited on commercial activated carbons (AC) in the ethanol conversion reaction was carried out.

2. K-(Me)MoS_2 catalysts supported on AC have shown significant reactivity towards ethanol conversion.

3. It has been established that the main processes of ethanol conversion are dehydrogenation (synthesis of acetaldehyde and ethyl acetate), condensation (ethyl acetoacetate), and dehydration/hydrogenation (i.e., formation of ethylene, ethane, and diethyl ether), and modification with K and Co (Ni, Fe) contributes to a higher yield of C_{3+} alcohols by reducing the proportion of hydrocarbons.

4. It was found that catalysts on the supports with a high content of micropores were more active in the ethanol conversion reaction than catalysts on a mesoporous support.

5. The influence of the acidic properties of the surface on the morphology of promoted and modified MoS_2 crystallites has been established. It is shown that high acidity reduces the activity of catalysts.

6. A general scheme of the process of ethanol conversion into final products using K-(Me)MoS_2 catalysts is proposed.

Theoretical and practical significance

Based on a comprehensive study of the influence of the nature and morphology of the carrier on the structure and catalytic properties of the active phase, effective catalysts for the synthesis of various oxygenates from ethanol based on MoS_2, promoted by Co, Ni, Fe and modified K, deposited on various carbon materials, were developed. The developed catalysts have shown high efficiency, stability, and resistance to sulfur poisoning. In addition, their increased resistance to CO_2 and coke deposition compared to other known catalysts was noted.

Methodology and research methods

Several techniques were used to study the characteristics of the tested catalysts. The textural properties of supports and sulfide catalysts were studied by low-temperature nitrogen adsorption on an Autosorb 1 (Quantachrome) porometer. The morphology of supports and sulfide catalysts was studied using a scanning electron microscope (SEM) and a transmission electron microscope (TEM). Chemical composition of the surface of catalysts K-(Me)MoS_2 was studied using X-ray photoelectron spectroscopy (XPS). The acid-base characteristics of supports and sulfide catalysts were determined by UV spectrometry by pyridine adsorption. X-ray fluorescence analysis was performed on a Shimadzu EDX-7000 spectrometer to determine the elemental composition of sulfide catalysts. Studies of the gaseous and liquid components of synthesis were carried out using gas chromatography.

Provisions submitted for defense

1. Synthesis, investigation of the composition, structure and properties of catalysts based on modified, and promoted MoS_2 for the synthesis of various oxygenated hydrocarbons from ethanol.

2. Results of studying the effect of various granular and fibrous carbon-based carriers on the catalytic properties of the studied catalysts for ethanol conversion.

3. Investigation of the effect of Co, Ni, Fe promoters, and K-modifier on the activity of a MoS_2-based catalyst.

4. Results of the influence of the reaction atmosphere and other conditions on the technological characteristics of ethanol conversion using catalysts based on modified and promoted MoS_2.

5. Influence of textural properties of carriers and properties of synthesized MoS_2 catalysts on their efficiency in the conversion of ethanol into various oxygenated hydrocarbons.

Reliability

The use of advanced analytical procedures and modern equipment available at the Peoples' Friendship University of Russia named after Patrice Lumumba in cooperation with the Zelinsky Institute of Organic Chemistry of the Russian Academy of Sciences ensures the accuracy and reliability of the results. In addition, the reproducibility of the results and their consistency with each other, as well as with literary studies, confirm the accuracy of the results.

Author's personal contribution

The author was engaged in the search, analysis, and generalization of literary data on the subject of the work. Directly participated in the setting of goals and objectives in this work. Independently carried out the synthesis, testing, and testing of catalytic samples in the conversion of ethanol on high-pressure flow catalytic units and the analysis of the data obtained. Together with the supervisor, I carried out the analysis of the obtained data and their generalization. Actively participated in writing scientific articles. The results of scientific work were reported at domestic and international conferences.

Approbation of the work

The main results of the dissertation work were presented at international conferences: International scientific conference «Catalysis for a Sustainable World», RUDN, Moscow, Russia, 15–18 December 2020; 10th Edition of Global Conference on Catalysis, Chemical Engineering & Technology, Chicago, IL 60606, USA, 28 – 30 March 2022; International Scientific Conference Advances in Synthesis and Complexing». RUDN, Moscow, Russia, 26–30 September 2022; 11th Edition of International Conference on Catalysis «Chemical

Engineering and Technology». Japan, 16–17 May 2022; III Interuniversity Conference of Young scientists with international participation "New materials and chemical technologies". Moscow, Russia, December 26 – 27, 2022. P. 181 – 182.

Completeness of the materials presentation

On the topic related to this research dissertation, 4 articles were published (in international peer-reviewed journals, Scopus and/or WoS databases), 1 in Russian Science Citation Index (РИНЦ) and 9 abstracts of reports in international conferences.

Structure and scope of the dissertation

The dissertation consists of an introduction, a review of the literature, a description of the objects and methods of research, results and their discussion, conclusions, and a list of references. The work is presented on 141 pages, including 32 figures and 11 tables. The list of references contains 181 titles.

CHAPTER 1: Literature Review

This chapter's contribution to the entire study

This chapter offers a summary of the sources of ethanol production prior to actually discussing the various techniques of converting ethanol into value-added chemicals such as aldehyde, esters, C_{3+} alcohol, and other valuable compounds. The significance of various commodities and specialty chemicals is highlighted.

1.1 Background

1.1.1 Ethanol as Fuel and Fuel Additives

Fossil fuels are employed to meet energy demands and to produce chemicals that enhance our quality of life. The excessive utilization of fossil fuels resulted in their exhaustion and concerns regarding the phenomenon of global warming. Efforts have been undertaken in recent decades to find a sustainable method for synthesizing various compounds from renewable resources, as a means of addressing the drawbacks associated with fossil raw materials. Biomass is considered a dependable alternative to fossil-based raw materials in the manufacture of fuels and chemicals, according to this perspective [1]. A diverse array of biomasses is readily accessible on a substantial scale and is economically comparable to petroleum in terms of mass, energy, and price, utilizing current, projected, and established technologies. Renewable energy sources are characterized by their abundance, accessibility, and reduced greenhouse gas emissions during consumption. Consequently, it demonstrates a diminished influence on the ecosystem and generates commodities through ecologically sustainable means [2].

1.1.1.1 Ethanol Conversion

Ethanol, a compound derived from biomass, is regarded as a highly valuable molecule owing to its numerous applications. Bioethanol is a widely recognized fuel source that is generated through the process of fermentation of diverse forms of edible refuse. However, growing apprehensions regarding the future food supply and natural systems have propelled the production of biofuels from non-food waste feedstocks. In

contrast, ethanol is extensively employed for the purpose of blending with gasoline owing to its elevated research octane number, negligible environmental toxicity, and commensurate energy content. The blending of ethanol has the potential to reduce petroleum consumption by 5-27% [3][4]. However, The addition of ethanol or methanol to gasoline results in a substantial increase in the vapor pressure of the resulting fuel. This is considered to be the primary disadvantage of utilizing alcohols with lower molecular masses [5][6].

It is expected that ethanol will be employed for the production of industrially significant compounds, which are presently derived from non-renewable sources. These compounds include acetaldehyde, ethyl acetate, butanol, acetone, ethylene, diethyl ether, and other oxygenated hydrocarbons. The escalation of ethanol production and its regulated blending ratio with gasoline are driving forces that underpin its utilization as an eco-friendly resource for the generation of fuels and high-value derivatives [7][8].

1.1.2 Ethanol-derived Chemicals

Ethanol is an excellent renewable feedstock since it can be transformed into a wide range of end products, including acetaldehyde, ethyl acetate, butanol, ethylene, and other light hydrocarbons and oxygenated hydrocarbons. The catalytic synthesis of acetaldehyde from ethanol is a crucial intermediate. Acetaldehyde is a versatile chemical that may be used to synthesize acetic acid, ethyl acetate, acetic anhydride, n-butanol, crotonaldehyde, ethyl acetate, and many more compounds [9]. Acetaldehyde synthesis from ethanol eliminates the concerns of hydrocarbon oxidation since ethanol is naturally oxygenated.

Historically, the production of acetaldehyde involved the hydration of acetylene with vinyl alcohol, leading to the tautomerization of the latter into acetaldehyde [1]. Sulfuric acid was frequently employed as a catalyst in this particular procedure. During the 1960s, the decrease in the cost of ethylene prompted its utilization as a primary component in the production of acetaldehyde. Under these conditions, acetaldehyde is generated through two distinct processes: the conversion of ethylene to ethanol followed by its dehydrogenation, or the partial oxidation of ethanol using air over a silver gauze

catalyst to yield acetaldehyde. Currently, the Wacker process is the predominant technique employed to produce acetaldehyde. This method involves the direct oxidation of ethylene to acetaldehyde, utilizing palladium or copper chlorides as catalysts. In contrast, the Wacker process generates chlorinated waste, necessitates higher energy consumption for air filtration and wastewater treatment, and mandates the utilization of expensive titanium for reactor tubing [10]. The process of dehydrogenation of ethanol, whether with or without the inclusion of air, has been found to be advantageous from both an ecological and economic standpoint in the synthesis of acetaldehyde. The increasing demand for direct ethanol transformation necessitates the development of innovative synthesis techniques and improved heterogeneous catalysts.

Ethyl acetate is a commonly employed solvent in various industrial applications. The process of industrial synthesis involves three main steps: firstly, the esterification of ethanol and acetic acid; secondly, the interaction of acetic acid with ethylene; and finally, the Tishchenko reaction, which involves the disproportionation of acetaldehydes. Nevertheless, the deleterious effects of the chemical agents employed represent the primary limitations of these techniques. The process of synthesizing ethyl acetate involves the conversion of ethanol through a one-step reaction. The proposed approach is a viable option that is advantageous from both an ecological and financial perspective. The production process involves oxidative and dehydrogenative reactions. The process of oxidation yields a total of two moles of water molecules, whereas the dehydrogenation pathway results in the production of hydrogen. The process of dehydrogenation is deemed to have greater economic significance due to its ability to generate hydrogen as a byproduct, without the need for oxygen, thereby averting the possibility of combustible mixtures [11]. The task of isolating products from reaction mixtures poses a considerable obstacle for both procedures.

Butanol is a multifaceted commodity chemical that finds its application in the production of acrylic esters and acrylic acid. It is also employed as a gasoline additive and a solvent. Due to its superior energy density, increased air-to-fuel ratio, reduced water solubility, and lower vaporization heat, it is classified as a biofuel according to sources

[12][13][14]. The commercial synthesis of butanol involves the oxo process, which involves two steps: (i) hydroformylation of propylene to yield butyraldehyde and (ii) hydrogenation of butyraldehyde to yield butanol [14][15]. The challenges associated with product separation, the significant cost involved in catalyst production, and the adverse environmental impacts represent the sole limitations of this methodology. Therefore, the conversion of ethanol to butanol appears to be a more favorable option. There exist two distinct chemical pathways for the synthesis of butanol: (i) the direct dimerization of two ethanol molecules and (ii) a multistep Guerbet process. The process of ethanol dehydrogenation leads to the formation of acetaldehyde, which is then subjected to hydrogenation to yield crotonaldehyde via self-aldol condensation of acetaldehyde [12][16].

Ethylene is a fundamental chemical compound that serves as a crucial building block in the synthesis of various polymers, including polyethylene, polyvinylchloride, and polystyrene. Additionally, it is utilized in the production of ethylene glycol, ethylene oxide, ethyl benzene, and an array of other chemical compounds. The process of thermal cracking of petroleum feedstocks is primarily responsible for its production. Nevertheless, these procedures consume a substantial amount of energy and emit a significant quantity of greenhouse gases. Bioethylene is produced through the dehydration of bioethanol with the aim of reducing the emission of greenhouse gases. The escalating depletion of fossil fuel reserves has resulted in a surge in the cost of ethylene. The conversion of bioethanol to ethylene is becoming increasingly attractive and feasible due to its potential for enhancing throughput and reducing costs [17].

Despite numerous studies on the conversion of ethanol into value-added chemicals, there are still challenges to be addressed, including the reported reduced time on stream for most catalytic systems. Tailored catalysts possess the capability to augment carbon yield in the context of hydrocarbon reactions. When dealing with unstable intermediates, it is possible to utilize catalyst design alternatives to enhance the production yields. The catalyst's efficiency should prioritize the selectivity of the desired product. The utilization of reaction chemistry has the potential to yield substantial substitutes for fossil fuel

resources, leading to the production of commodities that exhibit enhanced longevity and superior cleanliness in comparison to those currently obtainable from traditional sources. Studies have been conducted to explore the potential of MoS_2-based catalysts in ethanol reactions, with the aim of enabling novel transformations such as dehydrogenation and dehydrogenative coupling.

1.2 Transition Metal Sulfides Catalysts, MoS_2

The active phase in various heterogeneous catalytic processes, such as the hydrodesulfurization (HDS) process utilized in the removal of impurities during crude oil refining and higher alcohol synthesis, comprises of MoS_2 nanoclusters. The catalysts under consideration contain the MoS_2 phase in the form of either single or stacked layers of MoS_2. The catalytic activity of MoS_2 layers is commonly attributed to the inertness of the MoS_2 basal plane, which results in catalytic activity being primarily localized at the edges. The optimization of edge accessibility holds significant importance in the preparation of catalysts.

1.2.1 MoS_2 Structural Model

Transition metal sulfides (TMS), specifically materials based on MoS2, have been employed in hydrotreating processes to improve the quality of petroleum since the conclusion of World War II. The utilization of MoS2 in hydrotreatment processes could potentially serve as an initial indication of its versatility and resilience in the face of elevated reaction conditions. According to reference 18, MoS2 has the ability to carry out hydrodesulfurization (HDS), hydrodenitrogenation (HDN), hydrogenation (HYD), and hydrodeoxygenation (HDO) on diverse substrates with the aim of enhancing the cetane number and eliminating impurities from fuels [18].

The complex nature of reactant profiles in applied hydrotreatment processes has led to the examination of model reactions on MoS_2, which has provided valuable understanding of the mechanism and active catalytic site. Efforts to comprehend the fundamental origins of reactivity on MoS_2 have indicated that the surface area, as

evaluated through N_2 physisorption, is an inadequate parameter for normalizing reactivity information [19] on MoS_2 and similar substances. The accuracy of this statement cannot be generalized to all sulfides due to the considerable structural heterogeneity exhibited by TMS. The cubic structure of RuS_2 exhibits isotropy, and its reactivity is commensurate with its surface area, as reported in reference [20]. However, MoS_2 displays significant anisotropy, and its reactivity is influenced by this property in a manner that cannot be accounted for solely by its surface area. It is widely acknowledged that all remaining TMS catalysts are positioned along a continuum that spans between the aforementioned geometric endpoints. The HDS reactivity throughout the periodic table is demonstrated by volcano charts [21], indicating that the choice of transition metal has the most significant impact. The aforementioned phenomenon exhibited a correlation with the fluctuating intensity of the metal-sulfur linkage, which is subject to alteration based on the position of the element in the periodic table. The study concluded that an optimal intermediate strength of metal-sulfur bonding was necessary to facilitate the creation of sulfur vacancies [22] or coordinatively unsaturated (CUS) metal sites on the sulfide surface, which can serve as sites for substrate adsorption.

The identification of transition metals has a significant impact on reactivity. However, it is crucial to comprehend the geometric and chemical consequences to enhance reactivity on a particular TMS and establish the active site prerequisites in a broader sense. Multilayer dichalcogenides, including MoS_2, are comprised of platelets consisting of Mo-S. Platelets at the individual level consist of Mo-S sandwiches that are bonded through Van der Waals forces, which is the fundamental reason behind the initial use of MoS_2 as a solid lubricant. Following the observation that N_2 physisorption did not exhibit significant associations between reactivity and physisorption, a hypothesis was formulated positing that the extensive basal planes of MoS_2 were inert, and that solely the edges of the platelets contained active material. The results of chemisorption investigations involving O_2 indicate that the basal plane of MoS_2 does not exhibit chemisorption of O_2, but rather the edges of the slabs. Additional techniques that specifically focus on the edges were utilized to establish a relationship between the

structure and function. The most reactive feature of the material was determined through the utilization of electron spin resonance [23], magnetic susceptibility, and photodeflection spectroscopy techniques. The results indicated that the edges exhibited the highest level of reactivity. Several studies conducted on individual crystals, where the ratio between the basal plane and edge plane was either known or regulated, have demonstrated that chemical reactivity takes place in the vicinity of the edges. The challenge of correlating N_2-physisorption data with granular sample reactivity is attributed to the incapacity to anticipate or regulate the proportion of basal plane to edge plane areas in nanoparticulate MoS_2. The complexity of the matter is compounded by the fact that the term "edge" in this particular context does not necessarily pertain to the boundaries of the slab. The occurrence of local anisotropy resulting from bending, folding, or uneven layer termination can induce a local structure resembling a "edge" in small domains on the basal plane. This can lead to the emergence of "edge"-like reactivity in unexpected locations.

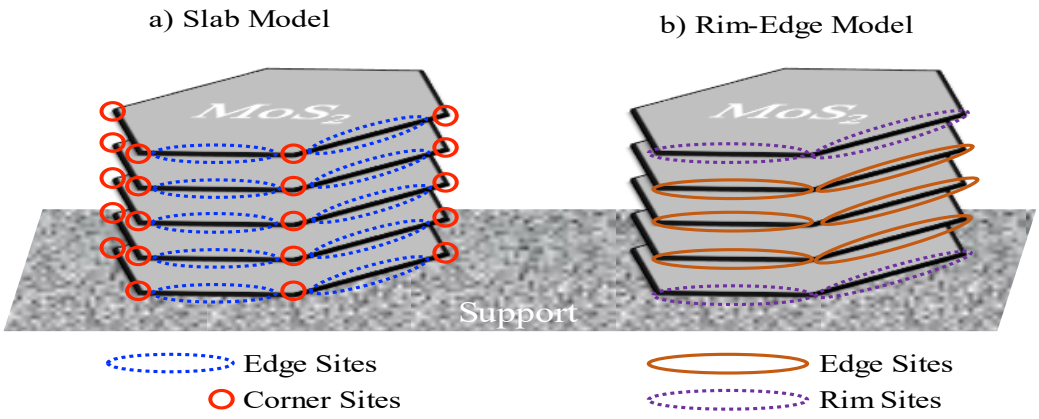

Figure 1.1. MoS_2 active sites are shown in two prominent geometric models. Both the a) Slab Model and b) the "Rim-Edge Model" [19]

The heightened stringency of pollution regulations during the 1990s prompted a notable upswing in the investigation and implementation of MoS_2 on a more extensive basis [24]. After the disclosure that hydrotreating activity is more probable to take place at the edges rather than in the basal planes, the subsequent measure was to determine the particular circumstances along these edges that function as active sites for the procedure. A geometric model for MoS_2 in its active phase was constructed utilizing slabs that

exhibited diverse Mo/S-atom geometries at the edge, corner, and basal plane, as described in reference [25]. As per this theoretical framework, the emergence of sulfur vacancies at the edges could potentially give rise to localized anisotropy. In order to preserve the neutral charge of the membrane's edges, it is imperative to have the presence of -SH groups, $^{-}$OH and O^{2-} groups, as well as Mo^{3+} and Mo^{2+} atoms. The species situated in the vicinity of sulfur vacancies pose a challenge or may even be unfeasible to quantify directly due to their limited quantities. The study involved the generation of slabs with diverse geometries to determine the optimal method of filling the edges and corners of each slab with anisotropic sites of varying types. A correlation has been identified between the reactivity of authentic MoS_2 samples and their anticipated edge and corner site populations. **Figure 1.1a** depicts the graphical representation of the Slab Model.

An additional geometric theory posits that the platelet perimeters located on the upper and lower strata of a platelet aggregate elicit dissimilar impacts compared to the platelet boundaries. The visual representation of the "Rim-Edge" Model [19] is illustrated in **Figure 1.1b**. In pursuit of this objective, MoS_3 samples lacking a definite shape were subjected to incremental heating in a sulfuric milieu, leading to the production of MoS_2 samples with differing stack heights. After undergoing hydrotreating, the specimens were subjected to dibenzothiophene (DBT) in order to evaluate their preference for hydrogenation over hydrodesulfurization. The study reveals that the hydrodesulfurization process of DBT exhibits a higher rate at rim sites compared to edge sites, as evidenced by the augmented selectivity for hydrodesulfurization in specimens featuring greater quantities of rim-sites. The site preference may not have an impact on smaller molecules. The researchers suggest that for specimens with limited stacking heights, the Slab Model and the Rim-Edge Model could be utilized.

1.2.2 Active Phase and Active Sites MoS_2-based Catalysts

The active phases of unpromoted Mo (W) sulfide catalysts during hydrogenation and hydrogenolysis are known to be CUS around the edges and corners of MoS_2 (WS_2) structures (seen in **Figure 1.2**).

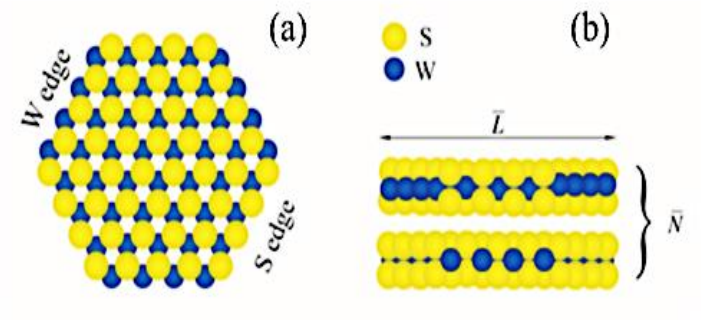

Figure 1.2. Ball model of a WS_2: (a) top view and (b) side view [26].

Various structural models have been developed to describe the active phases of molybdenum catalysts supported by Co(Ni), as reported in [27][28][29]. According to the intercalation model, the primary composition of MoS_2 structures consists of slabs that comprise a layer of Mo (W) atoms situated between two hexagonal planes of densely packed S atoms. Within the interlayer region of van der Waals gaps, octahedral intercalation sites are occupied by promoter Co (Ni) ions. The theoretical framework known as the "pseudointercalation model" is predicated upon the structural composition of bulk MoS_2, wherein sulfur atoms are arranged in a prismatic configuration surrounding each individual molybdenum atom. The intercalation of Co or Ni promoters occurs within the octahedral voids situated between the S-Mo-S layers located at the edge of the crystallite. The "contact synergy model" demonstrates the prevalence of Co_9S_8 and MoS_2 in unsupported CoMo catalysts. The contact between the two phases was attributed a co-promotional role. The phenomenon of contact synergism has been elucidated through the mechanism of hydrogen spillover originating from Co_9S_8 and MoS_2. The prevalent model in the field is the "Co-Mo-S model," which involves the presence of Co-Mo-S phases characterized by MoS_2-like structures. These structures contain promoter atoms situated at the edges of the S-Mo-S layers. The Co-Mo/Al_2O_3 catalyst features the Co-Mo-S phase, wherein Co atoms are situated at the edge positions of MoS_2 in the "Co-Mo-S model". Two distinct "Co-Mo-S type" phases exhibiting varying catalytic abilities were identified based on factors such as preparation and activation conditions, support type, and the presence of additives. The Type-I Co-Mo-S exhibits a singular slab configuration that

manifests a robust interaction with the substrate via Mo-O-Al bonds at the periphery, which pose a challenge for complete sulfidation. Type II comprises multiple slabs exhibiting weaker support interactions and higher degrees of metal sulfidation. It is widely acknowledged that Type II structures exhibit higher levels of catalytic activity in comparison to Type I structures. Following sulfidation, cobalt can exist in three distinct forms, namely Co_9S_8 crystallites on the support, Co atoms on the edges of MoS_2 crystallites (Co-Mo-S phase), and cobalt cations Co^{2+} in octahedral or tetrahedral locations in the Al_2O_3 phase (as depicted in **Figure 1.3**).

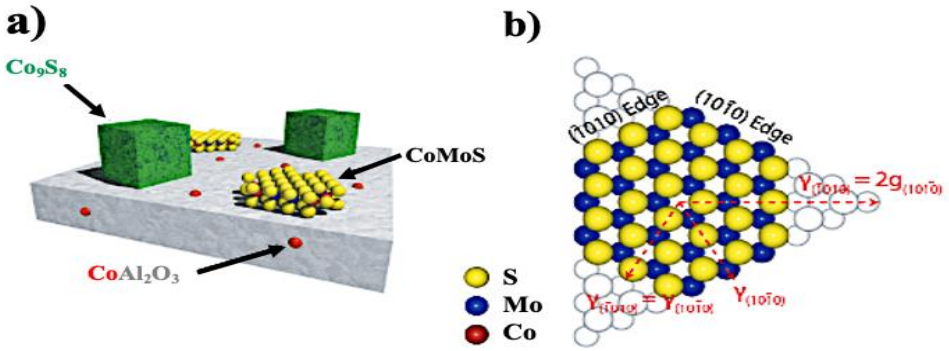

Figure 1.3. a) the three different phases of Co, b) ball model of MoS_2. Cobalt is also found in excess in two additional phases: cobalt sulfide Co_9S_8 and a $Co:Al_2O_3$ spinel structure in which Co is integrated into the aluminum support [30].

1.2.3 Non-promoted MoS_2

Several studies have been conducted to assess the comparative effectiveness of non-promoted MoS_2 with promoted systems. Based on an extensive analysis of the literature, it has been determined that the active phase of HDT catalysts comprises of nano-layers of MoS_2 [31]. The visual representation depicted in **Figure 1.4** illustrates the presence of a MoS_2 nanolayer, which can be observed as a singular sheet with restricted dimensions (approximately 30-40 Å) dispersed across the surface of alumina. The accurate definition of the unpromoted MoS_2 nanolayer has been a challenging task and has been extensively investigated through comparative analyses with promoted systems [32][33]. When attempting to construct a fundamental molecular model for the finite-sized single sheet of

MoS_2 from bulk MoS_2 [34], the initial concern to address is the characteristics of the stable atomic edges that terminate the MoS_2 sheet under HDT conditions. As per the principles of crystallography, the generation of edges can be infinite due to crystallographic orientations. In practical applications, the stability of two edges, namely the (10-10) molybdenum edge (hereinafter referred to as the "M-edge") and the (-1010) sulphur edge ("S-edge"), can be attributed to their energetic competition. The statement suggests that the 2D morphology may undergo a cyclic transformation between a triangular shape, a hexagonal shape, and a deformed hexagonal shape, contingent upon the comparative energy levels of the two edges [35]. Furthermore, the (001) basal plane, which serves as a capping layer for the two-dimensional structures, is rendered stable. The aircraft in question is fabricated through the process of "slicing" van der Waals interactions, which serve to uphold the coherence of the stacked layers constituting the bulk structure [33].

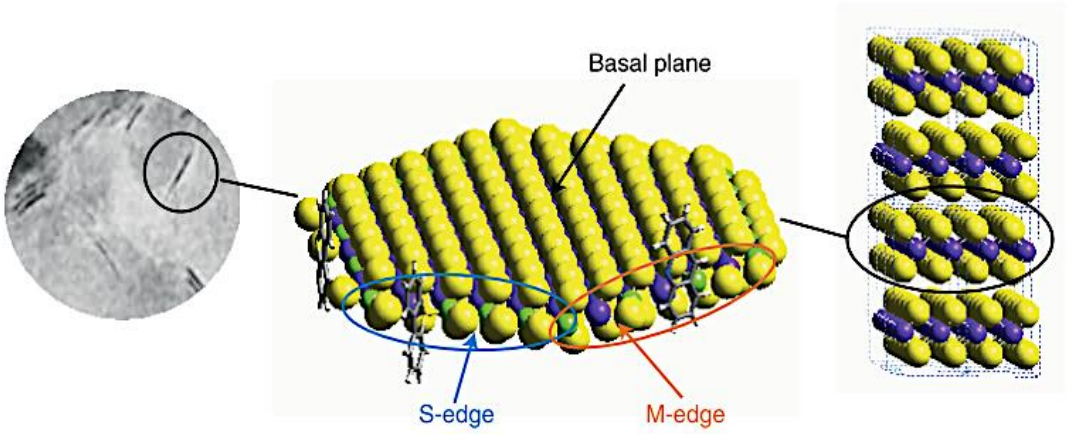

Figure 1.4. TEM picture of a Co(Ni)MoS active phase supported on alumina (left). Model of a single Co(Ni)MoS nano-layer (stacking equal to 1) with a two-dimensional morphology (centre). Structure of MoS_2 with an unlimited number of stacked layers (right). Colour key: S (yellow), Mo (pupil), and Co (green).

DFT calculations demonstrate the electrical and structural properties of these two edges (the Mo-edge and the S-edge). The electronic properties of the coordinatively unsaturated Mo-edge sites (also known as "CUS") are proposed by examining the predicted density of states around the Fermi energy. The bulk semiconducting gap narrows at unsaturated surface regions. The metallic character of the Mo-site and the back-

donation into the 2π* antibonding orbital of CO are caused by occupied d-states at the Fermi-energy level [31][36]. The high adsorption energies of electron-donating species such as sulfur atoms and thiophene molecules near the Mo-edge, where unsaturated Mo-sites operate as Lewis sites, are caused by unoccupied d-states right above the Fermi level.

The stability of MoS_2 slab edges in the presence of H_2, H_2S, and H_2/H_2S is a significant area of concern in the field of sulfide catalysis, given the active centers' inherent properties. Multiple research investigations [3–6] have demonstrated the instability of these rims during reaction conditions. The reaction between hydrogen and sulfur situated on S rims may result in the formation of anion vacancies or CUS-Mo-atoms, while hydrogen sulfide can dissociate on CUS molybdenum Mo rims. **Figure 1.5** illustrates the CUS formation pathway on MoS_2/Al_2O_3 catalysts. The process entails the dissociative adsorption of a hydrogen molecule on the metallic edge of a surface of MoS_2 crystallite, which is then succeeded by the creation of a CUS through the discharge of a solitary H_2S molecule into the gaseous phase. This has been documented in sources [1,2][37]. Furthermore, the authors posit that a comparable methodology could be employed to generate a dual vacancy. There are two potential pathways that could be involved in the creation of CUS on the sulfur edge. The initial phenomenon pertains to an intramolecular rearrangement of the surface, wherein no H_2S molecules undergo elimination.

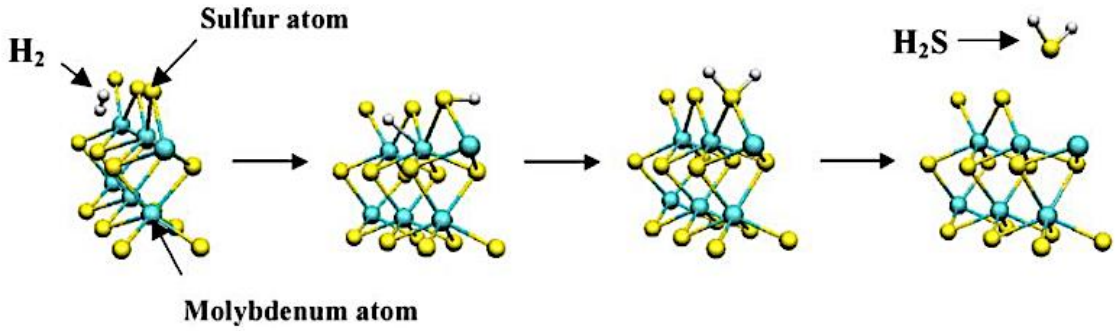

Figure 1.5. Mechanism of CUS formation on MoS_2. Abducted from [37]. Colour Keys: S (yellow), Mo (blue), H (white)

1.3 Effect of Alkali Metal

The utilization of alkali metals in heterogeneous catalysis is widespread for the purpose of modifying the activity and selectivity of various processes [38]. As per the author's assertion, the utilization of alkali has the potential to enhance selectivity or specificity, improve activity, and prolong the operational longevity of catalysts. The catalyst that lacks alkali demonstrates a selectivity of below 50% in regards to the production of ethylene oxide via the reaction of ethylene and oxygen. The catalyst's selectivity is enhanced as the alkali concentration increases, as reported in [39]. The impact of an overabundance of alkali doping on reactivity is moderate in the case of lithium and reaches its maximum potential with cesium. The selectivity of the atomic weight of the alkali metal increases when the catalyst is appropriately promoted. The alkali metal is frequently involved in the process. Methanol is the exclusive product resulting from the reaction of CO and H in the presence of a zinc-chromium catalyst under pressure. In the event that the catalyst comprises alkali, a greater quantity of alcohols is produced. The concentration of higher alcohols exhibits an increase in the presence of Li, Na, K, Rb, and Cs. According to previous research [38], the introduction of Li, Na, or K as promoters has been observed to decrease catalytic activity, whereas the presence of Rb or Cs has no effect on catalytic activity. The introduction of alkali into the low-temperature methanol catalyst that is copper-based results in an augmentation of the production of higher alcohols. A high concentration of alkali (3 wt.%.) can lead to the production of approximately 30% more alcohols. The concentration of alkali has a proportional effect on the activity of the catalyst.

The addition of alkali to the Co (Fe) catalyst has the potential to alter the selectivity of the Fischer-Tropsch process. Consequently, the augmentation of the olefins and alcohols of the product may occur at the cost of the aliphatics. The activity of the Fischer-Tropsch catalyst exhibits a direct correlation with the concentration of alkali, and attains its maximum value within the weight ratio range of potassium to iron spanning from 0.5:100 to 1:100 [38].

There exist various factors that may lead to the deactivation of a catalyst [40]. These factors include but are not limited to coking, poisoning, phase transitions, sintering of the active components, volatility of the active components, and surface rearrangement. The utilization of alkali doping has the potential to extend the deactivation period of a catalyst in specific scenarios. It is noteworthy that an overabundance of alkali may have adverse consequences and impede the advantageous outcome. The addition of small amounts of alkali has the potential to extend the operational lifespan of a nickel-aluminum oxide catalyst utilized in the process of CO methanization with H_2. The alkali in this instance serves as a preventative measure against the deposition of "kinetic" coke on the catalyst, as noted in reference [38]. Elevated concentrations of alkali, conversely, promote the crystallization of the Al_2O_3 substrate and, due to the concomitant decrease in active surface area, diminish the catalyst's operational lifetime.

In general, the impact of alkali doping on a catalyst arises from the process of neutralizing acidic sites. The alkali metal in the ethylene oxide catalyst functions to neutralize acidic sites that would otherwise facilitate the isomerization of ethylene oxide to acetaldehyde. Acetaldehyde typically reacts with oxygen to produce water and carbon monoxide in standard circumstances. At a temperature of 300 ºC, when ethylene oxide and air are introduced to the support utilized in the formation of the ethylene oxide catalyst, a portion of the ethylene oxide undergoes isomerization or combustion. In the event that the support is subjected to treatment with alkali metal hydroxide, it is possible to entirely avert the degradation of ethylene oxide. The efficacy of diverse alkali metal hydroxides exhibits similarity in this regard. The utilization of alkali doping has been suggested as a potential method to hinder the formation of coke on nickel catalysts utilized in steam reforming. It has been hypothesized that this outcome is primarily attributed to the neutralization of acid centers [41].

The electronic component is connected to alkali's action on semiconductor and metallic catalysts, which boosts their activity. Adsorption of alkali metal ions onto the metal surface enables for electron-donor activity by neighboring metal atoms. CO chemisorption increases the need for electrons from the 3d ion band, which strengthens

the Fe-C bond while weakening the C-O bond. When hydrogen is chemisorbed, it gives electrons to the iron, weakening the Fe-H bond. Alkali doping may increase the heat of chemisorption of CO by up to 100%. However, the heat of H chemisorption only slightly lowers. As a result, the rate of formation of the primary complex in the Fischer-Tropsch synthesis, as well as the rates of all CO-using processes, is increased. As a consequence, chain building speeds up, and the product spectrum swings toward molecules with more carbon atoms. The reduction in hydrogen adsorption rate hinders hydrogenation activities. As a result, doping with alkali reduces methane synthesis, increases olefin content, and stimulates the formation of oxygenated products.

Unmodified MoS_2 catalysts outperform (K)(Co, Ni, Fe)MoS_2 catalysts in the conversion of syngas to hydrocarbons. The main consequence of alkali metal alteration is alcohol [42][43]. The roles of alkali metals consist of inhibiting hydrogenation activity and promoting the formation of alcohol-producing active sites. K is consideration to poison the hydrogenation activity of MoS_2 toward hydrocarbons. Quantum chemical simulations of CO [44] and methanol [45] hydrogenation pathways on the unpromoted molybdenum disulfide surface suggest that a C-O bond cleavage followed by the synthesis of methane and water is thermodynamically preferable to carbon chain growth. It is considered that modifying the active site with potassium reduces the energy barrier for alcohol synthesis. K ions may serve as CO coordination sites and facilitate the formation of an acyl intermediate on the surface. An alkali metal has been seen to impact the dispersity of the active phase, resulting in a structure-forming property.

The impact of alkali metals such as potassium (K), sodium (Na), and cesium (Cs) on the efficacy of MoS_2 catalysts has been the subject of extensive research over the past few decades, as evidenced by sources [46][47]. As per the findings of Youchang et al. [48], the performance of the catalyst modified with Na is comparatively inferior to that of catalysts modified with other alkali metals. Lithium-based intercalants have been observed to be utilized in batteries [49], however, they are not employed as active phase constituents in MoS_2 catalysts for syngas conversion [[50]. A comparative analysis was conducted to investigate the impact of K and Cs additions on the morphology of CoMoS

catalysts that had been modified. The analysis was carried out through the utilization of scanning electron microscopy and X-ray photoelectron analysis, as documented in [51][52]. Furthermore, an analysis was conducted to evaluate the impact of these supplementary components on the catalytic efficacy. During the process of alcohol production, there is a shift in the distribution of potassium. Iranmah-boob et al., [51] demonstrated that the distribution of potassium, which was previously non-uniform, became uniform following the reaction. The non-homogeneous distribution of Cs remains unchanged throughout the reaction because of cluster formation. Potassium is considered to be an exceptional modulator. An induction period was observed during the process of alcohol synthesis, as reported in [53][54]. The phenomenon can be elucidated by the duration required for the diffusion of potassium across and beneath the layer of MoS_2.

1.4 Effect of Noble and Nonnoble Promoter Atoms

The utilization of DFT calculations was employed to expand the approach to the location of CoMoS nanoparticles [55]. Co-promotion decreases the edge contact between the TiO_2 and Al_2O_3 support. The adhesion energy of the edge-anchored CoMoS cluster through the M-edge, is lower than for the non-promoted system due to the presence of Co at the interface. On Al_2O_3, the promoter's ligand effect (decoration of the MoS_2 particles by the promoter) is likewise prominent, and when Co is present at the interface with the surface of the support, it also decreases the adhesion energy. As a result, the promoter effect, which decreases the Mo- and S-edge energies, explains the reduced particle sizes on alumina. The presence of free edge sites on anatase and alumina in the non-promoted active phase shows that dispersion effects alone cannot account for the diverse promotion effects on HDS activities. On the other hand, the different HDS catalytic activities for the promoted systems on the two supports are undoubtedly due to the different interaction energies inducing a significantly higher S-edge/Mo-edge ratio on alumina, which is favourable for optimal promoter decoration, whereas on anatase, the stronger support interaction with the Mo-edge is detrimental to the promotion effect.

The transition metals Co and Ni are the primary promoters for sulfide catalysts utilized in both HDS and alcohol synthesis [56][57][27][58]. The addition of Ni or Co to the active phase of a K-modified MoS_2 catalyst increases CO conversion and carbon chain growth [59]. The addition of Co to the catalyst alters hydrogenation activity and enhances the yield ratio of alcohol to hydrocarbons. Ni addition mostly enhances the hydrocarbon formation's selectivity [60]. Studies of Co and Ni content effect on K-Co(Ni)MoS catalyst activity in alcohol synthesis reveal that the optimal C_{2+}-alcohol yield is at Co(Ni)/Mo = 0.5 [61][62][63]. The Mo:Co ratio of 1:2 was found to be optimal for both alcohol synthesis and hydro-desulfurization [64]. this shows that the promoter plays comparable functions in both processes. Co(Ni)/Mo 1/3, promoter atoms added into the molybdenum disulphide active phase boost its dispersity. With a rise in promoter concentration, vacancies on the MoS_2 crystallite edges become saturated and distinct Co_9S_8 and NiS_x phases are formed [59][64].

According to Maximov et al.,[43] when MoS_2/Al_2O_3 is promoted with d-metals (Fe, Co, Ni, and related metals), a mixed $MeMoS_2$ phase (Me = Co, Ni, Fe) is established. The author also observed that the presence of Co and Ni contributes to the enhancement of selectivity towards C_{2+} alcohols. The $K\text{-}NiMoS_2/Al_2O_3$ catalyst has the greatest selectivity for ethanol and propanol-1. Changes in catalytic properties were attributed to the promoter's influence on the formation of double sulfide vacancies on the M-edge of (Me)MoS (where Me = Fe, Co, Ni) and K-(Me)MoS (Me = Co, Ni) sites, which may participate in syngas conversion. Similar promoter effects on Mo_2C catalyst activity have been discovered, and according to these studies [65][66], Fischer-Tropsch elements (Ni, Fe, Co) may alter the ASF distribution of alcohols by promoting carbon chain growth.

The effect of nonnoble promoter atoms have been tested on ethanol dehydrogenation. Nonnoble metals have also been studied for ethanol steam reforming, with the majority of research focusing on Ni- and Co-based catalysts for their C-C cleavage capability. Despite their greater potential for coke production, Co and Ni are far less expensive than these noble metals, making research on these two metals considerably more cost-effective.

In relation to dehydrogenation promoted catalysts, ethanol dehydrogenation is primarily carried out over Cu-based catalysts because of their high selectivity for the dehydrogenation products[16][67][68]. In comparison to other catalysts employed for this dehydrogenation process, they indicated that ethanol dehydrogenation occurs under comparatively moderate conditions [69]. Nevertheless, the use of Cu-catalysts is often limited by their quick deactivation, which is mostly caused by sintering owing to the comparatively low melting point of Cu metal. According to Franckaerts and co-workers [70], Cu-based catalysts are the most active to synthesize ethyl acetate, and the promoters and supports type play a vital role in avoiding metal sintering and improving product yield/selectivity. Additionally, promoters are utilized to improve the textural properties of catalysts, which helps avoid or delay sintering of the active phase [71]. Frequently reported catalysts for ethanol dehydrogenation for oxygenated hydrocarbons are metals (Ni, Pd, Au, Ag and Ru) supported on alumina [72]. However, the greater cost of noble metals relative to their non-noble counterparts has facilitated the development of alternate catalytic systems.

Sushkevich et al. [73] investigated MgO, ZrO_2, Nb_2O_5, TiO_2, and Al_2O_3, all supported on silica and promoted with many metals, including Ag, Cu, and Ni. The ethanol conversion over various catalysts varied from 2% to 90%, and the greatest performance was observed with $Ag/ZrO_2/SiO_2$ catalysts with butadiene selectivity greater than 74%. In relation to the absence of coke production in the presence of Ni, metallic Ni exhibited the greatest stability among the examined metal promoters. Riittonen et al. [72] have investigated a variety of metals supported on alumina (such as Ni, Pd, Au, Rh, Ru, and Ag) for the direct conversion of ethanol to butanol at 250^{o}C. More than 80 percent selectivity to butanol at 25% ethanol conversion was recorded for Ni metal supported on alumina in this study, outperforming all other metals with regard to selectivity. Dowson et al. [74] reported a collection of ruthenium-based catalysts, the best of which achieved 94% selectivity to butanol at ethanol conversions greater than 20%. These catalysts stand out due to their superior selectivity in comparison to other systems. These authors also imply that the base-catalyzed aldol condensation of acetaldehyde is most important for

obtaining high selectivity, since increasing the rate of aldol condensation resulted in an increase in butanol selectivity.

Ioan-Cezar's group [75] reported the conversion of ethanol to butanol over Me-Mg-Al, where Me = Pd, Ag, Mn, Fe, Cu, Sm, and Yb. They examined the performance of the catalyst with these metals and (Me)MgAl with Me = Pd, Ag, Mn, Fe, Cu, and Yb. The impact of each metal on the distribution of acidic and basic sites was investigated. All of the catalysts were selective for butanol, while the Cu and Pd catalysts were the most active. Chemical promoters are substances that either generate new active sites or boost existing chemical qualities, such as basicity or redox property, in order to stop the production of carbon [71].

1.5 Effect of Supports

In addition to the active metal and promoters, the selection of the support material exerts a notable influence on the catalysts' efficiency. The optimization of a support for catalytic applications necessitates careful consideration of its surface area, as it is a crucial characteristic. The likelihood of depositing a significant quantity of well-dispersed active phase particles (in this case, transition metal sulphide) is directly proportional to the surface area of the support. These particles are characterized by their optimal spacing, which prevents sintering phenomena and maintains high catalytic activity. In addition, the robust bond between the metal and support (as depicted in **Figure 1.6**) prevents the occurrence of sintering and coking, thereby contributing to the exceptional durability of the metal particles throughout the procedure. Additional support parameters, such as the fundamental acid-base characteristics and the capacity for oxygen storage, are essential factors that contribute to the overall efficacy of the catalysts.

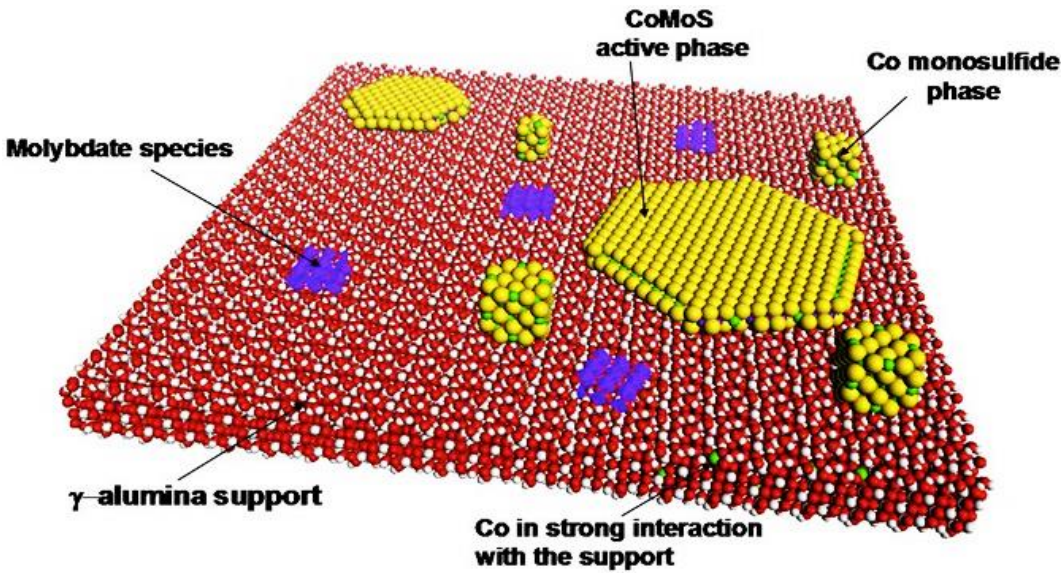

Figure 1.6. Schematic view of the γ-alumina-supported CoMoS catalyst. Color code: Al = red balls, O = red balls, H = white balls, S = yellow balls, Mo = purple balls or octahedra, Co = green balls. Reproduced from Ref. [35].

γ-Al_2O_3 is frequently employed as the support of choice for HDS and HDN, as well as, in combination with silica, for hydrocracking processes owing to its thermal characteristics, stability, and lower cost. γ-Al_2O_3-supported catalysts based on Mo or W and promoted by Co or Ni are among the most active and stable catalysts for the conversion of sulfur compounds. The effects of promotion may be tenfold greater than identical unpromoted catalysts on the same support. In the preparation of oxide precursors, it is difficult to prevent the formation of undesired species such as Co(Ni)MoO_4 or Co(Ni)Al_2O_4 on alumina. These species may result in isolated sulfides of the Co_9S_8 or Ni_2S_3 type, which are very inactive in hydrotreatment, or weakly sulfided species of the Mo oxysulphide type, or even species that cannot be sulfided [76].

Numerous researches have examined the support effect in hydrotreatment, but the findings are sometimes controversial because the observed effect cannot be fully separated from the dispersion state, the Mo (W) surface density, or the preparation or activation process. In addition, the concept of the quality of active sites is relatively recent, with the development of two distinct categories of active sites in particular. Depending on the sulfiding temperature, several authors have found two forms of CoMoS phase that may exist on alumina [77]. The so-called type I form is incompletely sulfided at low

sulfiding temperatures (673 K) and interacts significantly with the support. Type II, on the other hand, is completely sulfided in the CoMoS form at temperatures 873 K and is thought to be much more active than Type I due to a weaker interaction between the active phase and the support. The addition of a chelating agent (NTA, EDTA, citric acid, etc.) with the injection of the promoter promotes the production of Type II [76]. However, the concept of Type II has been revised or improved several times, particularly in relation to the stacking of the slabs, the preparation procedure, and the surface metal content [78].

Attributing this to other supports, silica or carbon supports would be suitable candidates for the formation of Type II phases due to their limited interaction with the active phase. Nevertheless, this does not imply that these two supports are best for the ultimate HDS activity, since they are also the sites of sintering, which is harmful to active phase dispersion. Consequently, the Type I/II idea may be overly restrictive: not only must a weakly interacting support be sought, but a reasonable balance for the active phase – support interaction must also be identified. It may affect several parameters: condition of sulphidation, rate of oxidation, morphology, dispersion, and electronic effects.

Carbon-type supports may have extremely large specific surface areas and well-controlled porosity; if their mechanical qualities were sufficient, however, these supports would be perfect. In addition, sintering of the active phase under hydrotreatment conditions and the restricted ability of these supports to be regenerated after deactivation severely limit the applications that may be used. However, carbon's properties make it a "inert" and dispersive support, which has been utilized in numerous fundamental research seeking to understand the influence of interactions between the support and the active phase by comparing the catalytic activity of carbon-supported sulphide catalysts to those supported on alumina and silica [79][80].

1.6 Ethanol as an indirect intermediate, co-fed with synthesis gas over MoS_2-based catalysts

Several investigations have been performed on the co-feeding of alcohols and syngas over MoS_2 assisted catalysts. Experiments with methanol and ethanol co-fed with

syngas have shown that these alcohols can be readsorbed and converted into higher species through a catalyst [81]. Christensen et al. [82] reported that co-feeding ethanol and syngas promoted the synthesis of higher hydrocarbons as well as higher alcohols. They discovered that increasing the ethanol co-feed over a carbon supported K/Co-MoS_2 catalyst significantly increased the formation of 1-butanol rather than 1-propanol, showing that self-coupling of ethanol or ethanol-derived species leads to 1-butanol.

Synchronous conversion of synthesis gas and ethanol altered the reaction rate and product composition significantly [83]. This was due to ethanol adsorption on the AS catalyst and CO participation in the catalytic cycle. The addition of ethanol to the syngas supplied into the reactor boosted the production of 1-butanol in particular. It is probable that the coupling reaction mechanism over K-promoted Co–MoS_2 supported catalysts resembled a standard aldol condensation [82][83]. This is further corroborated by the improvement of 1-butanol synthesis with acetaldehyde co-feed over a K-Co-MoS_2 catalyst [84].

According to reports [85][86][87], ethanol is one of the primary products of syngas conversion. Ethanol is presumed to be produced as a final product and alternatively as an intermediate for other higher long-chain compounds through CO insertion. Ethanol has the ability to generate additional intermediate species, which promotes the insertion of CO and increases the output of higher alcohols [88]. Nonetheless, the route of ethanol over MoS_2-based catalysts is far from certain.

Overall, structure-reactivity relationships and the location of active sites in MoS_2 catalysts for the synthesis of various oxygenated compounds from ethanol over a MoS_2-based catalyst are unknown and could be investigated to address fundamental knowledge gaps necessary for the rational development of MoS_2-based catalysts on ethanol conversion as a homogeneous process during syngas conversion.

1.7 MoS_2 and Substrates Interaction

The development of MoS_2 catalysts for H_2 production through the hydrogen evolution process has lately received a lot of interest [89][90]. Dehydrogenation reactions

on MoS_2 are significant because they demonstrate that MoS_2 can produce H_2 as well as activate and dissociate it. In this process, amorphous MoS_2 films, crystalline MoS_2 crystals, and microscopic Mo-S clusters all act as catalysts. Some aspects of an effective HER catalyst, such as consideration of electron hole mobility, do not apply to hydrotreating and syngas conversion [91]. Numerous innovative syntheses have been described with the purpose of increasing the surface area of the MoS_2 platelet with the goal of improving HER activity, and odd shapes such as wires, flowers, or geometric patterns have been created in the process. MoS_2 active site cluster models have also advanced [92].

Synthesis gas (syngas) is a mixture of hydrogen and carbon monoxide (sometimes with carbon dioxide) that was initially produced by coal gasification. In the 1930s, Germany and the United States employed MoS_2 catalysts rather than MoS_2-based catalysts for syngas methanation and Fischer-Tropch synthesis [93][94]. The oil crisis of the 1970s reignited interest in developing catalysts for syngas use, owing to the increased need for synthetic fuel blends. Initially, alcohols were recognized as undesired byproducts of Fischer-Tropsch processes [95], until Dow and Union Carbide patented the use of syngas and MoS_2-based catalysts for increased alcohol synthesis [96]. Methanation and Fischer-Tropsch synthesis are catalyzed by bare MoS_2. MoS_2 that has been activated catalyzes the formation of methanol and higher alcohols. Side reactions include the Boudouard reaction (carbon production) and water gas shift (WGS), which is advantageous when the H/CO ratio in a syngas source is less than optimum [96].

The selectivity to higher alcohols on promoted MoS_2 catalysts could be attributed to two separate promotion effects: The addition of alkali metals on the surface increases the availability of CO binding sites while decreasing the availability of hydrogen atoms formed by dissociative adsorption on MoS_2 [33]. The rise in the ratio of carbon monoxide to hydrogen atoms on the surface promotes the insertion of additional carbon monoxide rather than the hydrogenation of intermediates. It has also been discovered that the strongly reducing conditions utilized during the reactions that yield higher alcohols result in a loss of sulfur [81][97] on the surface of MoS_2 based catalysts. The addition of H_2S to

the reactant feed results in the return of sulfur to the surface of MoS_2 and an increase in selectivity for C_{2+} alcohols. The mechanism of higher alcohol synthesis in general, and especially over MoS_2-based materials, is unknown, and synthesis-structure-function links have yet to be achieved for this class of operations [98].

DFT analysis [99][100] of the sources of this novel reactivity suggests that MoS_2-based materials, in particular, disrupt scaling relationships by providing two distinct binding sites. This was discovered as a consequence of the investigation into the sources of this novel reaction. CO* can only be supported on metallic sites at the edge, in this case Co and Ni sites, while CHO* and COOH* can be stabilized by sulfur atoms at the edge, especially sulfur atoms at the bridging position. Although this study was limited to the interaction of a cobalt or nickel promoted MoS_2's S edge with C1 species, the results shed insight on the interaction of both CUS Mo and S sites of non-promoted MoS_2 with CO, CO_2, aldehyde, and carboxylic acid surface species.

1.8 Knowledge gap

The literature identifies the following knowledge gaps in the synthesis of various oxygenates from ethanol:

Ethanol dehydrogenation is carried out predominantly over copper-based catalysts due to the great selectivity that these catalysts exhibit for the dehydrogenation products [67][68]. On the other hand, the convectional catalysts are subject to sulfur poising. The circumstances under which ethanol dehydrogenation takes place are quite insignificant when compared to those required for the use of other catalysts in this dehydrogenation process. In spite of this, the use of copper catalysts is often constrained by their rapid deactivation, which is most frequently brought on by sintering as a result of the relatively low melting point of copper metal [71]. Additionally, promoters are used to increase the textural qualities of catalysts, which helps minimize or delay the sintering of the active phase. This is accomplished by improving the catalysts' surface area. Studies [72] have shown that metals (Ni, Pd, Au, Ag, and Ru) supported on alumina are the most effective catalysts for ethanol dehydrogenation for oxygenated hydrocarbons. However, in

comparison to the cost of non-noble metals, the cost of noble metals is much higher, which has led to the development of alternative catalytic systems. On the other hand, oxide-catalyst systems like ZnO/Cr_2O_3 and Cu/ZnO have become less appealing for the conversion of syngas. Zn, Cr, and Cu oxides or reduced Co have a considerable decrease of activity in the presence of syngas carrying a concentration of less than 100ppm H_2S. The process becomes more complex and more expensive because of the additional purification required to lower the sulfur content to less than a few ppb.

There is no open research on sulfur resistance K-doped Co(Ni, Fe)-promoted MoS_2-based catalysts supported on different novel commercial activated carbons for the ethanol conversion. Several isolated investigations [101][102] suggest that MoS_2 is capable of dehydrogenation, but more research on bulk MoS_2 for these reactions is required before MoS_2 may be commercialized for dehydrogenations. MoS_2 is abundant on earth, durable, and affordable, making it an excellent catalyst for a renewable feedstock-based economy. Although there are few reports of MoS_2 materials for dehydrogenation catalysis, MoS_2 has been widely used for a series of reverse processes known as hydrotreating. In hydrotreating catalysis, hydrogenation and hydrogenolysis processes are used to enhance the cetane number of fuels and eliminate sulfur and nitrogen-containing impurities from petroleum. Hydrotreating catalysis is also known as hydroprocessing. Because of tighter regulations on pollution controls and a general reduction in the quality of petroleum supplies, there has been a rise in the demand for highly efficient hydrotreating catalysts during the 1990s [24]. This demand has been driving up prices. In spite of these demands, research into the mechanisms that underlie reactivity on MoS_2 catalysts is currently ongoing [103]. Recent developments in computational techniques have made it possible to integrate modeling and experimental research, which has resulted to an improvement in our basic understanding of the structures on the MoS_2 surface [83][104]. As a result of the complex structure of the MoS_2 active site, there is also the potential to research the interaction of the MoS_2 surface with intermediates in a new range of reactions. This contributes to the expansion of fundamental knowledge about the origins of MoS_2 reactivity.

CHAPTER 2: Methods and Materials

2.1 Catalyst Supports

The catalysts were synthesized using aluminum oxide (γ-Al_2O_3), carbon-coated aluminum oxide (CCA); commercial granular activated carbons DAS, AG-3, BAW, and YPK-1 (commercial trademark ДАС, АГ-3, БАУ and УПК-1, respectively) and new fibrous activated carbons (commercial trademark AHM and TCA) as support materials.

The γ-Al_2O_3 was purchased from Sigma Chemical Co. (St. Louis, MO, United States), crushed, and sieved to get a particle size distribution of 0.2–0.5 mm. Before preparing the catalyst, it was calcined for six hours at 550°C.

Carbon-covered-alumina (CCA) was prepared by impregnating 4g of Al_2O_3 with about 15mL of a mixture of glycerol and 2-propanol (1:1), followed by pyrolysis under nitrogen (flow rate 1 L/min) at 200°C for 40 minutes and 600°C for 1 hour, with a heating rate of 10°C min^{-1}. The coke concentration was evaluated using thermogravimetric analysis (TGA) using a NETZSCH STA 4449 F3 Jupiter instrument. Thermogravimetric and differential Thermogravimetric curves for the CCA were acquired in flowing air from room temperature to 600°C (10°C/min heating rate). The carbon loading on the CCA support is near to the optimal loading for alcohol generation, which has been found to be 1.7%.

Activated carbon, AG-3 was produced by preparing a dough, granulating, carbonizing, and gas-vapor activating weakly coked coal crude and coal semi-coke with coal tar pitch binder. Activated carbon BAW was produced by activating charcoal grit with gas vapor at 850–900 degrees Celsius. Activated carbon, DAC was derived from anthracite (hard coal) by the processes of dough preparation, granulation, carbonization, and gas-vapor activation. Activated carbon YPK-1 was made using a carbonaceous composition activated by gas-vapor at 850-900 degrees Celsius [105].

Fabric active sorption (TCA) is an elastic sorbent obtained by heat treatment of technical fabric, which previously impregnated with chemical compounds. It was formed as canvases with dimensions: length 20 m, width 0.55 m, thickness 0.6 mm. Non-woven activated material (AHM) was produced by heat treatment of a nonwoven needle-punched

material based on viscose fibers and mtilon fibers. The parameters of the active layer are aerodynamic resistance 10 Pa, surface density 120 $g.m^{-2}$, thickness 1.0-3.5 mm [105].

2.2 Catalyst Preparation, K-(Me)MoS_2 Catalysts, (where Me = Co, Ni, Fe)

A typical Incipient wetness impregnation was used to synthesize the catalysts. Ammonium heptamolybdate tetrahydrate (Alfa Aesar, 99.9% pure; 0.48 g, 5 mmol) was diluted in 1 mL of 20 percent NH_4OH solution and 1.5 mL of distilled water, then combined with 0.40 g (10 mmol) of potassium hydroxide (analytical grade, 98 %). This solution was added to a combination of cobalt acetate (Alfa Aesar, tetrahydrate, 98 percent pure; 2.5 mmol) and citric acid (1.05 g; 5 mmol) in 1 mL of distilled water. The impregnated supports (3 g) were dried in flowing air (1 L/min) for 2 hours at 60 degrees Celsius, followed by 5 hours at 100–110 degrees Celsius. The catalyst precursors were sulfided in an autoclave with crystallized (elemental) sulfur (1:4 catalyst:sulfur) at 360 oC for 1 hour under H_2 pressure of 6.0 MPa.

2.3 Characteristics of Supports and Catalysts

Several characterization techniques were used on the as-synthesized carbon supports and associated K-(Me)Mo-supported catalysts. Relevant methods were chosen to aid in determining the structure, morphology, and textural properties of the materials obtained, as well as to provide insight into their catalytic behaviour.

2.3.1 Thermogravimetric (TGA)

A NETZSCH STA 4449 F3 Jupiter was used to evaluate coke content by thermogravimetric (TGA) measurements. Thermogravimetric and differential thermal gravimetric curves for 0.20 - 0.5 mm of the prepared CCA were recorded in flowing air in the range from room temperature to 600 °C (heating rate 10 °C/min)[106].

2.3.2 Scanning Electron Microscopy (SEM)

To examine the catalyst microstructure, Scanning Electron Microscopy (SEM) was used (SEM – field emission Hitachi SU8000 operated at 1 kV and an 18.4 mm sample

distance and equipped with an Oxford Instruments X-ray microanalysis detector). The samples were mounted in a 25 mm diameter SEM stub with conductive glue and then coated with carbon to prevent charging while under the microscope.

2.3.3 High Resolution Transmission Electron Microscopy (HRTEM)

HRTEM images of the catalysts were obtained on a Tecnai G2 20 electron microscope with 0.14 nm lattice-fringe resolution and an accelerating voltage of 200 kV. The samples used for HRTEM were prepared on a perforated carbon film mounted on a copper grid, and 10 – 15 representative micrographs were obtained for each catalyst in a high–resolution mode. Lengths of at least 500 slabs were measured for each catalyst. To measure the extent of MoS_2 dispersion, an average fraction of Mo atoms on the MoS_2 edge surface was calculated, assuming that the MoS_2 slabs were perfect hexagons[25]. MoS_2 dispersion (D) was statistically evaluated by dividing the total number of Mo atoms on the edge surface (Mo_e), including corner sites (Mo_c), by the total number of Mo atoms (Mo_T) using the slab sizes measured from the TEM micrographs:

$$D = \frac{Mo_e + Mo_c}{Mo_T} = \frac{\sum_{i=1\ldots t} 6n_i - 6}{\sum_{i=1\ldots t} 3{n_i}^2 - 3n_i + 1}, \quad \text{(i)}$$

where n_i is the number of Mo atoms along one side of the MoS_2 slab, as determined by its average slab length $\bar{L}$ (nm), and t is the total number of slabs in the TEM micrographs. The number of slabs per stack was determined to obtain the average stacking number ($\bar{N}$):

$$\bar{N} = \frac{\sum_{i=1\ldots t} n_i N_i}{\sum_{i=1\ldots t} n}, \quad \text{(ii)}$$

where n_i is the number of stacks in N_i layers.

2.3.4 X-ray Photoelectron Spectroscopy (XPS)

The sulfided catalysts were analysed by XPS using a Kratos Axis Ultra DLD spectrometer with a monochromatic AlK_αsource ($h\nu$ = 1486.6 eV, 150 W). Individual

spectral regions were analysed to determine the binding energy (BE) of the peaks, identify the chemical state of the elements and calculate relative ratios of the elements on the catalyst surface. The BE values were referred to the positions of the Au $4f_{7/2}$ peak at 83.96 eV and the Cu $2p_{3/2}$ peak at 932.62 eV. To survey photoelectron spectra, narrow spectral regions (Al $_{2p}$, S 2p, Mo 3d, C 1s, O 1s, Co $_{2p}$) were recorded. The collected spectra were processed by a mixed Gaussian (30 %) – Lorentzian (70 %) method with the use of CasaXPS software. Shirley background subtraction was applied to calculate atomic concentrations. Decomposition of the S2p and Mo3d XPS spectra was performed using appropriate oxide and sulfide references as supported monometallic catalysts.

Atomic concentrations of each element for the sulfided form of the catalyst were determined. Relative concentrations of each species, cobalt oxide Co^{2+}, Co_9S_8, CoMoS, molybdenum oxide Mo^{6+}, MoS_xO_y and MoS_2, for these catalysts were evaluated. For example, a relative amount of Co in the CoMoS phase was determined using the following equation:

$$[CoMoS]\ (\%) = \frac{A_{CoMoS}}{A_{CoMoS} + A_{Co_9S_8} + A_{Co^{2+}}} \times 100\,, \qquad \text{(iii)}$$

where A_X represents the peak area of the species x.

Effective Co content (wt. %) in the CoMoS phase was determined as follows:

$$C_{CoMoS} = [CoMoS] \times C(Co)_T\,, \qquad \text{(iv)}$$

where $C(Co)_T$ represents the effective cobalt concentration on the catalyst surface determined by XPS (at. %).

The promoter ratio in the CoMoS phase slab was calculated using the following relation:

$$\left(\frac{Co}{Mo}\right)_{slab} = \frac{C_{CoMoS}}{C_{MoS_2}}\,, \qquad \text{(v)}$$

where C_{CoMoS} and C_{MoS_2} are absolute Co and Mo concentrations in the CoMoS and MoS_2 species, respectively (at %).

The promoter ratio in the slab edge of the active phase was calculated as follows:

$$\left(\frac{Co}{Mo}\right)_{edge} = \frac{(Co/Mo)_{slab}}{D}, \quad \text{(vi)}$$

where D is the dispersion of the active phase particles obtained using TEM measurements.

The signal at 169.0 eV (characteristic of sulfates) was almost absent, indicating that the sulfided catalysts were not oxidised during the transfer from the sulfiding reactor to the XPS chamber.

2.3.5 N_2 adsorption-desorption Isotherms

To obtain surface analysis data, a Quantachrome Nova 1200e (USA) was used and N_2 adsorption-desorption isotherms at 77 K were recorded. The supports and sulfide catalysts were degassed at 110°C for supports and 250°C for sulfide catalysts for 4 hours each at 10^{-4} Hg. The BET equation was used to calculate SSA. V_{total} was determined at $P/P_o = 0.99$. The Barrett, Joyner, and Halenda technique was used to calculate mesopore size distributions. The mesopore volume was obtained from the desorption branch of Barrett, Joyner, and Halenda (considering the adsorption film thickness on the mesopore surface). Total and mesopore volumes were used to calculate the micropore volume of the samples[107]. For the gas sorption analysis, all sample cells were calibrated before use. Each sample was 0.1 g in weight. The analysis was set to yield at least 25 adsorption curve points (10 for BET and 6 for t-plot/-S) and 45 desorption curve points for the Barrett, Joyner, and Halenda technique.

The turnover frequency (TOF) for ethanol conversion was calculated using a method earlier described in [108]:

$$TOF_{edge} = \frac{F \cdot X_{EtOH} \cdot Ar_{Mo}}{W \cdot C_{MoS_2} \cdot D \cdot 3600}, \quad \text{(vii)}$$

where F is the EtOH molar flow (mol·h^{-1}); X_{EtOH} is conversion of ethanol, %; W is sample mass (g); C_{MoS2} is effective content of Mo in MoS_2 or (Co)MoS_2 crystallites (wt. %) calculated from the XPS spectra; D is dispersity of MoS_2 or (Co)MoS_2 crystallites calculated using HRTEM; Ar_{Mo} – molybdenum atomic mass (95.9 g/mol). TOF_{edge} calculations of the catalysts used in the study are detailed in[41].

2.3.6 UV Spectral Analysis of Pyridine Adsorption

UV spectral spectroscopy of pyridine-adsorption was used to determine the acid-base characteristics of the supported catalysts. UV spectra were used to determine concentrations in solutions using an SF-103 single-beam scanning spectrophotometer. At room temperature for 60 minutes, the adsorption spectra of pyridine in the ultraviolet region of a blank pyridine solution in octane and solutions of adsorption systems with supports and catalyst were recorded. The absorption maxima occur at 253 nm (analytical absorption band) and do not change as the pyridine concentration varies. The concentration of the test catalysts was measured using a calibration curve plotted against the optical density of the solution D and pyridine concentration. **Eq. 8** was used to compute Gibbsian adsorption (G, mol/g):

$$G = \frac{(C_0 - C_t) \times V}{m} = \frac{(D_0 - D_t) \times V}{m \times \varepsilon \times l}, \quad \text{(viii)}$$

where V (solution volume) is 10 ml, m (sample mass) is 0.1 g, D_0 and D_t are equal to the optical density of pyridine at maximum absorption prior and during the adsorption process; L (cuvette length) is 1cm; ε is the molar absorption coefficient (extinction, ε of pyridine = $2 \cdot 10^6$ l/(mol·cm), εBac = $1 \cdot 10^4$ l/(mol·cm)).

2.3.7 Elemental Analysis

The elemental composition of the catalysts was determined using an EDX-7000 X-ray fluorescence (XRF) (Shimadzu, Kyoto, Japan) spectrometer with a Rh tube anode

operated between 8–200 mA and 15–50 kV. All samples were crushed before measurements. The spectra were processed using the method of fundamental parameters.

2.4 Catalytic Activity Studies

The prepared catalysts were tested in fixed-bed reactors in the synthesis of oxygenated hydrocarbons and light hydrocarbons. The influence of hydrogen and helium atmospheres on catalyst performance for ethanol conversion to higher chain alcohols and other oxygenates was assessed using a stainless-steel packed bed reactor. Catalyst loading was 3.0 g, with the particle size ranging from 0.20 to 0.50 mm. In the process described earlier [19,109], the catalyst samples were diluted with quartz grains (size 1-2 mm) to 5 ml before being fed into the reactor. In a typical reaction, it was done at a pressure of 2.5 MPa, temperature of 320ºC, GHSV of 760 $L/h^{-1}\cdot(kg\cdot cat)^{-1}$, and an ethanol space velocity of 0.3 ml/min.

A set of experiments was completed with K-$CoMoS_2$-based catalysts supported on different support materials to examine the EtOH reaction pathways. Rectified ethanol (30 mL) was fed into the reactor, using a high-pressure pump. The catalyst was allowed to circulate with gas for an additional hour, under the same conditions as after the ethanol feeding termination. After 16 hours, liquid products were collected from the reactor.

2.5 Experimental Setup

The catalytic activity of the obtained samples was tested in a unit with a flow-through tubular reactor (10, internal diameter = 15 mm, length = 350 mm) with a fixed layer of catalyst under pressure (**Scheme 2.1**). Ethanol was injected directly into the reactor through line (8) using a high-pressure chromatographic piston pump (7). The reactor was housed in an electric vertical furnace (11) with one heating zone. The temperature was monitored using two thermocouples (9): one directly in the reactor in the catalyst bed and one in the center of the furnace (11). A meter (12) was attached to the thermocouple within the catalyst layer. The setter was the signal from the furnace's thermocouple, and the regulator-meter (13) regulated the electrical signal. The

electromagnetic relay (12) delivered an electric current to the furnace winding (11). Bronkhorst's electronic flowmeter was used to monitor raw material usage (6). The pressure in the reactor was adjusted and maintained by two non-return valves (4 and 19). Manometers were used to monitor pressures in both valves and the reactor (5). Nitrogen from the auxiliary line was used to provide back pressure on both non-return valves, which were supplied by a 40-liter cylinder. The exhaust gases from the reactor (10) reached the high-pressure separator (15), where liquid condensation occurred. Products (17) were examined by gas-liquid chromatography when the experiment was completed.

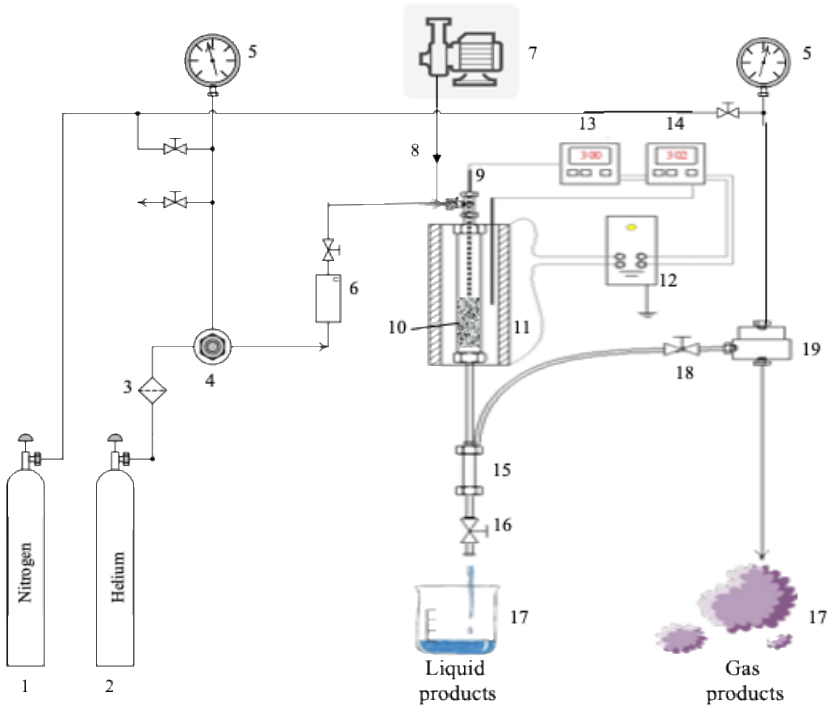

1	Reaction atmosphere
2	Carrier gas
3	Filter
4	Valve (reaction atmospheric gas feed)
5	Pressure gauge
6	Brokhorst flow meter
7	High pressure pump
8	Ethanol feeding
9	Thermocouple
10	Reactor (catalytic bed)
11	Furnace
12	Electromagnetic relay
13	Meter
14	Meter-regulater
15	High pressure separator
16	Valve (liquid product exit)
17	Product collection
18	Valve (gas products exit)
19	Valve

Scheme 2.1: Diagram of a flow-through catalytic unit with a fixed catalyst bed.

2.6 Products Sampling and Composition Analyses

To evaluate the gas products, an LHM-80 (Russia) gas chromatograph (GC) with a TCD detector was used. GC is often used to quantify the composition of gas or liquid mixtures. In order to conduct analysis on liquid samples, they must first be vaporized. When working with a liquid or gaseous sample, an inert gas (mobile phase) is used to move the sample through a heated column (stationary phase), which separates the

components based on their specific chemical characteristics (polarity, chirality, volatility among others). This particular column has been hand-picked for its suitability in the given situation. GC had two packed columns: one with a CaA molecular sieve and the other with a Porapak Q. FID detection was employed for liquid products fitted with a Crystall-2000M GS (Russia) as the probe. A 50 m HP-FFAP capillary column was integrated into the GC.

Conversion of ethanol was calculated as follows:

$$x_{EtOH} = \frac{mole\ EtOH_{reacted}}{mole\ EtOH_{feed}}, \quad \text{(ix)}$$

while selectivity S was determined based on the carbon balance for each component:

$$S = \frac{mole\ products_i\ formed}{n_{EtOH}reacted} \times \frac{nC_i}{nC_{EtOH}} = \frac{AC_i}{Ac_{EtOH}} \times \frac{nC_i}{nC_{EtOH}} \left(\frac{1 - x_{EtOH}}{x_{EtOH}}\right), \quad \text{(x)}$$

where n_{Ci} and nC_{EtOH} represent, respectively, the number of carbon atoms in the component i and in the ethanol-fed, while AC_i and Ac_{EtOH} are normalized chromatographic peaks areas.

CHAPTER 3: Results and Discussion

It is widely established that ethanol undergoes four transformations: dehydrogenation, dehydration, coupling, and the production of aldol condensation products [110]. According to Carrasco-Marin et al. [111], ethanol is first dehydrogenated to produce acetaldehyde, then dehydrated to produce ethene/ether, which are obtained directly from ethanol as primary reaction products through a parallel reaction network, where other products are produced via secondary reactions such as coupling and aldol condensation. The current studies for ethanol conversion over MoS_2-based catalysts demonstrate that this catalytic system could serve as a catalyst for ethanol dehydrogenation. Ethanol is transformed into acetaldehyde (AcH), ethyl acetate (EtAOc), ethyl acetoacetate (EAA), butanol-1 (BuOH-1), propanol-1 (PrOH-1), butyl acetate (BuAOc), CO_2, light hydrocarbons (HC), and traces of CO and diethyl ether (DEE).

3.1 Ethanol Conversion over (K)(Co)MoS_2-Catalysts Supported on Activated Carbon: Effect of Active Phase Composition

It is critical to understand the role of transition metal promoters and alkali metals on investigated MoS_2-based catalysts as one of the aspects to consider when developing an active catalyst for various reaction systems. The primary goal of this section is to examine the influence of K and Co doping on MoS_2 on the synthesis of oxygenated hydrocarbons through ethanol dehydrogenation. The impact of active phase compositions on conversion and product distribution were considered. In addition, the function of acidity of catalyst was examined.

3.1.1 Characterization of the MoS_2-catalysts

The textural features of the investigated materials are summarised in **Table 3.1**: the mesoporous volume (V_{meso}), microporous volume (V_{micro}), total pore volume (V_{total}), and

the BET surface area (S_{BET}), surface area microporous (S_{micro}), and surface area mesoporous (S_{meso}). The K, Co, and Mo loadings on the catalysts were retained at 10, 3.7, and 12 wt%, respectively. The S_{BET} of the granular carbon (C_{AG-3}) support was 854.00 m^2/g, while the pore volume was 0.450 cm^3/g. The S_{BET} of (K)(Co)MoS_2/C_{AG-3} catalysts with various active phase compositions was found to be in the range of 41.10 - 207.00 m_2/g and increased in the order of $CoMoS_2/C_{AG-3}$ < K-$CoMoS_2/C_{AG-3}$ < K-MoS_2/C_{AG-3} < MoS_2/C_{AG-3}. The textural features of the $CoMoS_2/C_{AG-3}$ catalyst were observed to diminish in an unexpectedly sharp manner. The unexpected effects seen may be explained in part by the presence of organic material on the surface/pores throughout the preparation and drying procedures. It is generally established that catalysts with a larger surface area may improve catalytic activity by improving active phase dispersion and, as a result, increasing active site exposure. Adsorption of reactant molecules on metal active phases improves as surface area increases. Carbon support was chosen for its excellent surface area, low acidity, and surface inertness. The use of carbon supports enables more active Type II Co(Ni)Mo(W)S stabilisation [112][113]. Carbon-supported catalysts are more active than metal oxide-supported catalysts [114]. The researchers discovered that high contact in Al_2O_3-supported catalysts is detrimental because it favours the formation of the low-active (Type I) Co-Mo-S structure.

When the textural properties of the support and (K)(Co)MoS_2-supported catalysts were evaluated, the synthesised catalysts had much lower textural properties than the support. The BET surface area and pore volume decreased following impregnation of active metals on the support, indicating that the metals filled the partial pores of the support. When K was added to MoS_2/C_{AG-3} and $CoMoS_2/C_{AG-3}$ catalysts, there was very little difference in V_{meso}. Based on these observations, it is reasonable to believe that a considerable number of K-modifier atoms are deposited inside the pore. Following K, Co, and Mo loading, active phase precursors had no effect on the diameter of the support pore. All catalyst samples showed narrow pore-size distributions of around 3.6 nm, which was the same as the original C_{AG-3}.

The normalised surface area (NSA) was calculated to estimate the possibility for support pore blocking induced by the loading of active metals, as described in [115]:

$$\mathrm{NSA} = \frac{(S_{BET})_{catalyst}}{(1-y)} \times \frac{1}{(S_{BET})_{support}}, \quad \text{(xi)}$$

where NSA denotes the normalized S_{BET} and y denotes the active phase weight fraction. Normalized NSA values are shown in **Table 3.1**. The different NSA values indicate that the metals partially blocked the pores of the support. The blocking extent (BE) of the support pores was calculated using the equation BE = 1 - NSA. BE was found to be higher in the presence of the $CoMoS_2$ catalyst, which suggests that there are a lot of surface pores blocked.

Figure 3.1 depicts (a) the N_2 adsorption-desorption isotherms (b) and the pore-size distribution at 77K of the impregnated C_{AG-3} material with varying active phase compositions. According to the International Union of Pure and Applied Chemistry (IUPAC) classification [116], the adsorption isotherms (**Figure 3.1a**) of MoS_2/C_{AG-3}, $CoMoS_2/C_{AG-3}$, K-MoS_2/C_{AG-3}, and K-$CoMoS_2/C_{AG-3}$ may be classical Type IV, which is characteristic for microporous materials. All of the samples show Type IV isotherms with an H3 hysteresis loop, confirming the catalysts' slit-shaped mesoporous structure. Adsorption at low relative pressure (below 0.20) may be ascribed to micropores, while adsorption at high relative pressure (over 0.40) can be attributed to mesopores.

Table 3.1. Textural and surface acidity support and catalysts

Catalysts	S_{BET} [a] ($m^2 \cdot g^{-1}$)	S_{micro} ($m^2 \cdot g^{-1}$)	S_{meso} [b] ($m^2 \cdot g^{-1}$)	V_{total} ($cm^3 \cdot g^{-1}$)	V_{micro} [c] ($cm^3 \cdot g^{-1}$)	V_{meso} [d] ($cm^3 \cdot g^{-1}$)	NSA [e]	BE [f]	D_p, [g] (nm)
C_{AG-3}	854.00	753.90	100.10	0.450	0.350	0.100	-	-	
MoS_2/C_{AG-3}	207.00	154.50	52.50	0.119	0.072	0.047	0.33	0.67	3.629
$CoMoS_2/C_{AG-3}$	41.10	27.30	16.80	0.042	0.013	0.029	0.064	0.94	3.618
K-MoS_2/C_{AG-3}	196.60	139.40	57.20	0.105	0.064	0.041	0.30	0.70	3.777
K-$CoMoS_2/C_{AG-3}$	164.00	137.00	27.00	0.090	0.060	0.030	0.45	0.55	3.618

[a] BET surface area;

[b] $S_{meso} = S_{BET} - S_{micro}$;

[c] micropore volume calculated by t-plot method;

[d] mesopore volume calculated by BJH method;

[e] NS_{BET} – normalized BET surface area determined by equation (iii);

[f] BE – blocking extent of the pores of the support due to metal loading calculated by $BE = 1 - NS_{BET}$;

[g] mesoporosity was calculated via the ratio of mesopore volume to total pore volume**.**

Figure 3.1b depicts the predicted pore size distribution from nitrogen adsorption. All of the samples show multimodal pore size distributions and similar average pore sizes (3.5-3.8 nm), as well as well-defined pore size distributions. Multimodal pore size distribution improves active phase availability and even metal deposition. Because the pore capacity of the MoS_2/C_{AG-3} catalyst decreased significantly when Co was introduced, it is probable that considerable amounts of cobalt were deposited within the pores

Figure 3.2 depicts the SEM/EDX-EDS study of K-(Co)MoS_2/C_{AG-3} morphology. The SEM clearly showed nanoparticle-encapsulating porous carbon matrices, which may expose more active sites during the catalytic process, allowing the reaction rate to improve [117]. Furthermore, the introduction of active metals alters the porosity properties of the catalyst's surface. The EDX maps reveal that K, Co, Mo, and S form a uniform phase on the surface of the (K)-(Co)MoS_2/C_{AG-3} catalysts based on the element distribution maps. K and Co, on the other hand, may generate phases that are independent of Mo. Mo and S were found to cover almost the whole field in MoS_2/C_{AG-3} (**Figure 3.2a**).

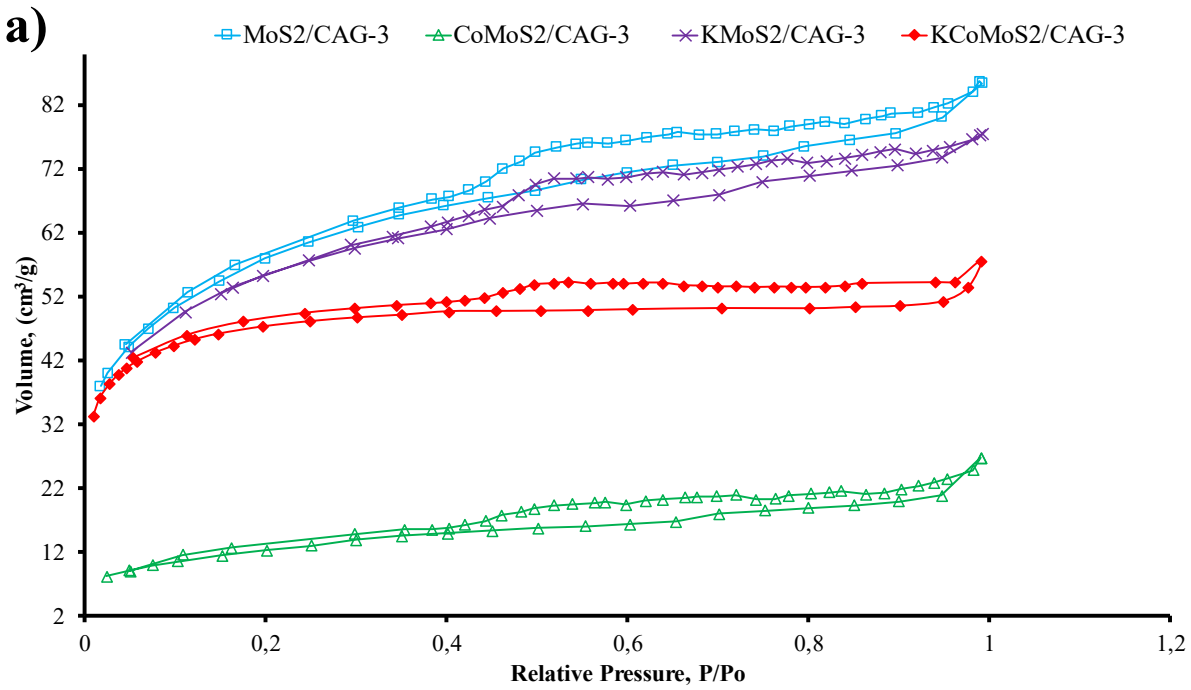

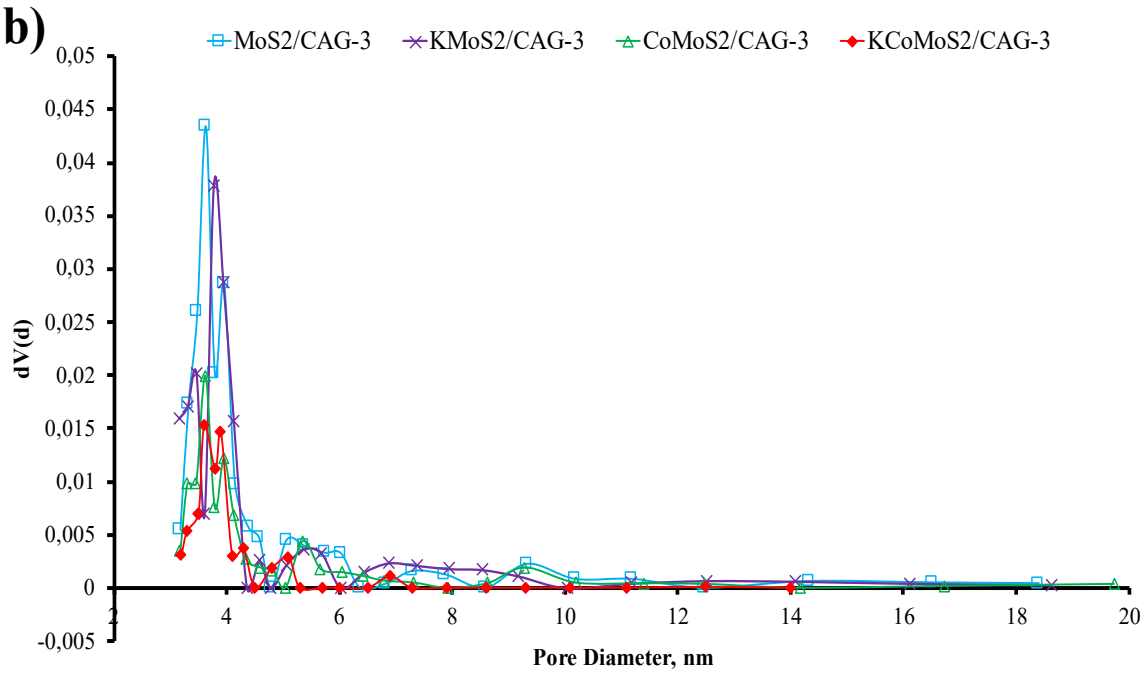

Figure 3.1. N_2 adsorption-desorption (a) and BJH pore-size distribution (b) profile of MoS_2/C_{AG-3} (•); $CoMoS_2/C_{AG-3}$; (Δ); K-MoS_2/C_{AG-3} (×); K-$CoMoS_2/C_{AG-3}$ (♦).

Furthermore, **Figures 3.2b** and d show that, whereas the components in the $CoMoS_2/C_{AG-3}$ and K-$CoMoS_2/C_{AG-3}$ catalysts formed an aligned correlated distribution, Co had a much more equal distribution. This is to be anticipated given that Co accumulates around the margins of MoS_2 crystallites and Co may generate a significant quantity of its own sulphide phases. The exceedingly bright particles of K reveal that, to a certain degree, K may form its own phase non-uniformly with Mo and S in K-incorporated catalysts, notably K-MoS_2/C_{AG-3} (**Figure 3.2c**).

The EDS spectrum shows that the Mo and S elemental distribution has a significant signal at roughly 2.5 keV, which is consistent with the results of the EDX investigation of MoS_2 catalysts [7]. This is proof that the CoMoS phase has developed. Potassium is distributed equally on the CoMoS active phase and on the support material when no active phase is present, suggesting that it interacts with oxygen-containing functional groups on the support surface. This gives indirect evidence of the CoMoS active phase development in MoS_2-based catalysts. It is consistent with the EDX maps.

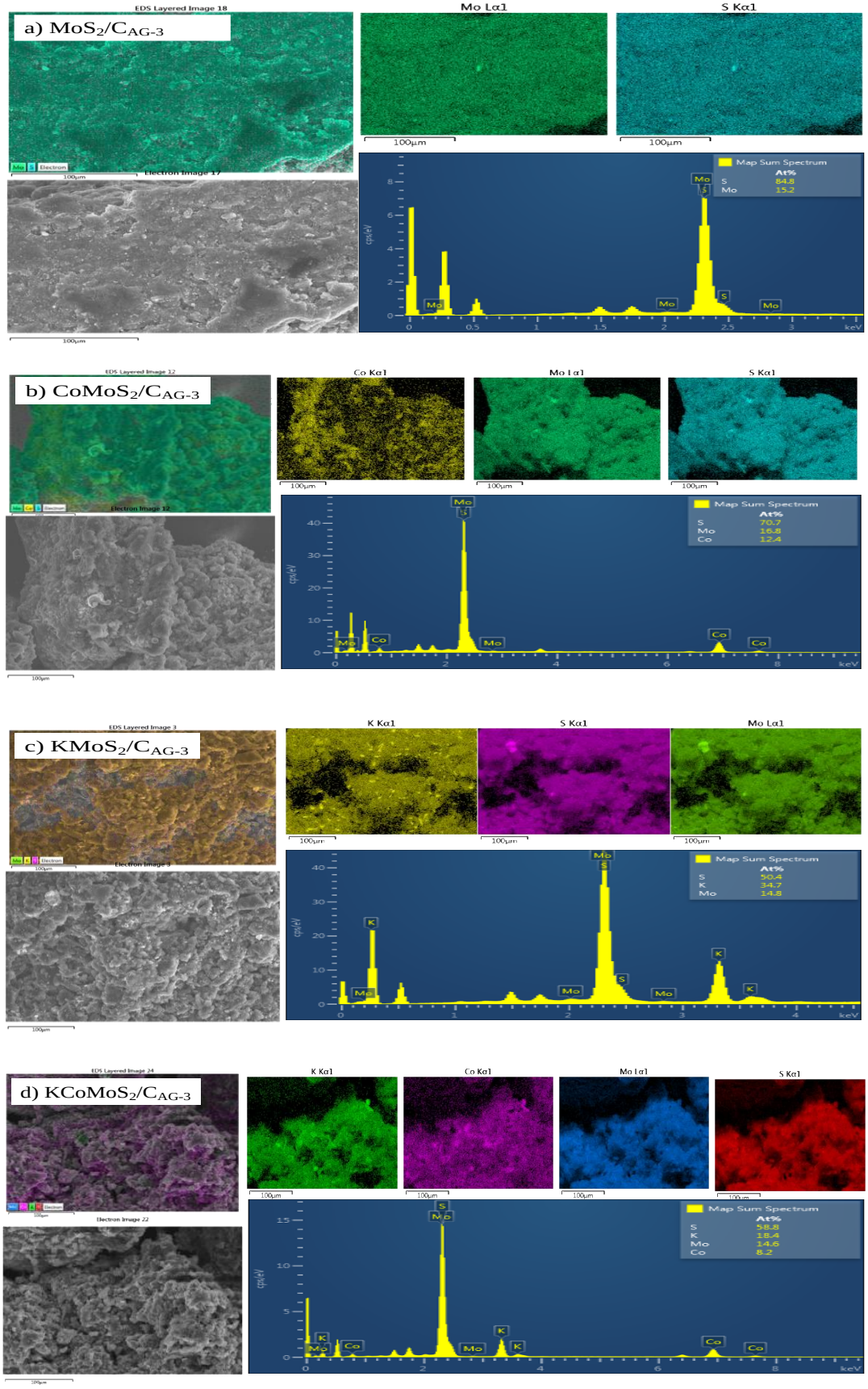

Figure 3.2. SEM/EDX micrographs and EDS spectra of (K)-(Co)MoS_2 catalysts; a) MoS_2/C_{AG-3}; b) $CoMoS_2/C_{AG-3}$; c) K-MoS_2/C_{AG-3}; d) K-$CoMoS_2/C_{AG-3}$, displaying the homogeneous presence of K, Co, Mo, S.

3.1.2 Catalytic Activity Tests

3.1.2.1 Influence of $KCoMoS_2/C_{AG-3}$ Acidity on Conversion

The activity of the catalysts was evaluated in a continuous-flow tubular fixed-bed reactor with a constant temperature of T = 320 ºC and a constant pressure of P = 2.5 MPa. **Table 3.1** displays the total acid sites in the following order, from least to greatest C_{AG-3} (3.62 µmol.g^{-1}) < MoS_2/C_{AG-3} (6.88 µmol.g^{-1}) < K-MoS_2/C_{AG-3} (11.69 µmol.g^{-1}) < $CoMoS_2/C_{AG-3}$ (19.27 µmol.g^{-1}) < K-$CoMoS_2/C_{AG-3}$ (23.12 µmol.g^{-1}). Even while the carbon support material was not acidic, the acidity of the impregnation solution accounts for the rise in sample acidity, with the development of more acid sites on the catalyst surface. The incorporation of transition metal atoms (Lewis acids), as described in [118][119], leads in the development of additional active site. It is worth mentioning that the chelating agent (citric acid) used to create the Co-precursor solution may be responsible for the surprisingly high acidity of Co-promoted catalysts.

The impact of catalyst acidity on conversion is seen in **Figure 3.3**. As can be observed, no apparent relationship exists between total conversion and catalyst acidity.

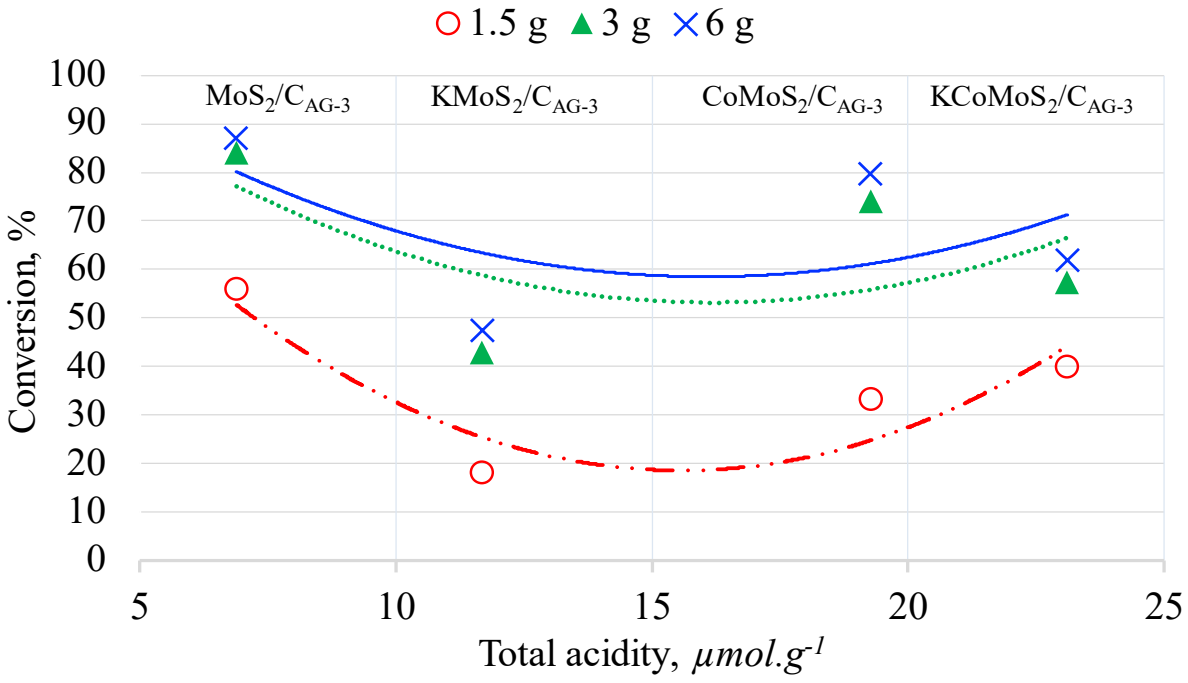

Figure 3.3: Dependence of conversion on catalyst total acidity. Reaction conditions: (GHSV= 760 L·h^{-1}·(kg·cat)$^{-1}$; catalyst loadings = 1.5 g (3 g and 6 g); feed volume = 30 ml ethanol; ethanol flow rate = 0.3 ml/min; T = 320ºC; P = 2.5 MPa).

The conversion rises as follows, regardless of the acidity of the catalyst: K-MoS_2/AG-3 (11.69 μmol.g^{-1}) < K-CoMoS_2/AG-3 (23.12 μmol.g^{-1}) < CoMoS_2/AG-3 (19.27 μmol.g^{-1}) < MoS_2/AG-3 (6.88 μmol.g^{-1}), suggesting that conversion was not acidity dependent. Based on the above findings, it is possible to claim that metal atoms in the active phase's composition had a substantial impact on conversion. Our prior research [43] have corroborated this.

3.1.2.2 Dependence of Conversion on Catalyst Loading

Figure 3.4 demonstrates the effect of catalyst loading as well as the dependency of catalytic activity on active phase composition for ethanol conversion over K-(Co)MoS_2 supported by AC. As previously observed, increasing the catalyst loading enhanced conversion. The conversion rate increases in the following sequence: 1.5 < g 3 g < 6 g. Conversion rose significantly when the weight was raised from 1.5 to 3 g. Nevertheless, increasing the catalyst loading above 3 g does not result in a substantial increase in reaction conversion. Increased catalyst quantity increases the number of available active sites, resulting in a more efficient interaction between the catalyst and the reactants.

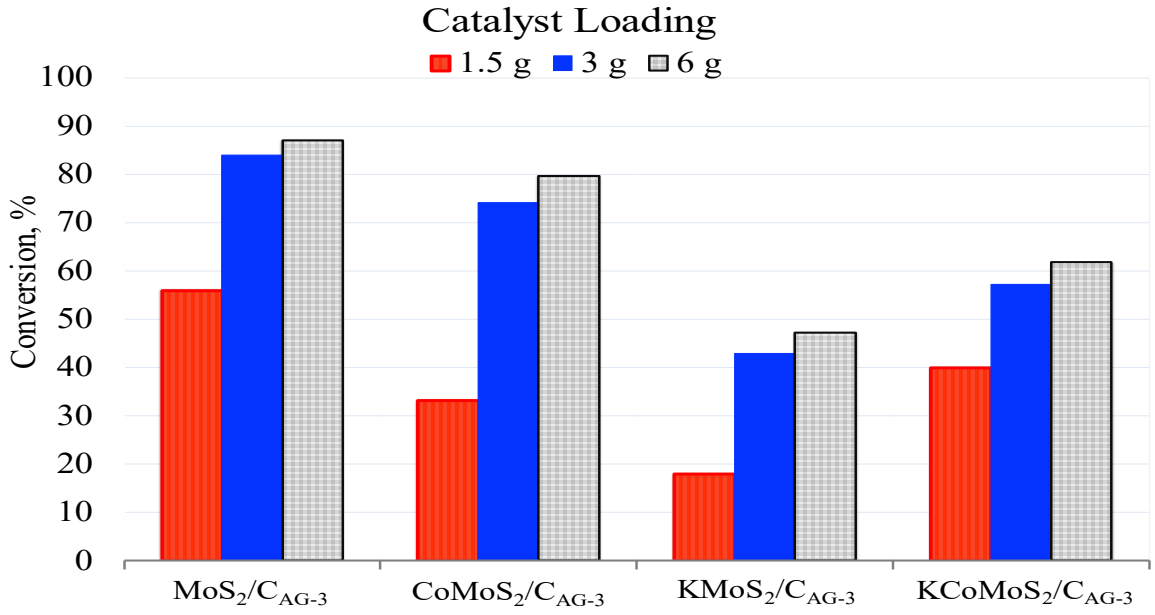

Figure 3.4. Influence of catalyst loading and active phase composition on ethanol conversion. Reaction conditions: (GHSV= 760 $L{\cdot}h^{-1}{\cdot}(kg{\cdot}cat)^{-1}$; catalyst loadings = 1.5 g (3 g and 6 g); feed volume = 30 ml ethanol; ethanol flow rate = 0.3 ml/min; T = 320ºC; P = 2.5 MPa).

The contact time between the catalyst and the reactants increases as the catalyst concentration increases, allowing the reaction to use ethanol as a reactant while also producing it as an intermediate, which is then used to produce the desired products. As the total number of active sites accessible to the reaction increases, so does the rate at which it reaches equilibrium. The difference in conversion between 3 and 6 g indicates the impact, and increasing the amount of catalyst appears to begin opposing mass transfer in heterogeneous catalytic systems. With 3 g of catalyst loading, it seems that equilibrium is reached on the first stage and then rapidly progresses to the second stage. According to [120], increasing the catalyst loading increased the reaction rate while reducing the time required for the reaction to reach equilibrium. Excess catalyst is undesirable for conversion because it obstructs mass transfer in a heterogeneous reaction system, causing the process to approach equilibrium conversion [121].

3.1.2.3 Dependence of Product Distribution on Catalyst Loading

Figure 3.5 shows how catalyst loading (1.5 g, 3 g, and 6 g) affected product yields. The catalyst load had a significant impact on the distribution of product yield. **Figure 3.5a** shows a comparable yield of EtAOc for all catalyst loadings over MoS_2/C_{AG-3}. However, in **Figures 3.5b, c**, and **d**, the EtAOc and EAA yields across $CoMoS_2/C_{AG-3}$, $K\text{-}MoS_2/C_{AG-3}$, and $K\text{-}CoMoS_2/C_{AG-3}$ are somehow at equilibrium at 3 g catalyst loading. Increasing the catalyst loading above 3 g has no discernible effect on EtAOc yields. This may imply that the reaction has achieved equilibrium in respect of synthesis of this product at all loadings. With the exception of **Figure 3.5b**, the amount of EAA rose as catalyst loading increased. However, the increase in the amount of EAA may not only be reliant on the amount of catalyst supplied, but also on the amount of EtAOc, since EtAOc is an intermediary in the Claisen condensation process that creates EAA. EtAOc is formed as a consequence of two sequential reactions, one of which yields AcH as an intermediary step. The production of an acetyl species arises from the dehydrogenation of the adsorbed ethoxy species. Following that, the ethoxy and acetyl species react to produce adsorbed ethyl acetate, which desorbs after [122].

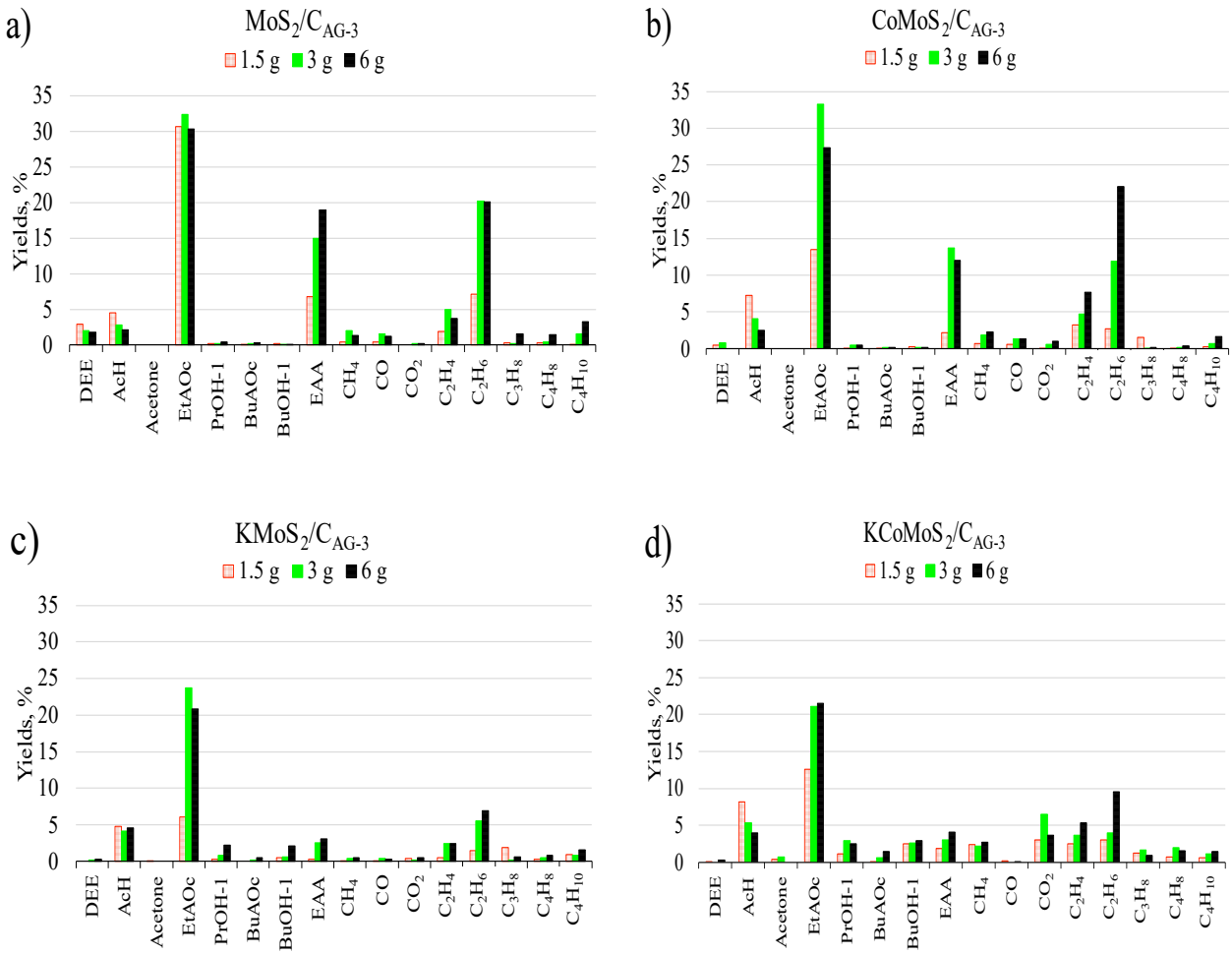

Figure 3.5. Dependence of product yields on catalyst loading over: a) MoS_2/C_{AG-3}; b) $CoMoS_2/C_{AG-3}$; c) K-MoS_2/C_{AG-3}; d) K-$CoMoS_2/C_{AG-3}$

The amount of AcH produced decreased as catalyst loading increased, and this quantity coincided with an increase in EtAOc production. It is probable that increasing the catalyst loading lengthens the residence time of the AcH intermediate on the catalyst, resulting in a higher yield of EtAOc during the reaction with more ethanol/ethoxy species. As illustrated in **Figure 3.5**, all MoS_2 based catalysts seem to follow a quantitatively similar pattern: the initial intermediate AcH is generated, followed by EtAOc and dehydration to C_2H_6. However, the hydrogenation process consumes some of the H_2 produced during the ethanol-to-AcH transition. Increasing the quantity of catalyst in the solution allows the second reaction step to occur, resulting in more EtAOc.

The quantity of HC increases as catalyst loading increases, notably the amount of C_2H_6 and C_2H_4 as seen in **Figure 3.6**. According to Ketabchi et al. [123], increasing the

quantity of catalyst from 0.2 to 0.35 g resulted in a slight increase in the yield of shorter chain hydrocarbons. They attributed this to the development of the reaction network and the increase in the number of active sites due to increased catalyst loading. Furthermore, this impact is explained by the fact that when the amount of catalyst loading increases, the number of electrophile sites increases proportionally, resulting in an increase in yield, which is consistent with the findings in [124]. The minor rise in the dehydration product, C_2H_6, was accompanied by a little drop in DEE, which might be attributable to the fact that ether can be an unstable product under the reaction conditions, and that it can decompose into the corresponding alcohol and olefin.

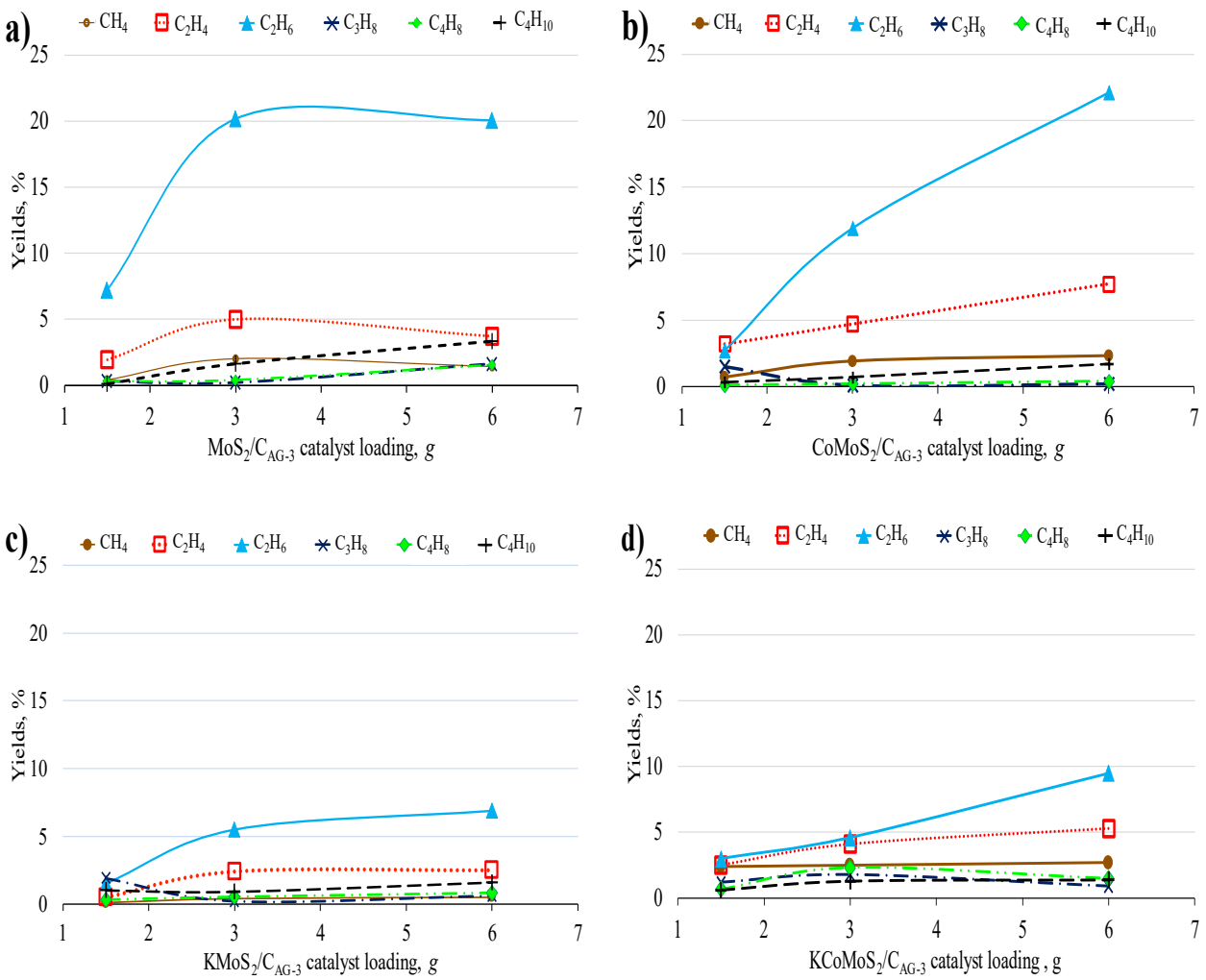

Figure 3.6. Effect of K-addition on hydrocarbons (HC) product distribution; a) MoS_2/C_{AG-3}; b) $CoMoS_2/C_{AG-3}$; c) K-MoS_2/C_{AG-3}, d) K-$CoMoS_2/C_{AG-3}$

3.1.2.4 Dependence of Conversion and Product Distribution on Catalyst Active Phase Composition

The results shown that addition of Co (Ni or Fe)-promoter to MoS_2 catalysts had mior effect on ethanol conversion compared to the non-promoted and unmodified MoS_2 catalyst (shown in **Figure 3.7**), with conversion ranging between 74% and 94%. Conversion decreased in the following order: $FeMoS_2$ > $NiMoS_2$ > MoS_2 > $CoMoS_2$. K-addition into MoS_2 and (Me)MoS_2 catalysts, on the other hand, significantly reduces conversion compared to K-free (Me)MoS_2 catalysts, and conversion decreases in the following sequence: K-$CoMoS_2$ > K-$NiMoS_2$ > K-MoS_2 > K$FeMoS_2$.

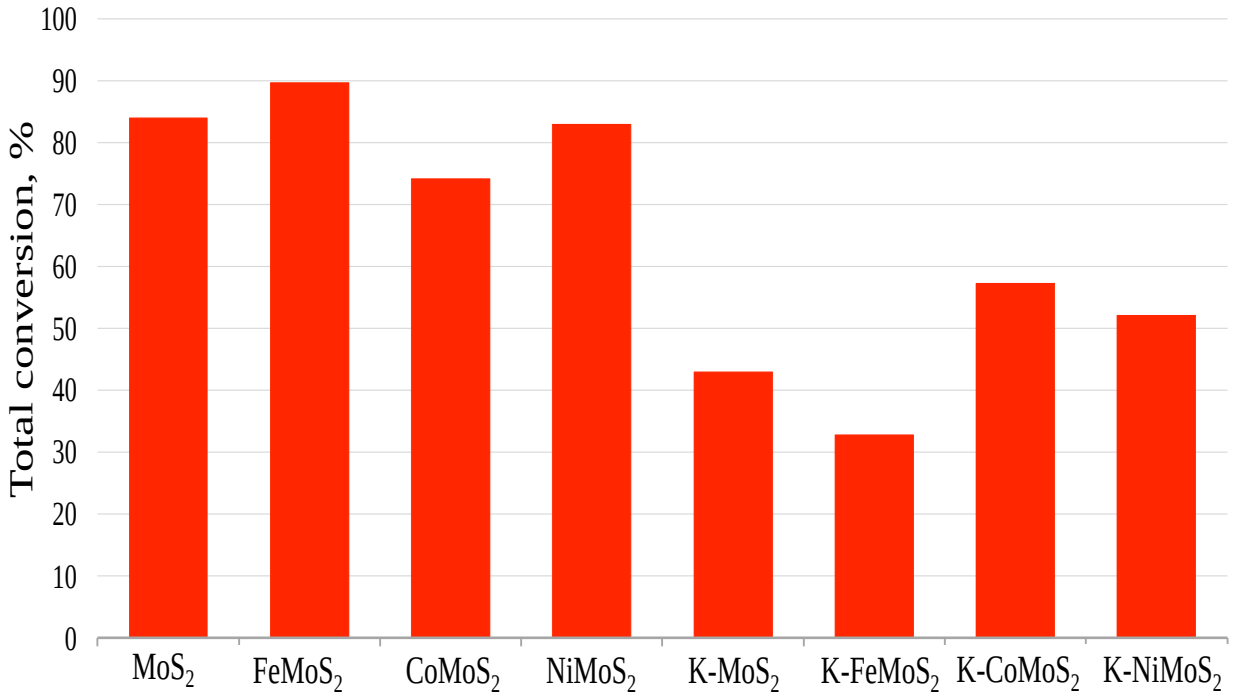

Figure 3.7. Influence of active phase composition on ethanol conversion. Standard reaction conditions: (GHSV= 760 $L.h^{-1}(kg.cat)^{-1}$; catalyst loadings - 3 g, feed volume - 30 mL ethanol; ethanol flow rate - 0.3 mL/min; T = 320 ºC; P = 2.5 MPa)

The activity of MoS_2-based catalysts correlates with the presence of coordinatively unsaturated sites (CUS) on the S- and M-edges. In the thermodynamically stable state, there is a substantial number of vacancies on the S-edge of MoS_2, but these are very few, if any, on the M-edge. In (Me)MoS_2 (Me = (Fe, Co, or Ni) phase, promoter atoms replace some Mo-atoms on the crystallite edges. Single Fe, Co, or Ni atoms promoting the S-edge

create (K)MeMoS sites, which are not capable of activating hydrogen and hence are relatively inactive under reaction conditions. On the other hand, a promoter contributes to the generation of three distinct Fe/Co/Ni sulfide phases responsible for hydrogenation and a mixed "K-CoMoS", "K-NiMoS", or "K-FeMoS" phase that enhances carbon chain growth.

The excess of Co/Ni/Fe causes the formation of a low-active Co_9S_8/NiS_x/FeS phase, which may block (Me)MoS active sites and result in a partial loss of catalytic activity. A considerable decrease in conversion over (Me)MoS_2 was also seen following modification with K. The K incorporation into (Me)MoS_2 systems, reduces the metal atoms [83] of the active sites while increasing the linear diameters and stacking numbers of the layers in MoS_2 crystallites [125][33], and this decreases catalytic activity. Moreover, the addition of K strengthens the Me-S bond and reduces the amount of vacancies formed on the edges. There was a considerable decrease in conversion over K-$FeMoS_2$ catalysts, which might be ascribed to the deactivation of the edge that contributes to catalytic performance. This indicated that Fe is more sensitive to the presence of K, and K acts as a strong poison on the edges, resulting in a loss in catalyst activity. The observed decrease in catalytic activity was ascribed to K-modified active site alteration, crystallite aggregation, and a decrease in the number of accessible sites on the surface.

The promoter atom influences the electron density on the antibonding d-orbital of the Mo in the Me-Mo-S phase [126]. The Mo-S bond weakens as the electron density on the Mo atoms rises. This minimises the amount of energy needed to form active sites, i.e. anionic vacancies. Furthermore, Ishutenko et al. [1] revealed that the addition of K caused partial poisoning of the active sites, resulting in a decrease in catalytic activity when compared to the reference Mo/Al_2O_3 and CoMo/Al_2O_3 samples. Furthermore, the shift in the activity of the catalyst is attributable to the interaction of K with the support and K with Mo [127], as demonstrated by XRD. These interactions have a substantial impact on the composition of the catalyst phase and catalytic performance. However, we should not rule out the possibility of a partial effect of the catalyst's textural features on conversion. Conversion decreases can also be attributed to active phase aggregation with the

following pore obstruction. Probably because of this phenomenon, active species deposition within the pores is reduced.

The yields of the formed products from ethanol over K-(Me)MoS_2 supported on AC are shown in **Table 3.2**. It evidences that product distributions were directly dependent on the active phase composition. The addition of K source to (Me)MoS_2 reduced EtAOc and enhanced AcH synthesis. EtAOc was synthesized at its highest yield and increased as follows: K-(Me)MoS_2/C_{AG-3} < K-MoS_2/C_{AG-3} < (Me)MoS_2/C_{AG-3} < MoS_2/C_{AG-3}. It seems like the increased availability of MoS_2 sites (over K-free catalysts) is likely a source of EtOAc active sites, and the interaction between K and Mo seems to be detrimental to EtOAc formation. It has been shown that catalysts comprising transition metal elements active in ethanol dehydrogenation produce significant amounts of EtAOc [128].

Furthermore, it seems that a reduction in CO formation resulted in an increase in CO_2. The water-gas-shift (WGS) reaction is thought to be responsible for the increased/decreased CO_2/CO production. Assuming that water was produced during the ethanol process, the amount of water formed was sufficient to convert CO/H_2O to CO_2. The WGS reaction is significant because it has the ability to alter CO and CO_2 synthesis. Co-promoted catalysts have been demonstrated to enhance the WGS process. As a result of the observed increase in CO_2 yield after the promotion of MoS_2 and K-MoS_2.

The activity for ethanol dehydration and hydrogenolysis was found to be high in the presence of K-free catalysts and reduced in the presence of K-Mo catalysts. Maximum yields ethene (produced through dehydration reaction) were achieved over K-free and Me-free MoS_2/C_{AG-3} catalysts. Interestingly, ethanol dehydration products were identified at greater yields using the less acidic catalyst (Me)MoS_2/C_{AG-3}, i.e., K-free samples, despite the absence of a clear association between yields and acidity. On the contrary, according to several findings [7,119,129], strong acids are responsible for the dehydration response. Based on these data, it is possible to conclude that when MoS_2 was promoted with K, the alkali metal species interacted with and decreased the majority of the acidic sites involved in the dehydration process.

Table 3.2. Dependence of product yields on catalyst active phase composition, K-(Me)MoS_2/C_{AG-3}, where Me = Co, Ni or Fe

	Yields (%)							
Active Phase	MoS_2	$FeMoS_2$	$CoMoS_2$	$NiMoS_2$	K-MoS_2	K-$FeMoS_2$	K-$CoMoS_2$	K-$NiMoS_2$
Conversion, %	83.8	42.8	93.8	74.2	87.9	34.1	56.5	49.5
Yield, %								
EtAOc	32.3	12.1	33.3	16.0	23.7	12.4	21.1	8.9
EAA	15.0	4.2	13.7	5.4	2.6	2.3	3.0	0.8
AcH	2.8	1.2	4.1	2.2	4.2	2.9	5.3	6.2
BuAOc	0.2	0.0	0.2	0.4	0.2	0.0	0.6	0.7
DEE	2.0	0.0	0.8	0.1	0.2	0.0	0.0	0.0
PrOH-1	0.2	0.0	0.5	0.9	0.8	0.9	2.9	1.7
BuOH-1	0.1	0.0	0.2	0.5	0.6	0.0	2.6	6.2
CH_4	2.0	1.5	1.9	0.1	0.4	0.1	2.2	5.0
CO	1.6	0.9	1.3	9.2	0.4	0.0	0.0	1.7
CO_2	0.2	0.4	0.6	2.0	0.2	1.3	6.5	5.2
C_2H_4	5.0	19.9	4.7	6.7	2.4	3.0	3.6	2.8
C_2H_6	20.2	47.4	11.9	39.3	5.5	8.0	4.0	7.2
C_3H_8	0.2	1.1	0.1	0.9	0.2	1.2	1.6	1.0
C_4H_8	0.4	1.0	0.2	0.6	0.5	0.6	2.0	0.9
C_4H_{10}	1.6	3.9	0.7	3.6	0.9	1.4	1.1	1.2

The effect of K-addition to (Me)MoS_2 on HC yields. Alkali promoters inhibit surface alkyl species' capacity to hydrogenate and produce HC after inclusion [130], notably over K-MoS_2/C_{AG-3} and K-(Me)MoS_2/C_{AG-3}, and shift formation towards the alkoxide. It also reduces C-O bond splitting in adsorbed intermediates on active sites and shifts fragment selectivity from alkyl to alkoxide. There is substantial evidence that the addition of K has a significant impact on catalytic performance with a significant change in product distribution, also demonstrating that the K cation has a significant impact on the character of the pure MoS_2 phase [131] with a notable impact on catalyst performance. Promotor atoms, on the other hand, seem to be decreasing hydrogenation sites in MoS_2, reducing overall HC yields

The reduced rate of hydrocarbon production with the presence of K could be due to a reduction in the availability of hydrogenation active sites. The availability of active hydrogen atoms is more essential in the production of hydrocarbons because the synthesis of hydrocarbons requires stronger hydrogenation centers. As a result, it is not surprising that the yields of hydrocarbons decrease monotonically as K-doping.

The selectivity to alcohols increases while the selectivity to hydrocarbons decreases with the addition of the Group VIII metal, with the highest yield to alcohols and the lowest hydrocarbon yield observed following both promotions with Group VIII metals and modification with K. The promoter metal and modifiers had a profound impact on C_2-hydrocarbon yields, and the yields decreased in the following order: $FeMoS_2$ > $NiMoS_2$ > MoS_2 ≥ $CoMoS_2$ and K-$FeMoS_2$ > K-$NiMoS_2$ > K-MoS_2 > K-$CoMoS_2$. The addition of Ni, Co, or Fe to MoS_2 and K-MoS_2 increased the selectivity to hydrocarbons, notably C_2, especially over Fe-containing catalysts, which may be attributed to Fe-containing catalysts generally accepted greater Lewis acidity compared to their counterparts.

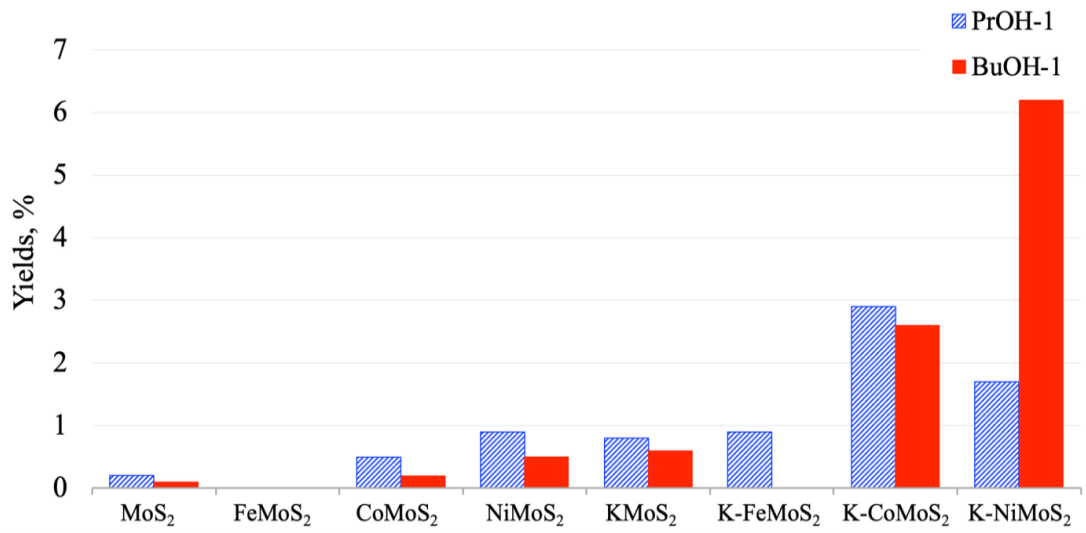

Figure 3.8. Dependence of alcohols yields on catalyst active phase composition

Over K-modified catalysts, the K-Mo interaction enhances MoS_2 aggregation, which reduces the availability of Mo-(CUS) sites and, as a result, inhibits hydrocarbon synthesis while promoting alcohol production. Also, alkali modifiers inhibit deoxygenation. The alcohol yields increased as follows: MoS_2 < (Me)MoS_2 < K-MoS_2 < K-(Me)MoS_2 (**Figure 3.8.**). Furthermore, K species may influence not only the formation of various oxidized precursors but also the microstructure, surface morphology, and electronic properties of active MoS_2 phases. The addition of K not only alters the electronic properties of the catalyst but also stabilises alkoxy species, resulting in enhanced synthesis of C_{3+} alcohols. Furthermore, the addition of (Me)-promoters into the K-MoS_2 supported catalyst demonstrated a strong ability to promote alcohol chain growth, resulting in the observed increase in BuOH-1 synthesis.

The coupling of ethanol or ethanol-derived species to yield 1-butanol seems to occur through an aldol condensation pathway, this suggests that a feasible approach to chain development utilizing this catalyst might be via alcohol coupling. The degree of the K-Mo interaction has been shown to be related to the degree of C_{3+} alcohol over sulfided materials [125]. The surface "K-Mo-S" species and Mo (CUS) sites are usually thought to be responsible for the synthesis of alcohol and HC, respectively. K-incorporation affects the active phase shape by increasing the crystalline size and stacking number of MoS_2 particles. Unmodified MoS_2 catalysts convert most syngas to hydrocarbons, and the

addition of an alkali metal modifies the dispersity of the active phase, resulting in the production of a structure-forming property [130–132]. K-species, as shown in [131], may impact the microstructure, surface morphology, and electronic properties of active MoS_2 phases, as well as produce distinct oxidized intermediates.

In [133,134], it is suggested that the promoter atoms function as electron density acceptors on the S-edge of the crystallites, reducing hydrogenation and deactivating the S-edge, resulting in improved selectivity/yield towards alcohols at the expense of hydrocarbons. Me-addition also increases the formation of MoS_2 crystallites, increasing the number of layers and linear dimension, all of which impact catalytic activity. As a consequence, the number of active centers on crystallite edges increases while the number of active centers of hydrogenation on the rims reduces, and when MoS_2 is promoted with d-metal, Co, Ni or Fe, a mixed Me-Mo-S phase is formed. At this phase, promoter atoms replace some Mo-atoms at the crystallite edges. The promotion of the S-edge with a single Me-atom result in the formation of inactive (K)MeMoS sites that are incapable of activating hydrogen. Double sulfur vacancies occur on the M-edge at CoMoS and K-MeMoS sites and may participate in the conversion process. According to [43], on the M-edge, double sulfur vacancies occur at MeMoS (Me = Fe, Co, Ni) and K-MeMoS (Me = Co, Ni) sites, and these vacancies are capable of engaging in conversion. When K-modification and Me-promotion were combined into MoS_2/C_{AG-3}, all catalysts exhibited a significant difference in activity, which might be ascribed to vacancies formed during Me-promotion and K-modification of MoS_2 catalysts. Overall, K-free catalysts had higher catalytic activity (i.e. total ethanol conversion) than their counterparts, and the incorporation of promoter atoms influenced product selectivity.

On these bases, it is widely known that reactivity on MoS_2-based catalysts occurs mostly at coordinatively unsaturated sites (CUS) produced at the catalyst's edges by (Co/Ni)MoS_2. Despite substantial study into the form of MoS_2 in hydrotreating, the specific structure of the active site remains an unresolved research subject [135–138]. However, it is widely accepted that MoS_2 forms platelets with interchanging Mo and S edge terminations, and that catalysis takes place at some of these edges [19,136]. The

frequency of such transformations determines the catalytic activity. The edge termination determines the coordination environment of CUS-Mo atoms on that edge. The coordination environment affects the strength of the Mo-S bonds, and hence the ease with which sulfur vacancies may be formed, as well as how the CUS Mo sites interact with reactants, intermediates, and products [31,36].

3.2 Effect of Granular and Fiber-Activated Carbons on Ethanol Dehydrogenation

The section studies the influence of novel fiber- and granular-activated carbon materials on the activity of supported, modified transition metal sulphide catalysts in ethanol conversion. The catalysts were characterised by SEM/EDX and TEM to investigate the morphology, N_2 physisorption to investigate the change in textural properties of the supports after impregnation of active phase precursors, XRF to investigate the composition of the catalysts, and UV spectroscopy of pyridine-adsorption to measure the total acidity of the samples.

3.2.1 Results

3.2.1.1 Catalyst Characteristics

Four novel types of supports, including two granular and two fiber-AC supports, were selected as supports the synthesis of K-promoted CoMo catalysts. The catalysts were composed of 10wt.% K, 3.7wt.% Co, and 12wt.% Mo. The textural properties of the DAS, K-$CoMoS_2$/DAS, YPK-1, and K-$CoMoS_2$/YPK-1 catalysts are depicted in **Table 3.3**.

The BET surface areas of K-$CoMoS_2$/DAS and K-$CoMoS_2$/YPK-1 were observed to be significantly lower at 249.45 m^2g^{-1} and 177.76 m^2g^{-1}, respectively, in comparison to the parent DAS (723.58 m^2g^{-1}) and YPK-1 (771.29 m^2g^{-1}). In addition, it was observed that the microporous structure of the K-CoMoS2/DAS catalyst exhibited a significantly higher value of 243 m^2g^{-1} compared to the K-$CoMoS_2$/YPK-1 catalyst, which had a microporous structure value of 142 m^2g^{-1}.

Table 3.3. Surface area and pore characteristics for AC-supported K-$CoMoS_2$ catalysts.

Catalysts	DAS	YPK-1	K-$CoMoS_2$/DAS	K-$CoMoS_2$/YPK-1
S_{BET} (m^2/g)	724	771	250	178
S_{micro} (m^2/g)	662	660	243	142
S_{meso} (m^2/g)	62	51	7	35
V_{total} (cm^3/g)	0.34	0.32	0.11	0.09
V_{micro} (cm^3/g)	0.28	0.27	0.10	0.06
V_{meso} (cm^3/g)	0.06	0.05	0.01	0.03
D_p (nm)	3.2	3.9	3.3	3.2
NS_{BET}	–	–	0.46	0.31
BE	–	–	0.54	0.69
%ME	0.18	0.16	0.11	0.33

S_{meso} = S_{BET} − S_{micro}; micropore volume calculated by t-plot method; mesopore volume calculated by BJH method;

NS_{BET} — normalized BET surface area;

BE-blocking extent of the pores of the support due to metal loading calculated by BE = 1 – NS_{BET};

%ME - mesoporosity calculated via the ratio of mesopore volume to total pore volume.

However, the mesoporous structures of the two catalysts displayed an opposite trend, with the K-$CoMoS_2$/DAS catalyst having a value of 7 m^2g^{-1} and the K-$CoMoS_2$/YPK-1 catalyst having a value of 35 m^2g^{-1}. The primary cause of the decrease in surface area was attributed to the obstruction and collapse of porous structures that occurred during the deposition of metals in a sulfide state onto the support. The broad expanse of the surface may suggest the presence of minute pores, measuring around 2 nm, which could become obstructed during the production of catalysts, particularly when significant loadings are expected. In comparison to DAS and YPK-1 supports, K-$CoMoS_2$/DAS and K-$CoMoS_2$/YPK-1 exhibited a decrease in pore volume, with values decreasing from 0.34 to 0.11 cm^3g^{-1} and 0.32 to 0.09 cm^3g^{-1}, respectively. The D_p value

of K-$CoMoS_2$/DAS exhibited an increase from 3.169 to 3.285 nm subsequent to the metal-loading process. The authors Surisetty et al. [139] postulated that the introduction of metal could potentially hinder the micropores within the support.

Table 3.4 depicts the elemental compositions of the stabilized catalysts. Based on these observations, it seems that the great majority of precursors were deposited on the support surface during the early stages of wetness impregnation. The observed K composition on both fibre and granular supports seems to vary with support type. The K loading was found to range between 8-11%, with a 30% variation. We assume that a considerable amount of K was deposited on the actual surface of the support on the fiber-supported catalysts, while K was deposited within the pores on the granular-supported catalysts.

Table 3.4. Composition of prepared catalysts based on X-ray fluorescence spectroscopy data.

Catalysts	**Targeted Compositions (wt. %)**			**Measured Compositions (wt. %)**		
	K	**Co**	**Mo**	**K**	**Co**	**Mo**
K-$CoMoS_2$/DAS	10	3.7	12	8.5	3.7	11.9
K-$CoMoS_2$/YPK-1	10	3.7	12	8.4	3.9	15.8
K-$CoMoS_2$/TCA	10	3.7	12	11.3	4.2	13.9
K-$CoMoS_2$/AHM	10	3.7	12	11.1	4.6	15.1

Table 3.5 shows the findings of pyridine-TPD adsorption studies used to assess the acidities of the supports and catalysts. It should also be highlighted that pyridine is preferentially absorbed at very acidic sites [140,141]. Thus, the acidity of the DAS granular material is comparable to that of the AHM fabric material, and the acidity of YPK-1 is comparable to that of TCA, demonstrating that acidity is determined by the material's composition and physical-chemical properties such as acidity, porosity, and so on. Similarly, catalysts deposited on the granular support have substantially lower acidity than the support itself, but catalysts deposited on the fibre support have much higher acidity than the original equivalent fibre support.

Table 3.5. Comparison of total acidity of $KCoMoS_2$ catalysts supported on fiber- and granular activated carbons.

Catalysts	Acidity (μmol.g^{-1})
DAS	65.81
YPK-1	39.31
AHM	79.67
TCA	47.37
K-$CoMoS_2$/DAS	21.19
K-$CoMoS_2$/YPK-1	24.05
K-$CoMoS_2$/AHM	156.43
K-$CoMoS_2$/TCA	165.81

The N_2 sorption isotherms for the K-$CoMoS_2$/DAS and K-$CoMoS_2$/YPK-1 catalysts are shown in **Figure 3.9a**, while the corresponding pore size distributions are shown in **Figure 3.9b**. Both AC-supported catalysts exhibited a typical Type I isotherm, which is a feature of N_2 adsorption in microporous materials, according to IUPAC classification [116]. This might be owing to the presence of tiny micropores. Microporous materials having small external surfaces (e.g., activated carbons, molecular sieve zeolites, and some porous oxides) offer Type I isotherms [116]. Furthermore, both isotherms for DAS- and YPK-1-supported catalysts exhibit an H4 hysteresis loop. Type H4 loops are typically seen in conjunction with thin slit-like pores [142,143]. Furthermore, before capillary condensation starts, micropores are filled at a low relative vapour pressure, but mesopores are filled at a greater relative pressure once capillary condensation occurs. The pore size distribution profile of the DAS- and YPK-1-based catalysts is restricted. This phenomenon, according to [144], might be caused by the development of pores of varying diameters. The holes in the lower size range might be caused by a blockage in the pore channels of the support, whilst the pores in the mid-size range could be caused by the collapse of smaller pores in the lower size range. Furthermore, the typical large pore size distribution may produce pore blockage, compromising the catalyst's diffusional capabilities during product synthesis. Because of the very low or negligible surface area of the fiber-based catalysts, we were unable to assess their textural properties; hence, the isotherms for the fiber-AC-supported catalysts are not provided. Fibers have a very low surface area, less than 1 $m^2.g^{-1}$, and it has been

shown that the N_2 sorption technique is inefficient at low surface area ranges, less than and about 1 $m^2.g^{-1}$, and that nitrogen is insufficient [145].

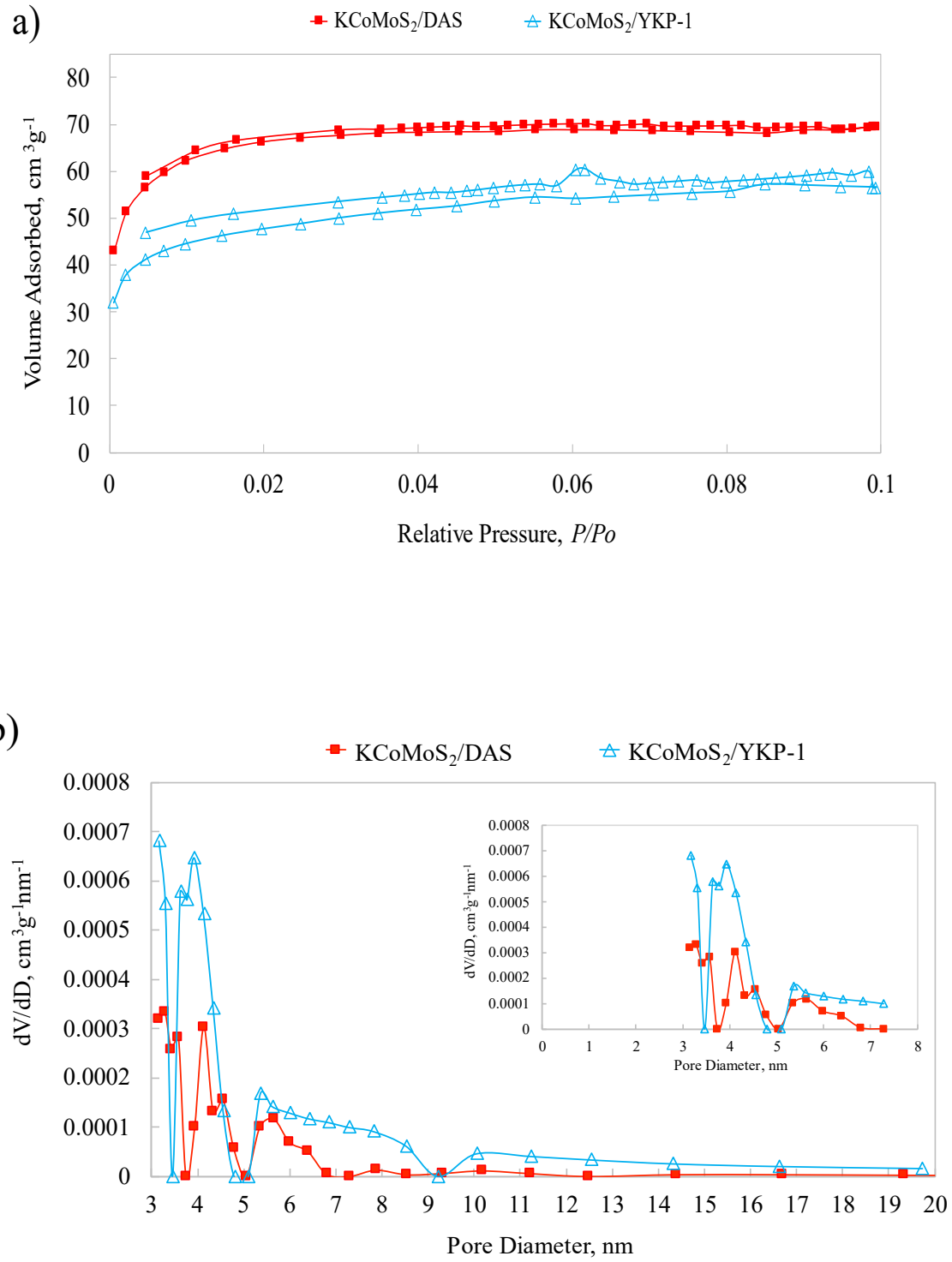

Figure 3.9: Characterization of the **granular**-activated carbons: (**a**) N_2 (77K) adsorption–desorption isotherms and (**b**) pore size distribution.

3.2.1.2 SEM and TEM

Figure 3.10 shows granular-AC-supported K-$CoMoS_2$/DAS and K-$CoMoS_2$/YPK-1 catalysts with a porous structure with a high degree of uneven porosity. The non-uniform porosity structure of both catalysts is most likely caused by a range of small- and large-particle aggregations. K-$CoMoS_2$/AHM and K-$CoMoS_2$/TCA, on the other hand, have a thin, flexible, threadlike morphology with a strip-axial pattern and a few longitudinal gaps, as well as a large fraction of irregular particles dispersed predominantly on the respective materials' fiber-AC surfaces. On the other hand, it seems that active metals are deposited more unevenly on the support surface with the fiber-AHM than with the fiber-TCA.

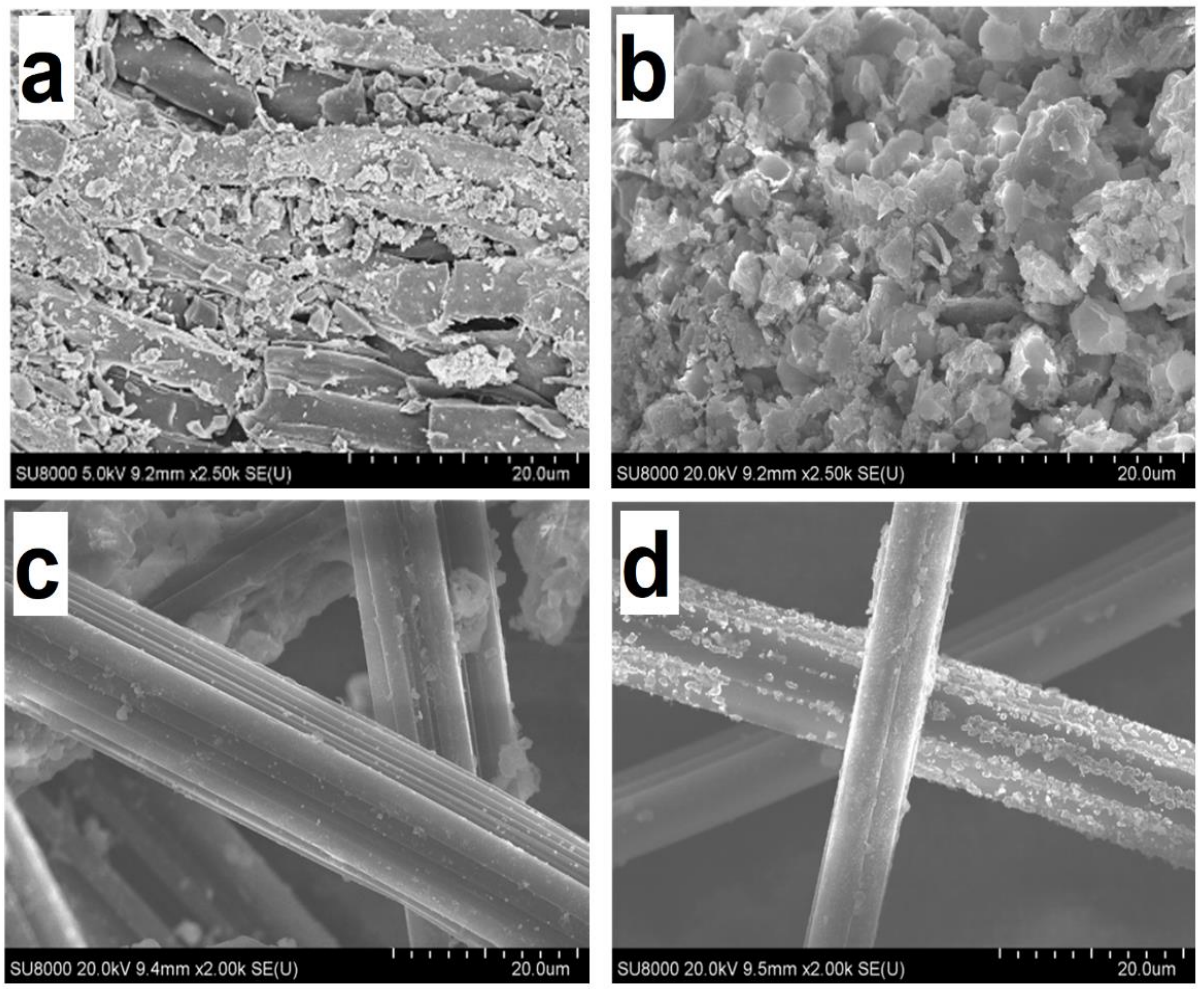

Figure 3.10. SEM images of (**a**) K-$CoMoS_2$/DAS; (**b**) K-$CoMoS_2$/YPK-1, (**c**) K-$CoMoS_2$/AHM, and (**d**) K-$CoMoS_2$/TCA.

The distributions of K, Co, Mo, and S were investigated using energy dispersive X-ray spectroscopy (EDX) (**Figure S3.1**). The SEM/EDX spectrum mapping verifies the formation of MoS_2 species during the sulfidation process, and K/Co species are homogeneously distributed on the MoS_2 phase, which produces a single phase and a uniform phase. The mapping of the elements also gives indirect evidence for the development of MoS_xO_y oxysulfide species as well as a Co-Mo-S phase. An EDX spectrum indicated that the K-$CoMoS_2$ catalyst supported on DAS had impurities such as Fe, Ca, Si, P, Cr, and S on its catalytic surface. The remaining samples had no signs of contaminants. The contaminants seen on DAS support might be related to the preparation source.

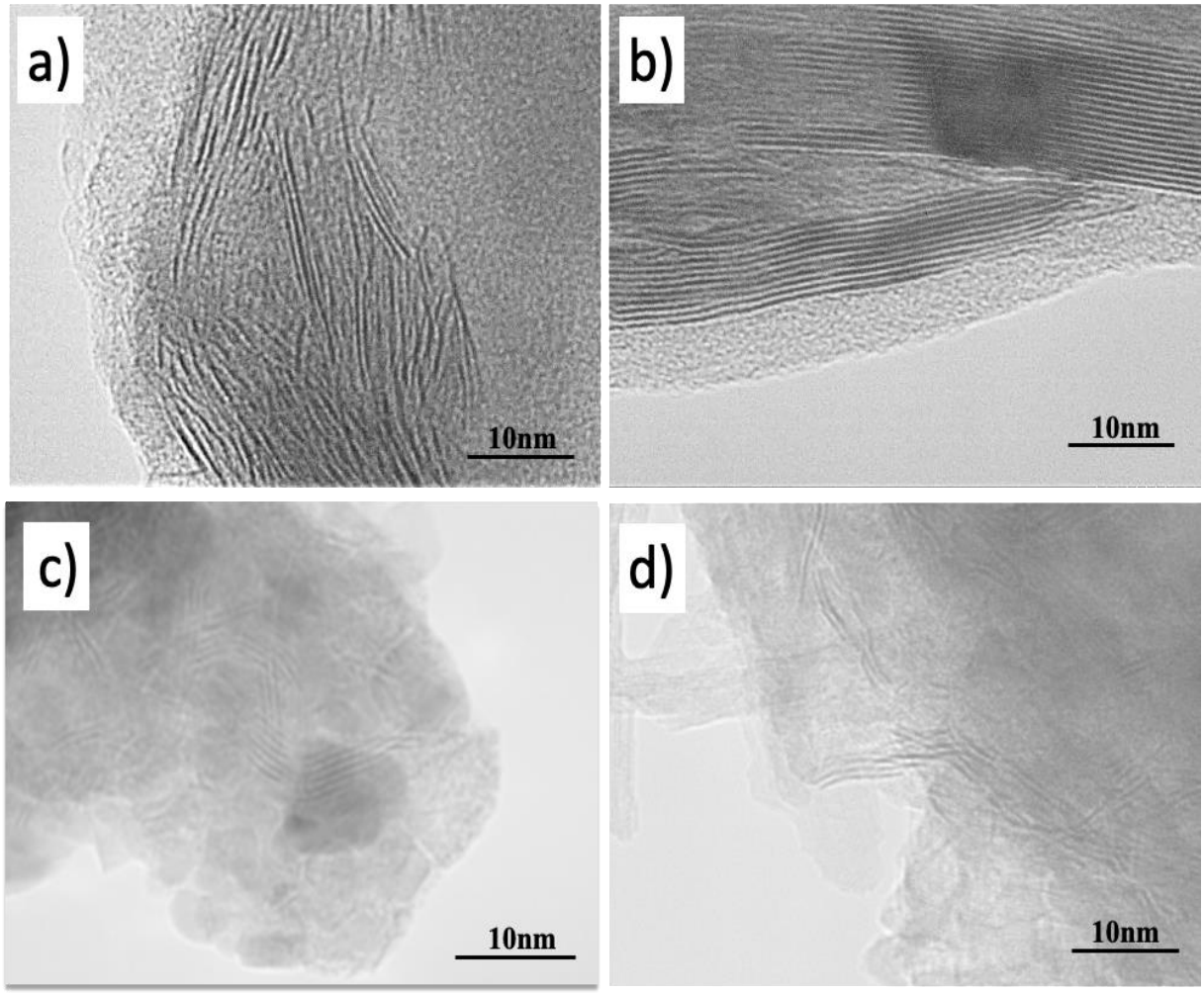

Figure 3.11. TEM images of K-$CoMoS_2$/DAS (**a**), K-$CoMoS_2$/YPK-1 (**b**), K-$CoMoS_2$/AHM (**c**), and K-$CoMoS_2$/TCA (**d**).

Figure 3.11 depicts TEM analysis of the microstructure and morphology of sulfided catalysts with MoS_2-like species [41]. The TEM micrographs reveal the typical layered structure of MoS_2, with randomly aligned crystallites. As can be observed, the granular-activated-carbon-based catalysts had substantially bigger and longer layered MoS_2 crystallite structures than their counterparts. The interaction between the active phase and the support might result in the formation of type-I or type-II multilayered phases, explaining the variance in crystallite shape. The surface morphology of MoS_2-based catalysts has been reported to be a result of the decorating of K on the edges of MoS_2-slabs, resulting in a K-decorated MoS_2-phase [33,131].

The TEM surface analysis indicates structural variations in MoS_2 crystallites that may be caused by K-intercalation. Interplanar distance between MoS_2 phases is increased by K-intercalation [51,53]. K-intercalation between MoS_2 planes has the potential to increase the d-spacing of (002) planes from 6.2 to 8.4 nm. The authors demonstrate how intercalation evolves over time. Dorokhov et al. [146] postulated that K-intercalation in MoS_2 interlayer space generates alcohols and changes catalytic activity. Furthermore, a K-promoter may influence the shape and microstructure of active phases, while the support can influence the location of active MoS_2-like species (K-decorated MoS_2 and K-intercalated MoS_2).

3.2.1.3 Catalytic Tests

The direct conversion of ethanol to various oxygenates was carried out to study the catalytic properties of the supported K-$CoMoS_2$ catalysts. **Figure 3.12** depicts the experimental data, including the ethanol conversion (%), total liquid product (LP_{total}), hydrocarbons (HC_{total}), and LP_{total}/HC_{total} ratio. On the fiber-AC-based catalysts, the maximum activity for the ethanol reaction was reported, and the conversion increased as follows: (38.7%) K-$CoMoS_2$/YPK-1 < (49.5%) K-$CoMoS_2$/DAS < (58.2%) K-$CoMoS_2$/TCA < (67.1%) K-$CoMoS_2$/AHM. The observed differences in catalytic activity may be due to the surface morphologies of the catalysts, the amount to which the support interacts with the active phase, and the type and textural features of the support used. It should be noted that, although fiber-AC-based catalysts have the maximum activity, the

conversion rate is considerably higher due to enhanced HC_{total} synthesis, while granular-AC-supported catalysts have the reverse tendency, with the following rise in LP_{total}: K-$CoMoS_2$/TCA < K-$CoMoS_2$/AHM < K-$CoMoS_2$/YPK-1 < K-$CoMoS_2$/DAS. Furthermore, the higher overall activity of the fiber-based supported catalyst may be related to mass-transfer limits when compared to the microporous AC.

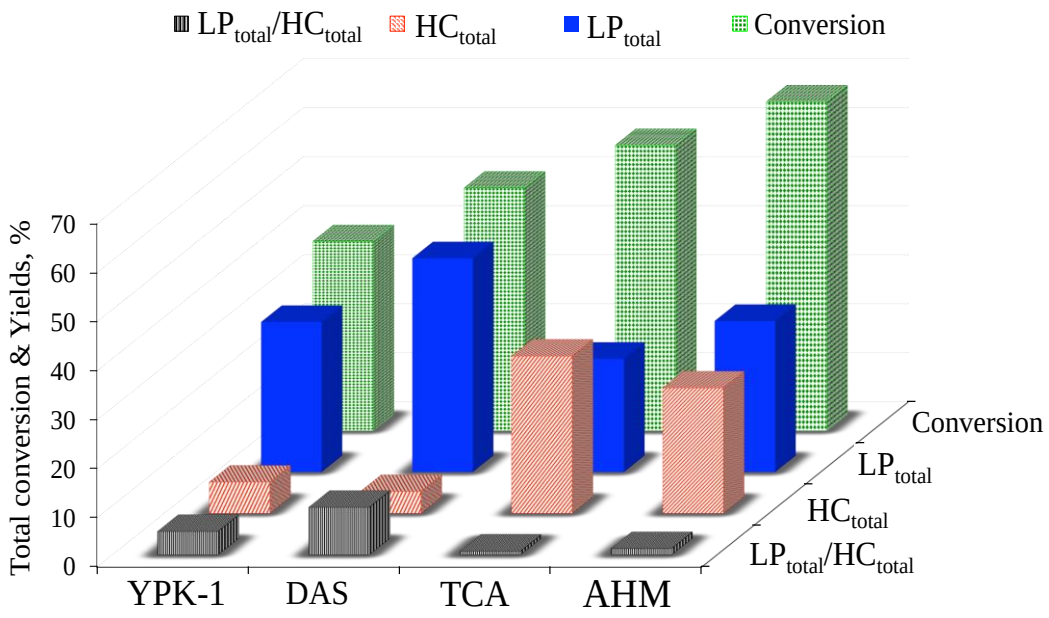

Figure 3.12: Dependence of total liquid product yields (LP_{total}) and hydrocarbon (HC_{total}) yields on conversion. Reaction conditions: T = 320 °C, m_{cat} = 3 g, P = 2.5 MPa, GHSV = 760 L h^{-1} kg_{cat}^{-1}, and feed flow rate = 0.3 mL/min under He atmosphere.

In contrast to the two granular supported catalysts, the catalyst with the highest proportion of micropores, K-$CoMoS_2$/DAS (49.5%), was shown to be more active than K-$CoMoS_2$/YKP-1 (38.6%). As per the findings of Osman et al. [147,148], the amount of microporous surface area in a catalyst improves its activity toward CO hydrogenation. This seems to be the situation with ethanol conversion. A comparable impact of microporous on catalytic activity was observed. Catalysts with a higher microporous content were shown to be more active. The findings reveal that increasing the surface area of the MoS_2-based catalysts improves their catalytic activity. It is widely documented [149,150] that supporting the Mo active phase on a high-surface area material, such as ACs, may be favourable because it increases the number of active sites by enhancing metal particle dispersion and distribution throughout the support surface. Despite the

equivalent difference in pore capacity, K-$CoMoS_2$/DAS has a slightly increased V_{total} and V_{micro}, resulting in improved catalytic activity. This supports the findings of [151], although in CO conversion, the catalyst with a greater pore capacity was shown to permit higher conversion and enhance the yield of liquid products. Furthermore, a bigger catalyst pore diameter boosted catalytic activity. Because of diffusion limits, narrow holes are inactive, but excessively broad pores are more prone to coking. This highlights the significance of catalyst textural features in boosting their performance in targeted commodities.

Figure 3.13 depicts the obtained product distribution as well as the GC analysis of the reaction products identified as aldehyde, esters, C_{3+} alcohols, hydrocarbons, and CO/CO_2. It is well known that ethanol dehydrogenates to directly produce acetaldehyde and dehydrates to form C_2H_4 and diethyl ether through the parallel reaction network, whilst additional products are produced as secondary reaction products formed by aldol condensation and coupling processes. It is worth noting that only trace amounts of diethyl ether and CO were reported on the K-$CoMoS_2$/TCA catalyst. This could be due to the fact that ether is generally unstable and rapidly decomposes into the equivalent olefin. The synthesis of AcH and C_2H_4 demonstrates that this catalytic system is capable of catalyzing both dehydrogenation and dehydration processes. The product distribution results further provide evidence of the increased synthesis of HC over fiber-based rather than granular-based catalysts, especially for C_2 hydrocarbons. n-PrOH and BuOH were produced in greater amounts over granular-based catalysts than their equivalents. Surprisingly, it seems that the yield of the aldol condensation product, BuOH, was precisely proportionate to the quantity of AcH generated. A decrease in AcH seems to enhance aldol-type condensation. While AcH seems to be the second most produced liquid product, no apparent association was found between its synthesis for both fiber- and granular-based catalysts. It was produced at a greater yield than K-$CoMoS_2$/AHM, about two to three times higher than the yield obtained with the other catalysts examined. A significant quantity of EAA was also identified, suggesting that it was formed by the C-C bond formation process, which occurs when two esters or one ester react with another carbonyl molecule in the presence of a strong base via the Claisen condensation process.

A reaction route for ethanol over K- and Co-promoted MoS_2-supported catalysts was presented in our previous study [152].

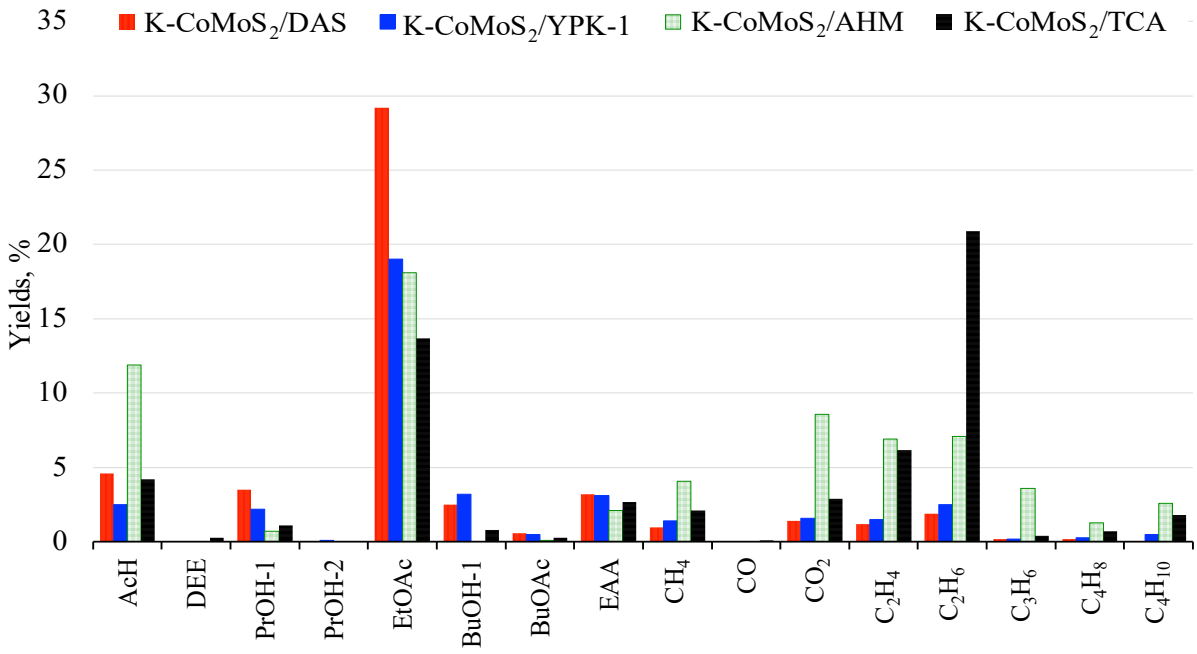

Figure 3.13. Product yields over K-$CoMoS_2$ catalysts on various supports under the standard conditions. Reaction conditions: T = 320 °C, P = 2.5 MPa, m_{cat} = 3 g, GHSV = 760 L h^{-1} kg_{cat}^{-1}, and feed flow rate = 0.3 mL/min under He.

EtOAc was synthesised in considerable amounts across all liquid products and catalysts, with yields increasing as follows: K-$CoMoS_2$/TCA < K-$CoMoS_2$/AHM < K-$CoMoS_2$/YPK-1 << K-$CoMoS_2$/DAS. It has been shown that dehydrogenation of ethanol using transition metal-containing catalysts provides a significant quantity of ethyl acetate [111,153]. The interaction of the first formed AcH with the surface ethoxy group or ethanol molecules results in the production of ethyl acetate during ethanol breakdown on heterogeneous transition metal catalysts, according to Szymanski et al. [154]. The adsorbed ethoxy species is dehydrogenated to produce an acetyl species, and the acetyl and ethoxy species react to make adsorbed EtOAc, which finally desorbs. Previous research [155] [122] indicates that the synthesis of ethyl acetate is the product of two sequential processes, (xii) and (xiii), with the synthesis of acetaldehyde functioning as an intermediary step. To obtain high selectivity to ethyl acetate, the partial pressure of

acetaldehyde in the system must be reduced. (xii) A quick reaction rate reduces acetaldehyde concentration, which enhances selectivity to ethyl acetate [122].

$$CH_3CH_2OH \rightarrow CH_3CHO + H_2 \quad \text{(xii)}$$

$$CH_3CH_2OH + CH_3CHO \rightarrow CH_3COOCH_2CH_3 + H_2 \quad \text{(xiii)}$$

3.2.1.4 Discussion

According to **Figure 3.14**, granular supports (DAS and YPK-1) possess active phase crystallites with a significant number of layers and a substantially longer length when compared to crystallites formed on fabric materials. It is hypothesized that the latter are positioned in "axial spots" on the surface of the fibres, covering substantially less area than the crystallites seen on the surface of DAS and YPK-1. As a result, the acid sites of the granular materials are blocked by crystallites of the active phase, while the acid sites of the fibre materials are more open and alter the acidity of the catalyst.

One point remains: why does the acidity of these fibre catalysts become greater than that of the original supports? It might be owing to the size of the produced particles. The majority of the active phase particles formed on fibre materials are 1-2-layered crystallites with typical sizes ranging from 2 to 6 nm. The number of longer particles in these catalysts is minimal.

The active phase put on granular supports has more particles with 6-8 stacks and a size larger than 10 nm. This suggests that the active phases of AHM and TCA catalysts, which are composed of tiny, low-layered crystallites, contain more coordination-unsaturated sites (CUS) than the phases of granular catalysts, which are composed of bigger particles. CUS are recognized for their strong acidity. Furthermore, hydrogen spillover may play a role in the acidification of active sites on fibre supports. The greater the proportion of free surface, the greater the hydrogen spillover. Thus, the decrease in the acidity of the catalysts carried on the granular materials and the increase in the acidity of the catalysts deposited on fiber materials can be explained by three interrelated factors: (i) the difference in the active phase particle sizes, (ii) the difference in the number of

CUS located on large and small particles, and (iii) hydrogen spillover on the surface free of particles of the active phase.

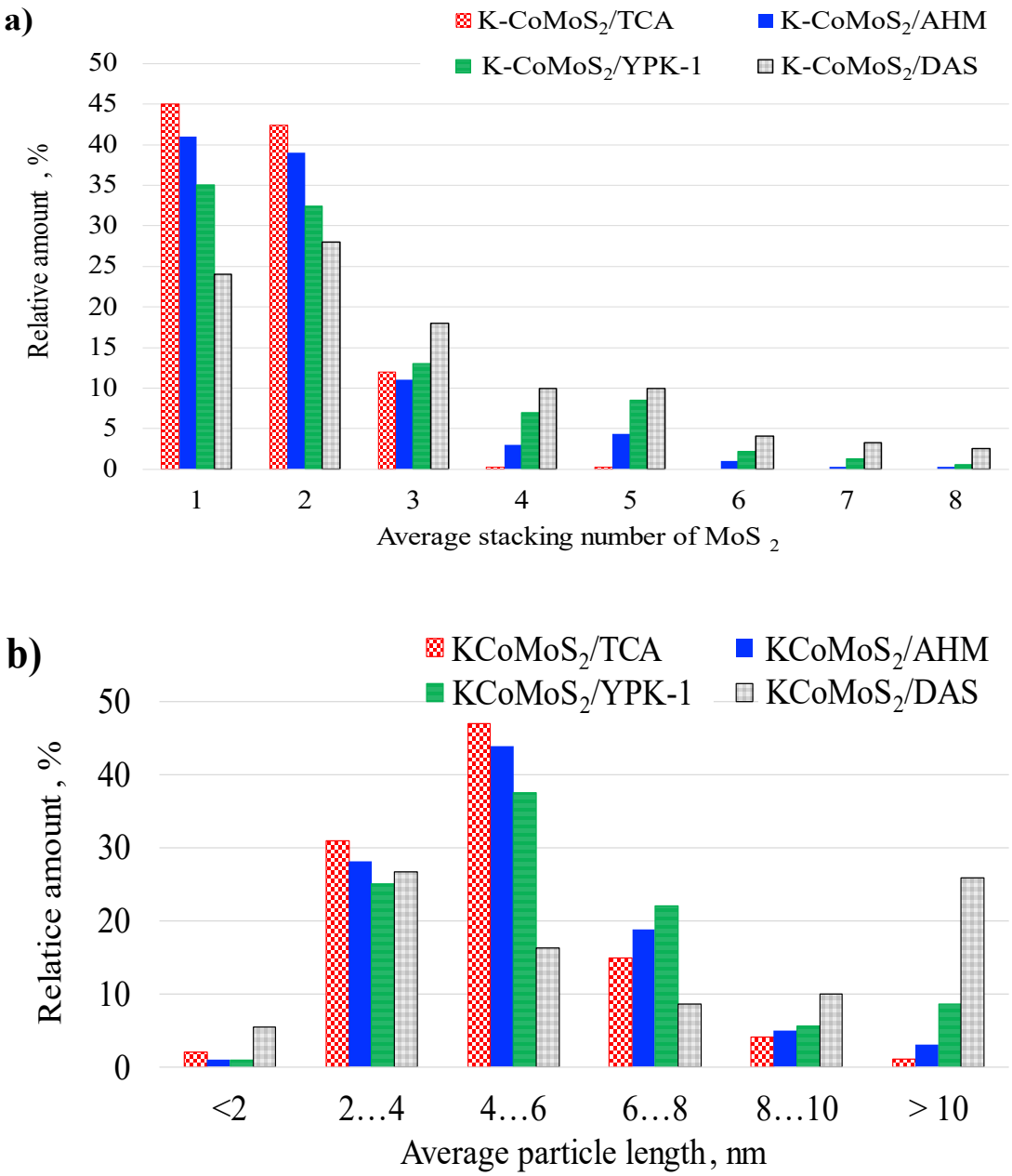

Figure 1.14. Distributions of stacking number of MoS_2 particles obtained from minimum 500 individual slabs per sample as recorded from TEM image (**a**), and of particle length of MoS_2 particles (**b**) for K-$CoMoS_2$ supported of activated carbons TCA, AHM, YPK-1 and DAS.

These considerations relate to data on liquid reaction product conversion and yield on granular and fibre catalysts (**Figure 3.12**). Catalysts deposited on fiber supports show a higher degree of conversion compared to catalysts on granular supports. Furthermore, they produce more gaseous products than granular catalysts. At the same time, granular

catalysts produce more liquid products (mostly alcohols). Indeed, if hydrogenation and chain-breaking (cracking) reactions occur at CUS, which are positioned on rims and solid angles, the synthesis of alcohols happens on the edges, according to the "Rim-edge" concept [19,156–158]. As a result, the larger the yield of alcohols, the longer the edge of the crystallite (more layers and a higher stacking number) and the longer its linear dimension.

Figure 3.15 shows the acidity of the catalyst as a function of (a) ethanol conversion and (b) product yields. The increasing surface acidity of the catalyst promotes HC_{total} synthesis while inhibiting LP_{total} synthesis, whereas conversion (**Figure 3.15a**) rises. The most active catalysts (K-$CoMoS_2$/TCA and K-$CoMoS_2$/AHM) have the highest pyridine adsorption values (strong acid sites), while the least active catalysts (K-$CoMoS_2$/YPK-1 and K-$CoMoS_2$/DAS) have the fewest acidic sites. The enhanced acidity and activity may be related to the fiber-AC supports' lower ash content as compared to the granular-AC supports.

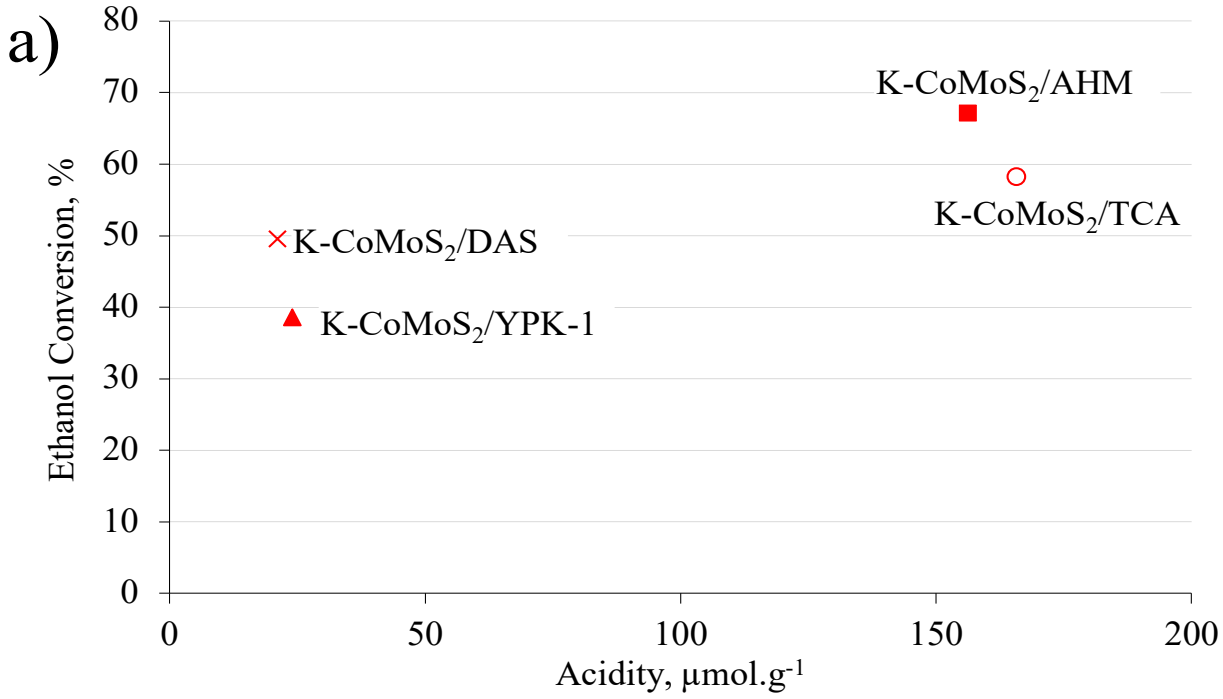

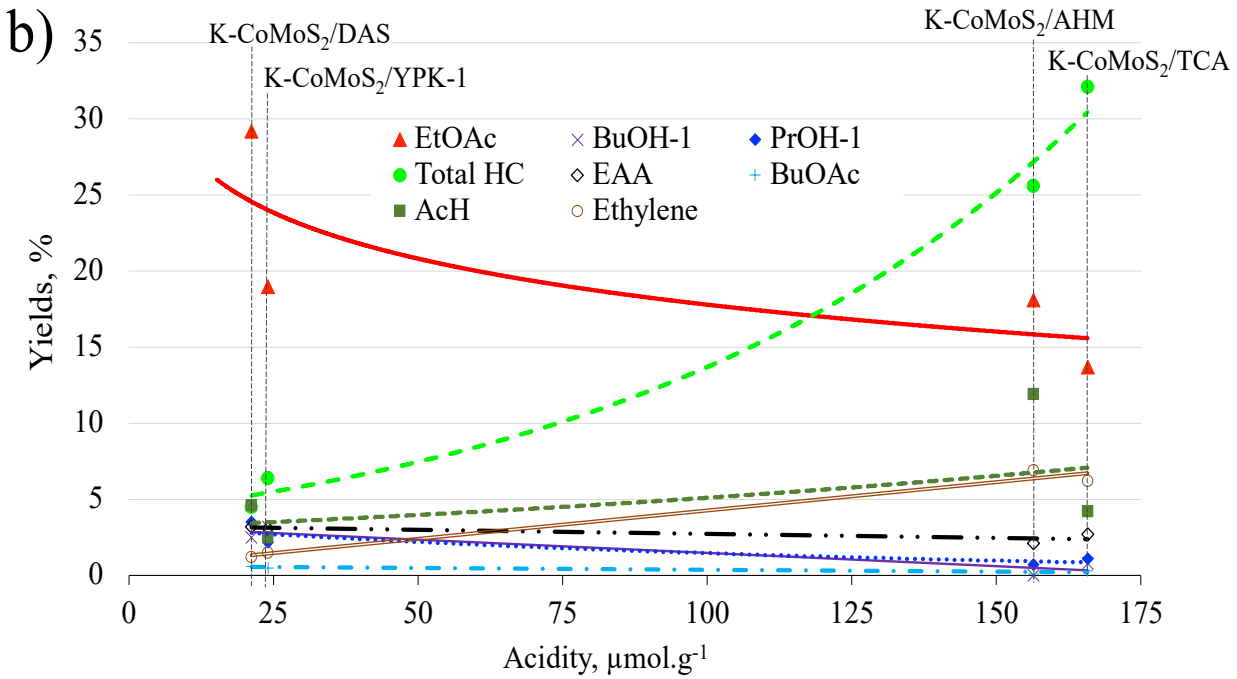

Figure 3.15. Total acidity as a function of (**a**) ethanol conversion and (**b**) product yields at 320 °C for all K-promoted trimetallic CoMo-supported catalysts (Reaction conditions: T = 320 °C, m_{cat} = 3 g, P = 2.5 MPa, GHSV = 760 L h^{-1} kg_{cat}^{-1}, and feed flow rate = 0.3 mL/min under He).

Figure 3.15b depicts the relationship between product yields and catalyst acidity. There is a clear relationship, and the results show that the acidity of the catalyst surface has a considerable impact on the synthesis of the desired products. The increased ethylene production found as catalyst acidity increased implies that the dehydration process requires the presence of strong acid sites in order to produce ethylene products. According to [159], acidic sites accelerate dehydration and the formation of C_2H_4. Furthermore, high acidity boosted HC synthesis, which was at its highest yields under the most acidic catalyst, K-CoMoS$_2$/TCA. Acidity increases alkane synthesis by promoting C-O cleavage through dehydration [160]. Reduced acidity may aid in decreasing deoxygenation and increasing oxygenate production. It also seems that lower acidity promotes an aldol-type condensation process, which resulted in a larger yield of higher alcohol, specifically, BuOH. According to León et al. [161], catalysts with higher basic site concentrations and strengths increase the synthesis of C_4-products (i.e., butanol-1), while the presence of acid sites promotes ethanol dehydration, resulting in reduced condensation efficiency. According to the studies [17,149], fundamental sites are required for ethanol

condensation into butanol-1. The somewhat greater butyl acetate yields in the less acidic samples, K-$CoMoS_2$/YPK-1 and K-$CoMoS_2$/DAS, indicate an aldol-type reaction.

As the acidity of the catalyst rises, the efficiency of acetate synthesis decreases [154]. EtOAc was discovered to decrease when the acidity of the catalyst increased as follows: K-$CoMoS_2$/TCA < K-$CoMoS_2$/AHM < K-$CoMoS_2$/YPK-1 < K-$CoMoS_2$/DAS. The production of ethoxide species has been linked to basic sites [162]. As a consequence, the findings indicate that ethoxide formation is a significant step in the synthesis of ethyl acetate, and it may even be the rate-limiting step under these circumstances. Because the EAA yield seems to be proportionate to the EtOAc yield, it appears to be a byproduct of ethyl acetate production. On one of the acidic K-$CoMoS_2$/AHM catalysts, AcH, the principal reaction product of dehydrogenation, was generated at more than double the rate of its closest analogue, with other catalysts performing roughly identically in their syntheses. However, it had a lesser yield than EtOAc. Secondary condensation products might contribute to the lower AcH levels. BuOH-1 seems to increase in proportion to the decrease in AcH yield. Carrasco-Marin et al. [111] discovered that the AcH dehydrogenation process happens on either Lewis acid or basic surface sites on both the exterior and interior surfaces. However, this might explain why no obvious link was discovered in the synthesis of AcH in relation to the textural features of the catalysts. K-$CoMoS_2$/AHM > K-$CoMoS_2$/DAS ≥ K-$CoMoS_2$/TCA > K-$CoMoS_2$/YPK-1 has the lowest activity for catalyzing ethanol dehydrogenation.

In addition, it was observed that an increase in acidity levels resulted in a slight reduction in pore volume, particularly in the case of catalysts supported by granular activated carbon. Anashkin et al. [163] reported that an increase in pore volume and liquid products resulted in a decrease in the overall acidity of MoS_2-based catalysts. Our findings are in line with the results obtained from the comparison of catalysts supported by DAS and YPK-1. The K-$CoMoS_2$/DAS exhibited a relatively higher pore capacity, lower acidity, and greater activity. The findings indicate that MoS_2 with reduced surface acidity exhibited greater LP synthesis activity, as depicted in **Figure 3.12**, in comparison to MoS2 with higher acidity and diminished pore volume. The results indicate that the support characteristics exert a noteworthy influence on both the catalyst's efficiency and

the yields of its products. The observed effect is in line with our previous research [152], which demonstrated that the catalytic activity is significantly impacted by the nature of the support.

3.3 Catalytic Conversion of Ethanol Over Supported K-$CoMoS_2$ Catalysts for Synthesis of Oxygenated Hydrocarbons

The section examines the catalytic activity of trimetallic K-$CoMoS_2$ catalysts supported by alumina, carbon-coated alumina (CCA), and two commercial activated carbons (AC). The structural properties and morphology of the supports and catalysts were investigated using HRTEM, UV spectrum analysis of pyridine adsorption, SEM/EDX, XPS, and N_2 physisorption. The effect of support type on the shape of MoS_2 crystallites was revealed. Turn over frequency (TOF) was determined to be affected by catalyst acidity, crystallite stacking number and length, and active site number.

3.3.1 Characteristics of Catalysts and Supports

Textural properties of the prepared CCA support vary from those of the Al_2O_3 support and activated carbons (**Table 3.6**). The CCA-supported catalyst (1.7% carbon content) had a lower specific surface area than the alumina-supported catalyst. In addition, the average pore capacity of CCA decreased marginally from 0.65 cm3/g Al_2O_3 to 0.63 cm3/g CCA. Coke formed on the alumina's surface obstructs the micropores, causing this condition.

BAW and AG-3 commercial activated carbon materials had a greater surface area but a lower total pore volume than CCA and Al_2O_3. BAW and AG-3 are carbon supports derived, respectively, from birch trees and coal. The type of the support influenced the pore sizes and morphologies significantly. The total pore volume decreased in the following order: AG-3 < BAW < CCA ≈ Al_2O_3. The micropore structure of alumina and CCA supports is insignificant, while activated carbon materials contain a significant micropore volume (about 0.3 cm^3/g). The mesopore volume of activated carbons AG-3

and BAW is quite modest at 0.10 and 0.13 cm^3/g, but the mesopore volume of Al_2O_3 and CCA supports dominates the overall pore volume of these materials (0.65 cm^3/g and 0.63 cm^3/g, respectively).

Table 3.6. Texture characteristics of the supports and catalysts measured by N_2 physisorption technique.

Sample	S_{BET},[a] m^2/g	S_{micro}, m^2/g	S_{meso},[b] m^2/g	V_{total}, cm^3/g	V_{micro},[c] cm^3/g	V_{meso},[d] cm^3/g	NS_{BET},[e]	BE,[f]	%Me,[g]
Al_2O_3	161	0	161	0.65	0.00	0.65	-	-	100
K-$CoMoS_2/Al_2O_3$	91	0	91	0.29	0.00	0.29	0.76	0.24	100
CCA	156	13	143	0.63	0.01	0.63	-	-	100
K-$CoMoS_2$/CCA	73	0	73	0.26	0.00	0.26	0.63	0.37	100
AG-3	854	753	101	0.45	0.35	0.10	-	-	22
K-$CoMoS_2$/AG-3	164	137	27	0.09	0.06	0.03	0.26	0.74	33
BAW	753	642	111	0.39	0.26	0.13	-	-	33
K-$CoMoS_2$/BAW	404	365	40	0.23	0.16	0.07	0.73	0.27	30

[a] BET surface area;
[b] $S_{meso} = S_{BET} - S_{micro}$;
[c] micropore volume calculated by t-plot method;
[d] mesopore volume calculated by BJH method;
[e] NS_{BET} – normalized BET surface area determined by équation (11);
[f] BE – blocking extent of the pores of the support due to metal loading calculated by BE = 1 – NS_{BET};
[g] mesoporosity was calculated via the ratio of mesopore volume to total pore volume.

SSA and total pore volume were decreased following loading the active phase onto alumina, CCA, and BAW, whereas only ~20% of SSA remained after loading the active phase onto the AG-3 support. Moreover, the pore structure of the alumina-based and AC-based carriers and related catalysts is extremely distinct. **Figure 3.16** depicts the pore sizes of Al_2O_3, CCA, AG-3, and BAW-supported catalysts.

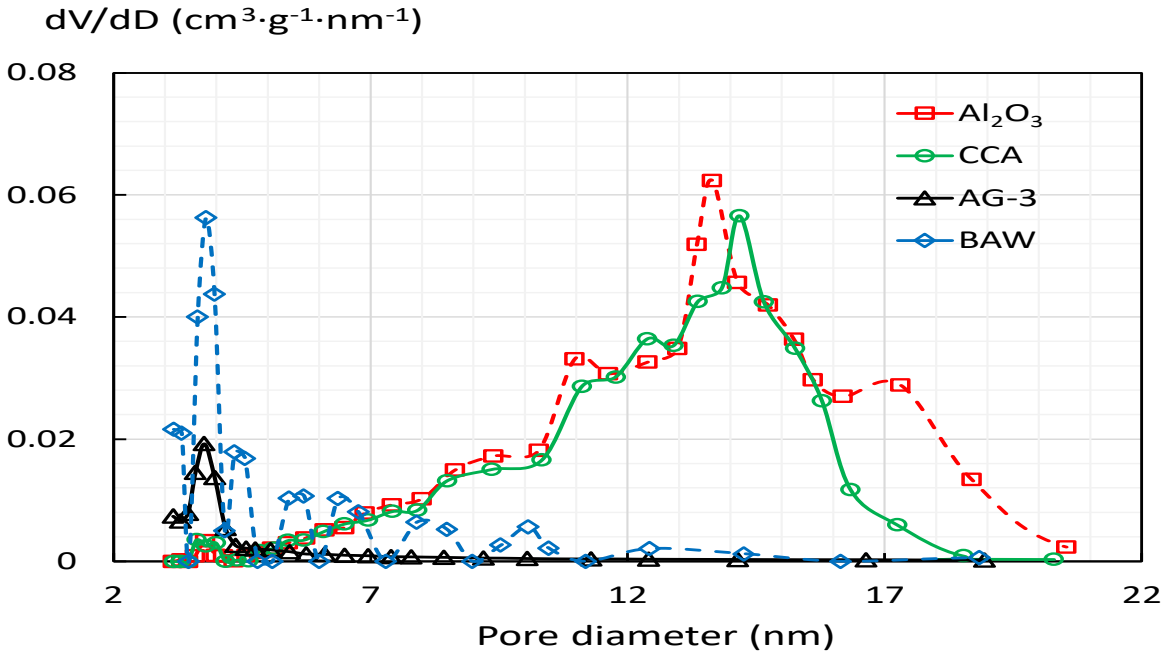

Figure 3.16. Pore size distribution of K-$CoMoS_2$/Sup (Sup = Al_2O_3, CCA, AG-3, BAW).

The alumina-based catalysts have wider pores, while those supported on AC are characteristic of a fine structure of narrow pores. The pore width increased in the order of K-$CoMoS_2$/AG-3 < K-$CoMoS_2$/BAW < K-$CoMoS_2$/CCA < K-$CoMoS_2$/Al_2O_3. Catalysts supported on AG-3 and CCA exhibited a unimodal distribution with average diameters of 3.8 and 14 nm, respectively. In contrast, BAW- and Al_2O_3-supported catalysts exhibited a multimodal distribution of pores. As shown in [164], multimodal pore size distributions are typical of fixed beds, which is particularly noteworthy since it enhances the active phase availability and even metal deposition, both of which are desired. Bimodal pore size distribution boosts the active surface area and enhances the activity of mesopores while protects them against poisoning by big molecules and metals.

3.3.2 SEM/EDX and TEM analysis

The SEM micrographs of K-$CoMoS_2$/Sup (Sup = Al_2O_3, CCA, AG-3, BAW) reveal a morphological distinction (**Figure 3.17**).

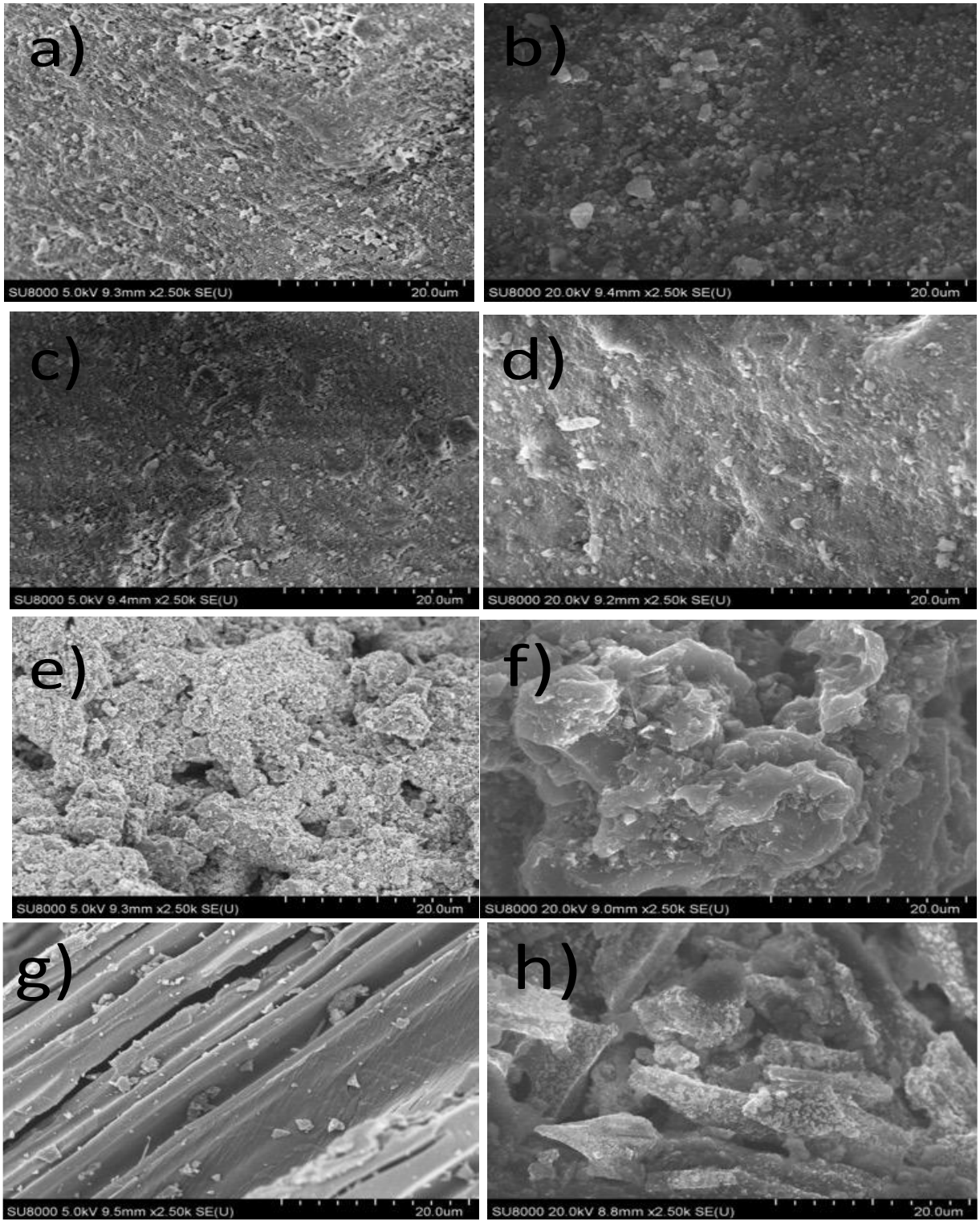

Figure 3.17. SEM images for: (a) Al_2O_3, (b) K-$CoMoS_2$/Al_2O_3, (c) C/Al_2O_3, (d) K-$CoMoS_2$/CCA, (e) AG-3, (f) K-$CoMoS_2$/AG-3, (g) BAW, (h) K-$CoMoS_2$/BAW.

Consequently, the average size of the particles generated on AC-supported catalysts (f, h) is greater than that on alumina and CCA-supported catalysts (f, h) (b, d). **Figure S3.2** displays EDX maps of the active phase components dispersed on the surface of K-$CoMoS_2$/Sup (Sup: a) Al_2O_3, b) CCA, c) AG-3, and d) BAW catalysts. Mo and S are coterminous with Co. This demonstrates the creation of CoMoS phase. Potassium is uniformly distributed on both the CoMoS active phase and the support material when there is no active phase, and it interacts with oxygen-containing functional groups on the support surface. Similar comparisons reveal the development of oxygen-containing functional groups on the carbon surface.

Figure 3.18 depicts representative HRTEM micrographs of four sulfided K-$CoMoS_2$/Sup catalysts. The MoS_2 slabs are represented by the black, thread-like fringes. The picture fringe spacing is roughly 0.65 nm, which corresponds to the typical (0 0 2) basal planes of crystalline MoS_2. HRTEM data were used to determine the average size of the MoS_2 phase (**Table 3.7**). The average phase size of MoS_2 crystallites ranged from 4.6 to 6.1 nm, while the average stacking number ranged from 1.7 to 2.6. When compared to the alumina-based sample, the carbon-containing catalysts had a greater stacking number and average slab length.

Table 3.7. Morphological characteristics of the sulfided K-$CoMoS_2$/Sup catalysts

Catalyst	Morphological characteristics		
	Average length,[a] $\bar{L}$ (nm)	Average stacking number,[b] $\bar{N}$	Dispersion of MoS_2 [c] particles, D
K-$CoMoS_2$/Al_2O_3	5.0	1.7	0.24
K-$CoMoS_2$/CCA	5.8	2.0	0.21
K-$CoMoS_2$/AG-3	6.6	1.8	0.18
K-$CoMoS_2$/BAW	10.6	1.9	0.12

[a] $\bar{L}$ (nm) determined from MoS_2 HRTEM results.
[b] $\bar{N}$ determined by HRTEM results (Equation (2)).
[c] MoS_2 dispersion calculated from HRTEM results (Equation (1)).

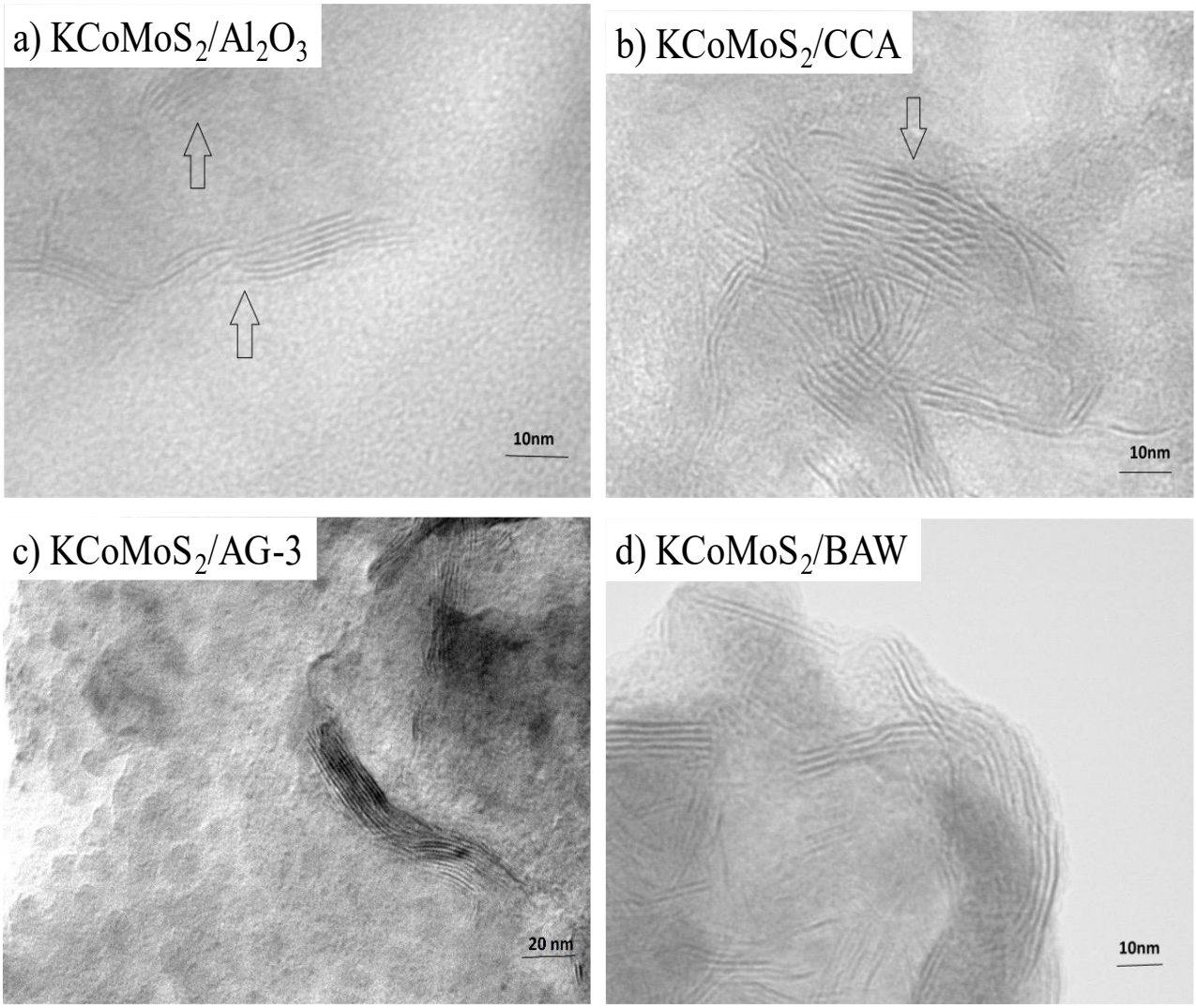

Figure 3.18. TEM images, MoS_2 crystallites distribution: degree of stacking numbers and particle length of (obtained from minimum 500 individual slabs per sample as recorded from TEM image): (a) K-$CoMoS_2/Al_2O_3$; K-$CoMoS_2$/CCA; (c) K-$CoMoS_2$/AG-3 and (d) K-$CoMoS_2$/BAW.

Table 3.8. Metal distribution for Co and Mo species present on the surface of the sulfided K-$CoMoS_2$/Sup catalysts (Sup = Al_2O_3, CCA, AG-3, BAW).

Catalyst	C_{CoMoS} [a] (wt. %)	Co percentage (%)			Mo percentage (%)			Co/Mo ratio	
		CoMoS	Co_9S_8	Co^{2+}	MoS_2	MoS_xO_y	Mo^{6+}	$(Co/Mo)_{slab}$ [b]	$(Co/Mo)_{edge}$ [c]
K-$CoMoS_2$/Al_2O_3	0.63	26	65	9	88	6	6	0.14	0.58
K-$CoMoS_2$/CCA	0.22	19	64	17	74	9	17	0.11	0.51
K-$CoMoS_2$/AG-3	1.67	34	45	22	94	0	6	0.16	0.79
K-$CoMoS_2$/BAW	1.17	31	44	25	73	13	14	0.22	0.87

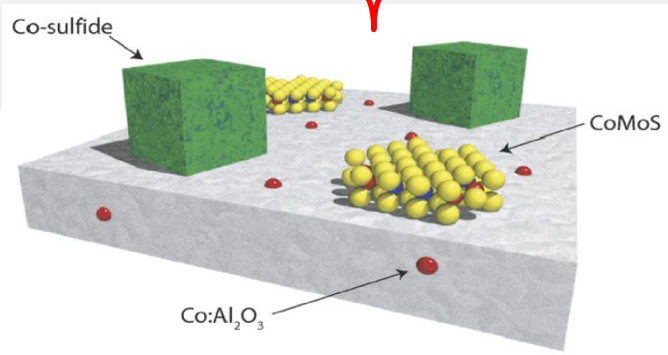

[a] Effective Co content in total CoMoS phase species from XPS results (Equation (iv)).

[b] Co/Mo ratio in the CoMoS slabs calculated from XPS results (Equation (v)).

[c] Co/Mo ratio in the CoMoS edges calculated from XPS and HRTEM results (Equation (vi)).

3.3.3 XPS analysis

Using XPS, the chemical species on the surface of K-$CoMoS_2$/Sup catalysts were investigated. **Figure 3.19** depicts the Mo 3d spectrum, which contains three Mo 3d doublets [108,165,166]. The Mo $3d_{5/2}$ and $3d_{3/2}$ doublets with BE values of 228,8 and 232,0 eV, respectively, correspond to the Mo^{4+} in the MoS_2 phase species. The doublet with BE equal to 230.0 and 233.2 eV is associated with the Mo^{5+} in the MoS_xO_y oxysulfide species, while the doublet with BE equal to 232.1 and 235.3 eV is associated with the Mo^{6+} oxide species. The EDX maps (**Figure S3.2**) demonstrate further, in conjunction with the EDX-XPS data, that S correlates with O. The XPS spectra offer direct evidence of the production of MoS_xO_y oxysulfide species. S 2s is attributed to the 226.1 eV peak at BE. Mo3d XPS spectra for the K-$CoMoS_2$/AG-3 catalyst vary considerably from those of other catalysts. In the intercalated K_x-MoS_2 phase, the Mo 3d binding energy is changed from 229.4 eV (2H-MoS_2) to 228.4 eV, indicating that potassium cation interaction stabilizes the 1T-MoS_2 phase [167]. Previously, it was observed [167] that the quantity of this K_x-MoS_2 phase had a strong correlation with its catalytic efficacy in the formation of methyl mercaptan from syngas and H_2S.

Figure 3.19 depicts three peaks with their associated satellites in the spectral area of Co $2p_{3/2}$. Cobalt is associated with the 778.6 eV peak at BE in the CoMoS species. The values at 778.1 and 781.5 eV, respectively, correspond to Co_9S_8 particles and Co^{2+} in an oxidizing environment [108,165,166]. The decomposition of the XPS spectra revealed metal distribution for the Co and Mo species (**Table 3.8**). The K-$CoMoS_2$/Sup catalysts are characterized by a comparable degree of sulfidation: the relative amount of cobalt in the CoMoS phase was in the range of 19-34 rel. % and molybdenum in the MoS_2 particles at the level of 73-94 rel. %.

There are somewhat more Co-promoted centers on carbon substrates, since the $(Co\text{-}Mo)_{edge}$ value for catalysts based on AG-3 and BAW is 0.21 to 0.36 times more than that of Al_2O_3 and CCA (almost 1.5 times). This may be explained by the decreased dispersion of active phase particles on carbon carriers, which, for the same Co/Mo ratio in all catalysts, promotes a more thorough decorating of MoS_2 edges by Co promoter atoms

a)

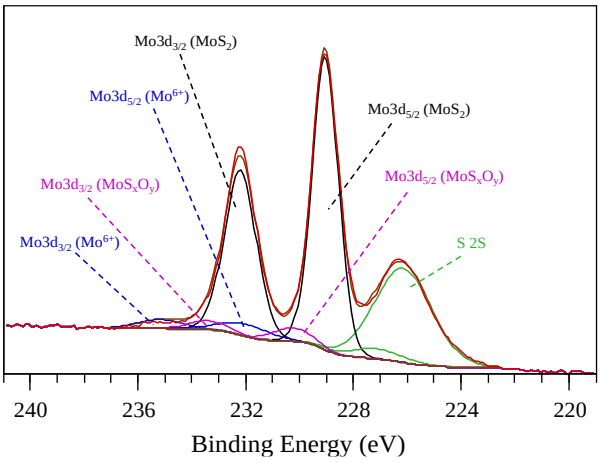
Mo3d3/2 (MoS2)
Mo3d5/2 (Mo6+)
Mo3d5/2 (MoS2)
Mo3d3/2 (MoSxOy)
Mo3d5/2 (MoSxOy)
Mo3d3/2 (Mo6+)
S 2S
240
236
232
228
224
220
Binding Energy (eV)

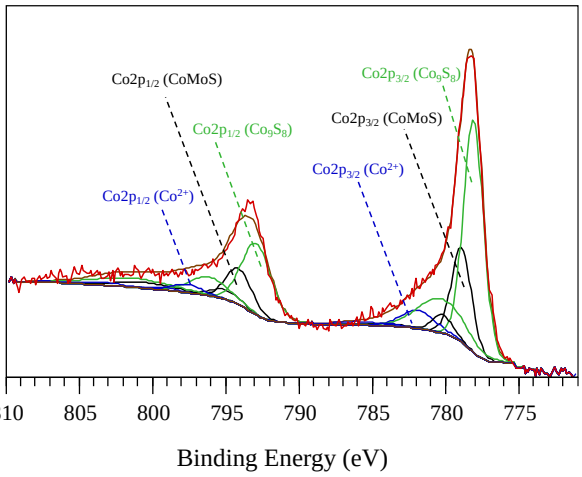
Co2p1/2 (CoMoS)
Co2p3/2 (Co9S8)
Co2p1/2 (Co9S8)
Co2p3/2 (CoMoS)
Co2p3/2 (Co2+)
Co2p1/2 (Co2+)
810
805
800
795
790
785
780
775
Binding Energy (eV)

b)

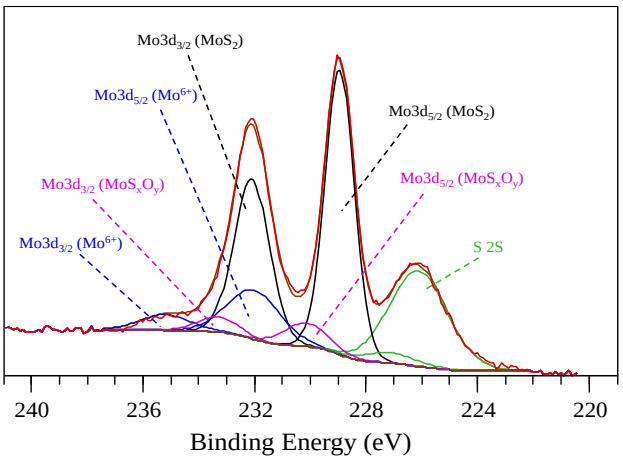
Mo3d3/2 (MoS2)
Mo3d5/2 (Mo6+)
Mo3d5/2 (MoS2)
Mo3d3/2 (MoSxOy)
Mo3d5/2 (MoSxOy)
Mo3d3/2 (Mo6+)
S 2S
240
236
232
228
224
220
Binding Energy (eV)

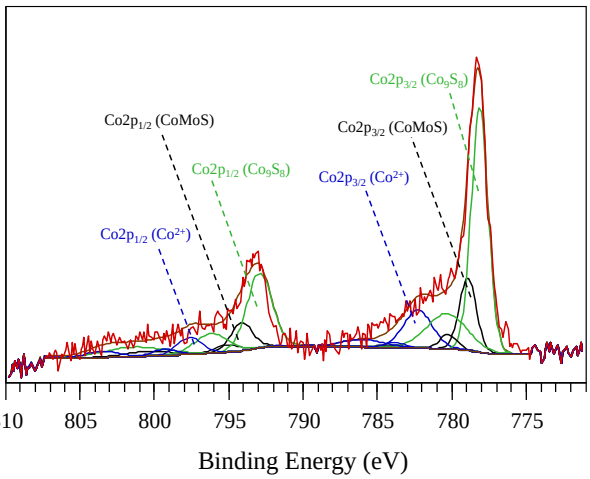
Co2p3/2 (Co9S8)
Co2p1/2 (CoMoS)
Co2p3/2 (CoMoS)
Co2p1/2 (Co9S8)
Co2p3/2 (Co2+)
Co2p1/2 (Co2+)
810
805
800
795
790
785
780
775
Binding Energy (eV)

c)

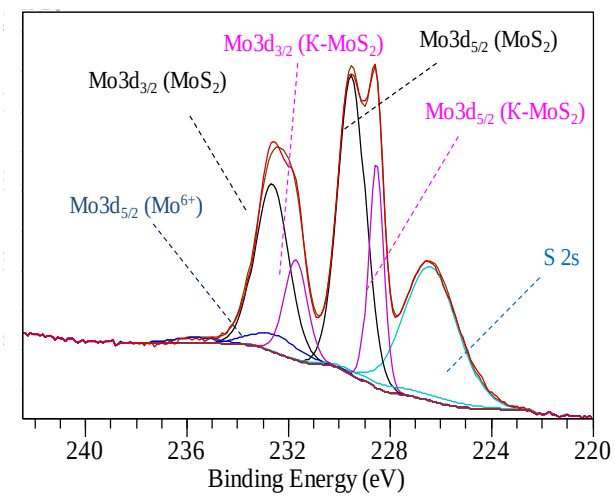
Mo3d3/2 (K-MoS2)
Mo3d5/2 (MoS2)
Mo3d3/2 (MoS2)
Mo3d5/2 (K-MoS2)
Mo3d5/2 (Mo6+)
S 2s
240
236
232
228
224
220
Binding Energy (eV)

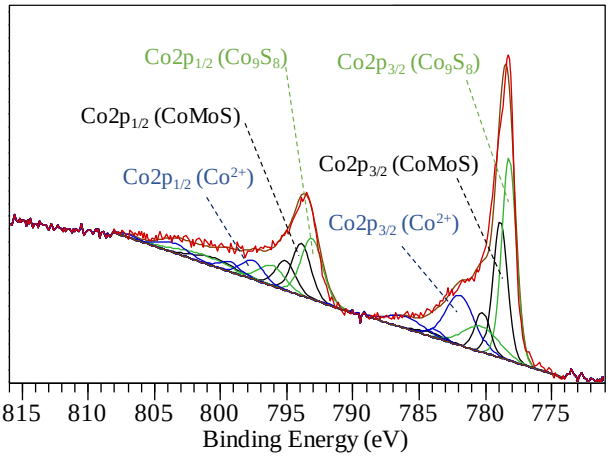
Co2p1/2 (Co9S8)
Co2p3/2 (Co9S8)
Co2p1/2 (CoMoS)
Co2p1/2 (Co2+)
Co2p3/2 (CoMoS)
Co2p3/2 (Co2+)
815
810
805
800
795
790
785
780
775
Binding Energy (eV)

d)

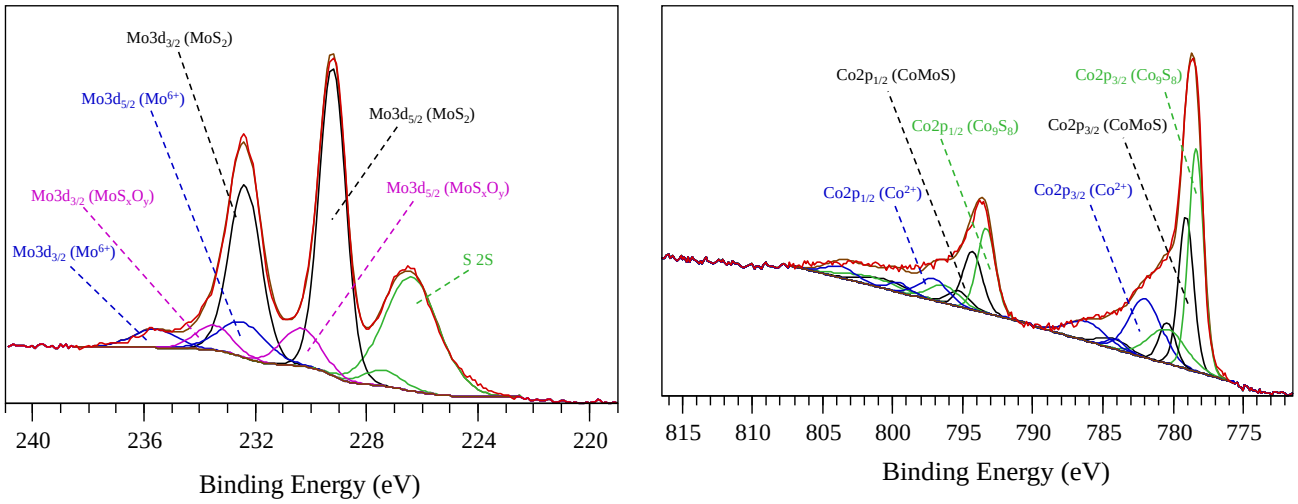

Figure 3.19. XPS Co 2p and Mo 3d spectra recorded for sulfided catalysts; **a**) K-$CoMoS_2/Al_2O_3$; **b**) K-$CoMoS_2$/CCA; **c**) K-$CoMoS_2$/AG-3; **d**) K-$CoMoS_2$/BAW, for Co 2p spectra in blue: Co^{2+} oxide contributions; in green: Co_9S_8 contributions; in grey: CoMoS phase contributions; for Mo 3d spectra in blue: Mo^{6+} oxide contributions; in pink: MoS_xO_y contributions; in grey: MoS_2 contributions

3.3.4 Catalytic Test Studies Over K-$CoMoS_2$/Sup (Sup = Al_2O_3, CCA, AG-3 and BAW)

Figure 3.20 illustrates ethanol conversion over K-$CoMoS_2$ catalysts on alumina and carbon-based supports in He or H_2 atmospheres. Across all catalysts, ethanol conversion under He was greater than under H_2 conditions. Notably, the catalysts remained stable under He atm for two to three weeks longer than they did under H_2, where we observed a little drop-in activity that may be attributable to the rapid desulfurization of the catalysts' surface caused by H_2. The H_2 atmosphere may have hindered ethanol disproportionation and shifted the equilibrium of the reaction toward the reduction and generation of hydrocarbons, resulting in a decreased conversion rate.

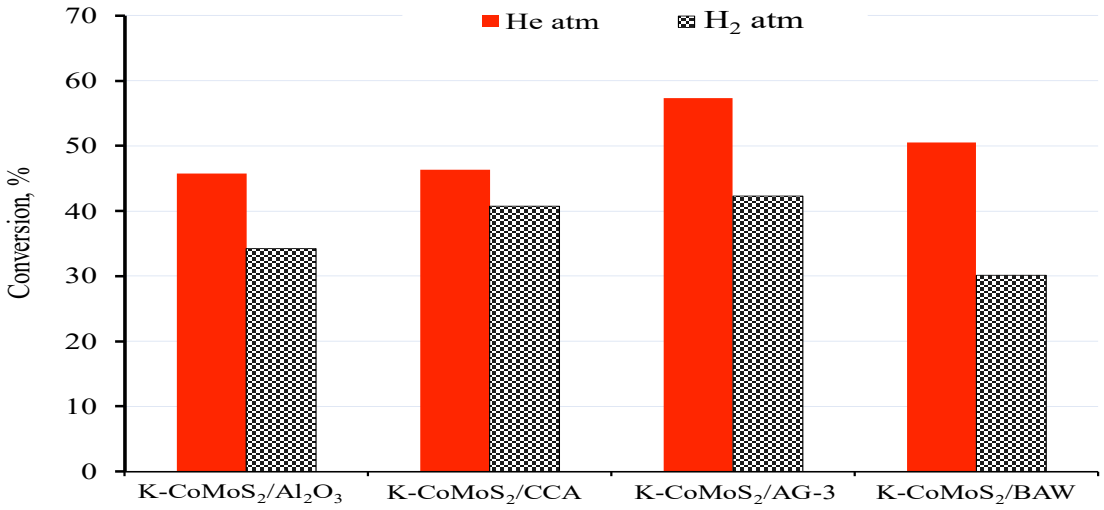

Figure 3.20. Ethanol conversion over the K-$CoMoS_2$/support catalyst under He and H_2. (Conditions: GHSV= 760 $L \cdot h^{-1} \cdot (kg_{cat})^{-1}$; catalyst loading 3 g; feed volume 30 ml ethanol; space velocity, 0.3 ml/min; T = 320ºC; P = 2.5 MPa).

Table 3.9 depicts the composition of the products of ethanol conversion as acetaldehyde, ethyl acetate, butyl acetate, propanol, propanol-2, butanol-1, CO_2, methane, and other short-chain hydrocarbons. Numerous metal oxides, including Al_2O_3, are known to accelerate the ketonization of carboxylic acids and esters. Acetone is produced by ketonization of EtOAc. On K-$CoMoS_2/Al_2O_3$, the production of acetone is consequently greatest. **Table 3.9a** demonstrates that the concentration of liquid oxygenates produced under He was much greater than under H_2 (seen in **Table 3.9b)**. This discovery may be attributed to the distinct conversion behavior of ethanol in these gases. In the first instance, the interaction between alcohol and the hydrogen environment led to the creation of a considerable quantity of saturated gaseous hydrocarbons. In the He atmosphere, it is plausible that ethanol underwent disproportionation, followed by the synthesis of a greater number of different oxygenates and a lower yield of hydrocarbons than in the H_2 atmosphere.

Activated carbon supports minimize the contact between the active phase and the support material in comparison to alumina supports [168–170]. In comparison to the catalysts supported on Al_2O_3 and CCA, the K-$CoMoS_2$ catalysts based on AC

demonstrated improved product distributions of C_{3+} and other oxygenates while yielding less hydrocarbons.

Table 3.9a. Product yield over K-$CoMoS_2$/Sup (Sup = Al_2O_3, CCA, BAW, AG-3) under He atmosphere

	K-$CoMoS_2$/Al_2O_3	**K-$CoMoS_2$/CCA**	**K-$CoMoS_2$/AG-3**	**K-$CoMoS_2$/BAW**
AcH	10.90	6.40	5.30	5.70
DEE	0.00	0.00	0.00	0.20
Acetone	2.10	0.80	0.70	0.70
EtOAc	12.50	17.00	21.10	23.00
PrOH-2	0.10	0.00	0.00	0.00
PrOH-1	2.60	2.80	2.90	2.70
BuOH-1	2.60	1.60	2.60	2.60
BuAOc	0.40	0.10	0.60	0.40
EAA	3.20	2.00	3.00	2.50
CH_4	4.50	3.00	2.50	2.70
CO	0.30	0.00	0.00	0.00
CO_2	4.60	5.80	7.70	5.40
C_2H_4	1.90	3.30	4.20	2.10
C_2H_6	2.10	3.20	4.70	2.20
C_3H_8	0.50	1.70	1.80	1.70
C_4H_8	1.10	1.50	2.40	1.50
C_4H_{10}	1.60	0.00	1.30	0.30

In hydrogenation processes, Al_2O_3- and CCA-supported catalysts are more favorable than AC-supported catalysts. K-$CoMoS_2$/BAW has the highest liquid product conversion rate, followed by K-$CoMoS_2$/AG-3. Due to the acidity of Al_2O_3, the catalyst interacts more strongly with the active phase, resulting in a reduction in the layer growth and stacking number of MoS_2 crystallites [171,172]. Furthermore, [173] indicates that the interaction of the CoMoS phase with Al_2O_3 generates Al—O—Mo links, which are known to inhibit the catalytic activity of the active phase. This results in a reduction in the production of active sites necessary for catalytic activity. In addition, carbon supports

restrict such interactions, resulting in a more flexible active phase that enables the formation of additional vacancies on the edges of MoS_2 slabs. The capacity of multilayer MoS_2 crystallites to create vacancies, which is greater than that of monolayer MoS_2 crystallites, accounts for the higher product yields observed for multilayer MoS_2 crystallites.

Table 3.9b. Product yield over K-$CoMoS_2$/Sup (Sup = Al_2O_3, CCA, BAW, AG-3) under H_2 atmosphere

	K-$CoMoS_2$/Al_2O_3	**K-$CoMoS_2$/CCA**	**K-$CoMoS_2$/AG-3**	**K-$CoMoS_2$/BAW**
AcH	7.40	5.00	3.90	4.70
DEE	0.00	0.00	0.00	0.40
Acetone	1.10	0.50	0.30	0.40
EtOAc	12.30	15.30	12.70	13.00
PrOH-2	0.10	0.00	0.00	0.10
PrOH-1	2.00	1.30	1.60	0.90
BuOH-1	2.70	1.90	2.30	3.00
BuAOc	0.30	0.20	0.30	0.30
EAA	1.90	1.30	1.00	1.00
CH_4	2.30	0.20	1.40	1.40
CO	0.20	0.00	0.00	0.00
CO_2	2.70	4.00	3.80	1.30
C_2H_4	1.90	6.40	3.00	0.80
C_2H_6	1.70	5.90	4.20	0.80
C_3H_8	0.50	0.60	2.70	1.30
C_4H_8	0.30	0.00	2.70	1.20
C_4H_{10}	0.00	0.00	3.70	1.10

3.3.5 Influence of catalyst textural properties

Figure 3.21 depicts the correlation between product yields and specific surface area (S_{micro} and S_{meso}) of the evaluated catalytic samples. Various SSA may be shown to effect product yields. S_{micro} decreased in the following order: K-$CoMoS_2$/BAW > K-$CoMoS_2$/AG-3 > K-$CoMoS_2$/CCA > K-$CoMoS_2$/Al_2O_3. For mesopores, S_{meso} arose as

follows: K-$CoMoS_2/Al_2O_3$ > K-$CoMoS_2$/CCA > K-$CoMoS_2$/AG-3 > K-$CoMoS_2$/BAW. As the surface area fluctuates, it is anticipated that the crystallite particles on the surface would vary. The bulk of big crystallites are composed of layered structures with a stacking number above one. Moreover, dispersed particles of minuscule size (particularly K-$CoMoS_2/Al_2O_3$ and K-$CoMoS_2$/CCA) are often mono- or bi-layered. A larger specific surface area generates more minute particles than a smaller one. While particles with a higher stacking number are more/less stable, the number of finer particles rises with their surface area. In addition, as the H_2 atmosphere's surface area grows, there is an increase in HC and a decrease in liquid products. **Figure 3.21** illustrates the rise in liquid product output as the surface area increases under He atm. In the hydrogen atm, the production of liquid products reduced as the surface area increased, but the production of hydrocarbon products dropped somewhat in both reaction atmospheres.

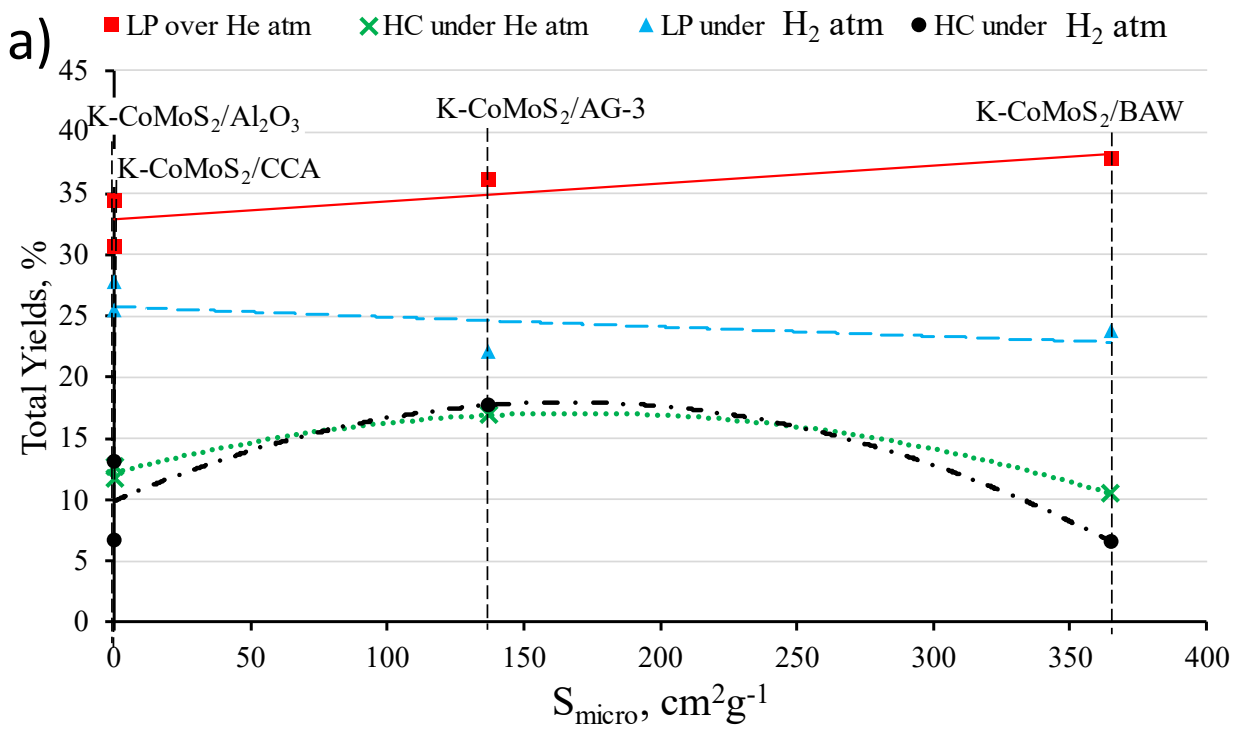

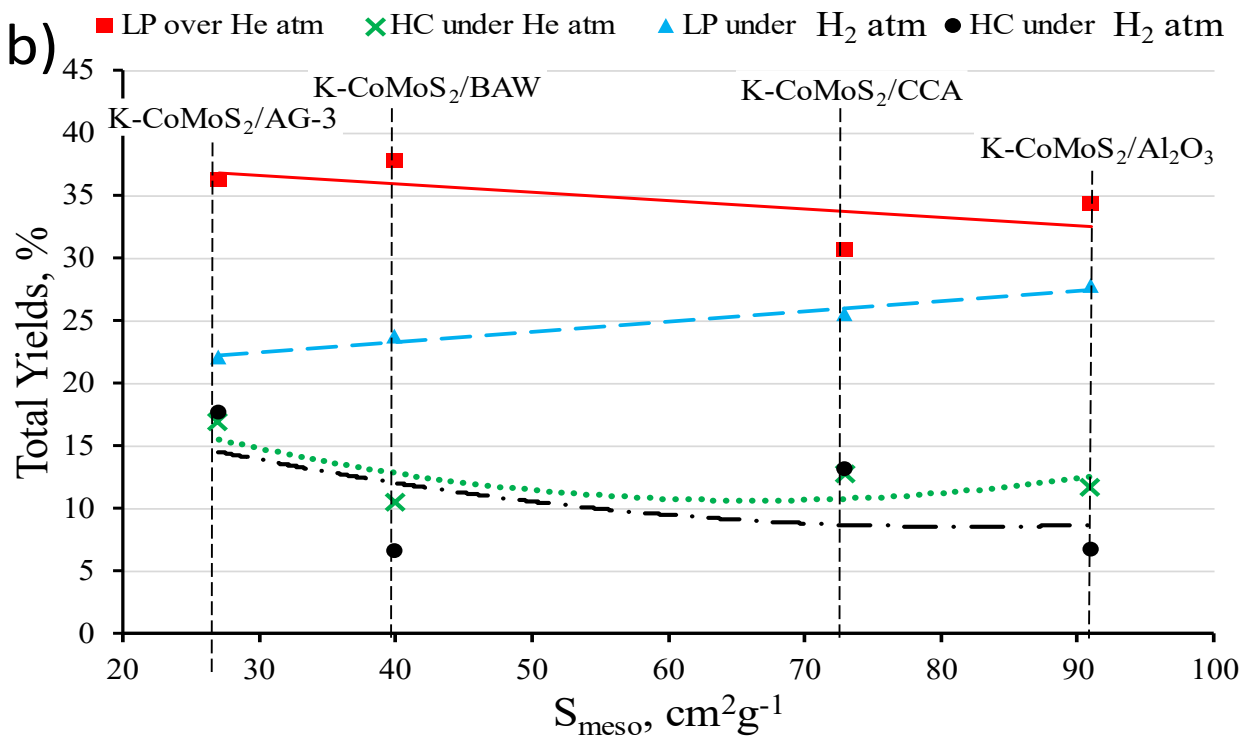

Figure 3.21. Dependence of liquid products and hydrocarbon yields on: (a) S_{micro}; (b) S_{meso}, (LP – liquid products, HC – hydrocatbons).

Figure S3.3 illustrates the relationship between major liquid product yields and overall micro- and mesopore volumes (i.e. V_{micro} and V_{meso}). In all reaction atmospheres and at all pore volumes, the principal result was ethyl acetate (V_{micro} and V_{meso}). As V_{meso} grows, BuOH-1 and acetaldehyde yields (on mesopores, **Figure S3.3c, d**) increase, whereas PrOH-1 yields stay almost constant. This may suggest that the yields of BuOH-1 and acetaldehyde were dependent on the change in pore volume in both reaction atmospheres, and that their yields rose as the pore volume grew. On CCA- and Al_2O_3-based catalysts, these were detected.

Similar correlations were seen between yields of the major liquid product and the total surface area of micro- and mesopores (i.e. S_{micro} and S_{meso}), as shown in **Figure S3.4**. Observations were made between 0 and 400 m^2/g S_{micro} and 20 and 100 m^2/g S_{meso} in both the He and H_2 reaction atmospheres. Ethyl acetate was produced with a high yield regardless of its textural qualities. However, when S_{meso} and S_{micro} increased, the yields of ethyl acetate (**Figure S3.4d**; in the He atmosphere) and acetaldehyde (**Figure S3.4a**; in the H_2 atmosphere) dropped, respectively. The yields of acetaldehyde and acetone

exhibited a small exponential increase between 64 and 90 m^2/g S_{meso} for catalysts based on CCA and Al_2O_3. Using a catalyst with a greater mesoporous surface area, it is fair to assume that these compounds may be produced with high yields.

According to reports [173], the surface of activated carbon is inert compared to that of Al_2O_3, despite the presence of oxygen-containing functional groups on the carbon surface. Consequently, active components of the catalyst and adsorbed species may interact with these groups when disseminated on the surface of the activated carbon support, particularly at elevated temperatures. Carbon surfaces may chemisorb oxygen at low temperatures (e.g., room temperature) to generate oxygen-containing surface complexes with varying thermal stabilities. Several of these clusters are dispersed around the surface and inside the pores. Micropores are most likely obstructed by a large MoS_2 crystallite that covers a significant amount of the microporous surface area. In addition, some of these oxygen surface groups contribute to the intensity and extent of the contact between Mo and the C-surface, with dispersion rising as the number of oxygen surface groups increases. This may explain how some K-$CoMoS_2$ catalysts supported on activated carbon are more active than those supported on alumina.

3.3.6 Effect of Catalyst Acidity of Product Distribution

Using pyridine-adsorption, the total surface acidity of the samples was calculated. **Table 3.10** shows the total acidity of supports and catalysts. The acidity of the supports might be classed as follows, from most acidic to least acidic: Al_2O_3 > CCA > AG-3 > BAW. K-$CoMoS_2/Al_2O_3$ > K-$CoMoS_2$/CCA > K-$CoMoS_2$/AG-3 > K-$CoMoS_2$/BAW, in the same sequence as the acidity of the respective supports. Note that following impregnation with K, Co, and Mo precursors, the acidity of the catalysts supported on CCA, AG-3, and BAW rose. This rise is a result of the sulfidic active phase being more acidic than the carbon supports. The acidity of the Al_2O_3-supported catalyst decreased considerably after the addition of the precursors. After covering the Al_2O_3 surface with amorphous carbon, the acidity of the Al_2O_3 support decreased dramatically, resulting in a

reduction in the number of Lewis acid sites. These sites were inhabited by coke formed on acidic surfaces.

The possible sources of acidity of the active phase are SH groups (Brønsted acidity) and coordinative unsaturated sites (CUS, Lewis acidity) located on MoS_2 slabs. SH groups normally are weak acids and pyridine used for probing acidity is a weak base. We assume, that our technique mostly measured amount of Lewis acid sites that are CUS of the active phase.

Table 3.10. Comparison of total acidity of $KCoMoS_2$ catalysts supported on alumina-based and granular activated carbons materials.

Samples	Total acidity, μmol/g [a]
Al_2O_3	285.77
K-CoMoS/Al_2O_3	43.90
CCA	3.57
K-CoMoS/CCA	11.74
AG-3	3.62
K-CoMoS/AG-3	9.35
BAW	0.28
K-CoMoS/BAW	7.17

[a] Surface acidity was determined by pyridine-adsorption-TPD

Figure. S3.5 shows the dependence of liquid product yields on catalyst surface acidity. The dependence under He and H_2 is shown in **Figure. S3.5a** and **b**, respectively. It is worth mentioning that there was no clear relationship between total ethanol conversion and catalyst surface acidity, but a clearer relationship was marked concerning the distribution of main products. The formation of ethyl acetate decreased with the increase of catalyst surface acidity under He, whereas an opposite trend was noted for the formation of the primary product of ethanol and acetaldehyde dehydrogenation. However, products such as butanol-1, propanol-1 and ethyl acetoacetate were synthesized almost in the same amounts across all the catalysts with surface acidity. Of note is that there was a slight decrease in the acetone yield with the decrease in surface acidity under these

reaction conditions. **Fig. S3.5b** illustrates product distribution in the reaction in the H_2 atmosphere. The formation of ethyl acetate did not increase with the increase in surface acidity, as observed under He. It may be because the reaction with ethanol proceeds differently in both reaction atmospheres. A slight decrease in the acetaldehyde yield with a decrease in surface acidity was observed. These findings further suggest that for these systems for ethanol reaction the He atm is more suitable than the H_2 atm. The dependence of the product yield on surface acidity indicates that dehydrogenation of ethanol (i.e. direct synthesis of AcH) requires Lewis acid sites. The more acidic material gave higher yields of acetone and acetaldehyde, and the more basic material yielded more ethyl acetate and slightly increased the HA formation. The surface-active sites for the ethyl acetate formation in these catalysts are assumingly the same as those for ethanol dehydrogenation.

Figure 3.22 depicts TOF dependences on (a) the stacking number and length of the crystallites; (b) the number of the active sites and catalyst acidity; (c) the number of the sites and ratio of the length to the stacking number. As it follows from the plots, the TOF dependences on the cited parameters consist of two segments (K-$CoMoS_2/Al_2O_3$ —– K-$CoMoS_2$/CCA (projection 1——2) and K-$CoMoS_2$/AG-3 —— K-$CoMoS_2$/BAW (projection 3——4)), which are positioned in different planes and their projections cannot merge. It indirectly indicates that active sites of the alumina-supported catalysts (K-$CoMoS_2/Al_2O_3$ —— K-$CoMoS_2$/CCA) differ in nature from those of the activated carbon-supported catalysts (K-$CoMoS_2$/AG-3 —— K-$CoMoS_2$/BAW). Comparison of the projections of lines 1——2 and 3——4 in the bottom plot, **Figure 3.22a,** shows that the TOF increase for the alumina-supported catalysts is mainly determined by the increase in the stacking number of the crystallite compared to the activated carbon-supported catalysts. For K-$CoMoS_2$/AG-3 —— K-$CoMoS_2$/BAW, the TOF value depends chiefly on the crystallite length. This difference can be a result of different locations of the active sites. Active sites of the alumina-based catalysts may be located on the rims and active sites of the activated carbon-based catalysts on the crystallite edges. The plot in **Figure 3.22b** also witnesses in favour of this assumption. Comparison of the projections of

segments 1——2 and 3——4 on the bottom plane shows that TOF over the alumina-based supported catalysts is suppressed by acidity, whereas TOF over the active carbon-supported catalyst is unaffected by negative acidity. At the same time, for K-$CoMoS_2$/AG-3 —— K-$CoMoS_2$/BAW, simultaneous growth of TOF is determined by the reduction in the number of active sites per crystallite length (specific active sites number, SASN). This unusual relationship can be explained by drawing on the data in **Figure 3.22c**.

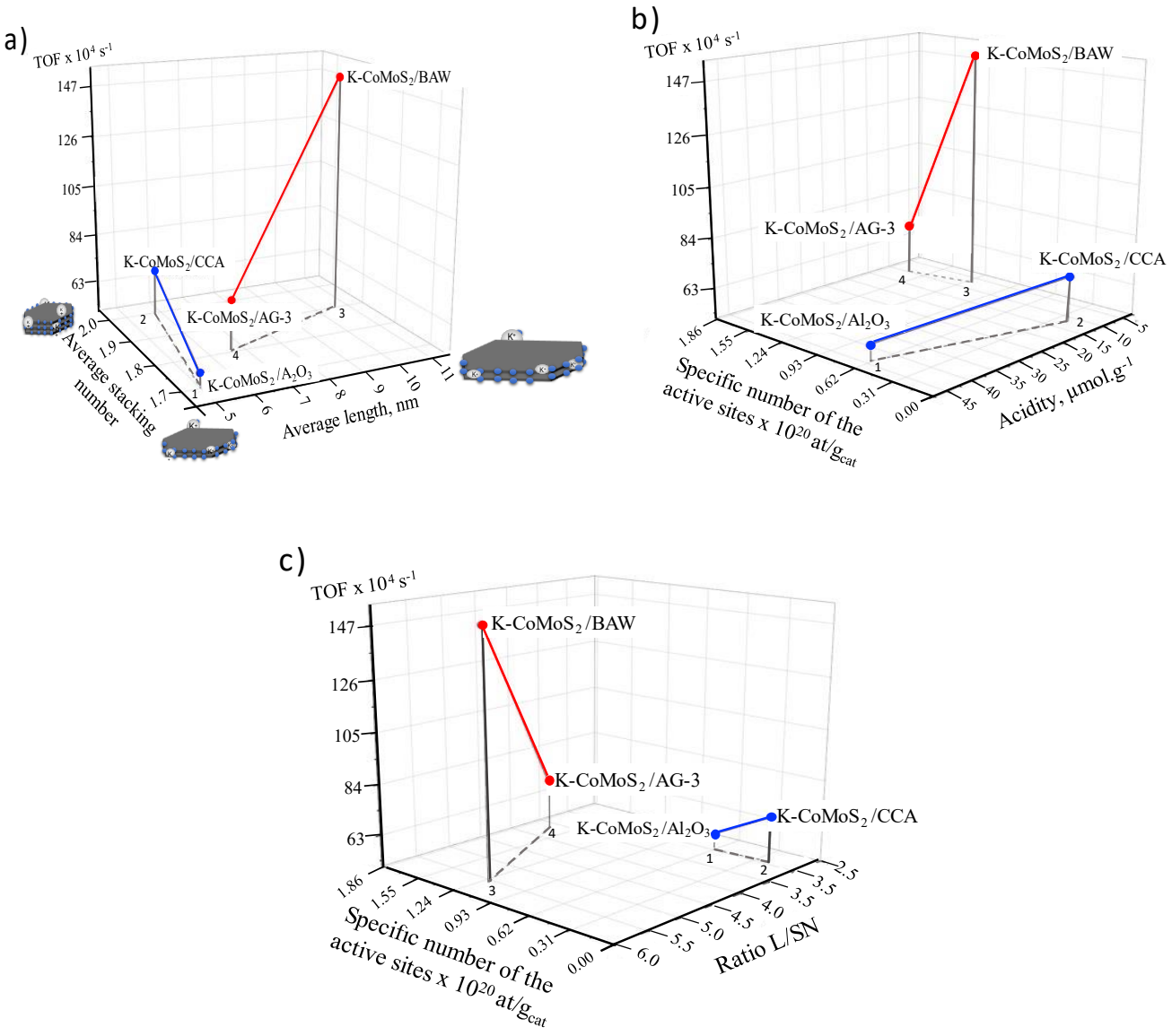

Figure 3.22. 3D plots of TOF vs (a) stacking number and length of the crystallites; (b) active site number and catalyst acidity; (c) active site number and ratio of the length to the stacking number

As seen from **Figure 3.22c**, the decrease of SANS is followed by the increase in the ratio of the length to the stacking number (L/SN), i.e., crystallite widening for the activated carbon-based catalysts. The decrease in SASN was also noted for the alumina-based catalysts but without changes in the L/SN ratio. It means that, for these catalysts, changes in the crystallite length are proportional to changes in their stacking number. Getting together data of the a, b, c plots, we can conclude that the determining factor for TOF growth on the alumina-based catalysts is the increase in the stacking number and decrease in the acidity of the catalyst (and of the carrier in particular). For activated carbon-supported catalysts, acidity is not a key factor (it is low in comparison with alumina-supported ones); rather the crystal length and possibly the distance between neighboring active sites can determine catalyst activity. Using the "rim-edge" model [19,137], we may assume with a high probability that the sites determining the catalytic activity of alumina-based catalysts are located predominantly on the rims, and the sites of the activated carbon-based catalysts are located on the edges of promoted MoS_2 crystallites.

Carbon on the CCA reduces the interaction between the alumina and the active phase. However, carbon does not uniformly cover the surface of alumina, since organic precursors preferentially adsorb on Lewis sites and block them. The oxidic precursors for the active phase can only adsorb on the remaining carbon-free alumina surface, resulting in sulfide crystallites with a larger stacking number, altering the diameter/height ratio of the crystallites and influencing catalytic activity.

3.3.7 Dependence of Acidity and Morphology on Catalyst Activity

Figure 3.23 illustrates the correlation between the acidity of the catalyst and the number of promoted active sites. Catalysts supported by carbon have more active sites (Co in a form of CoMoS phase) than those based on alumina. This helps explain why carbon-based catalysts are more active than alumina-supported catalysts. Furthermore, it should be highlighted that the promoted sites on AG-3-supported catalysts are more active than those on BAW-supported catalysts, despite the fact that the BAW-supported catalyst

is more active. **Figure 3.16** demonstrated that BAW has a multimodal distribution, and the BAW-supported catalyst is more active in terms of total product yields than AG-3, despite K-$CoMoS_2$/AG-3 having more active sites. Due of the multimodal pore distribution in BAW, intermediates of varying sizes are able to reach some of the active sites inside the pores.

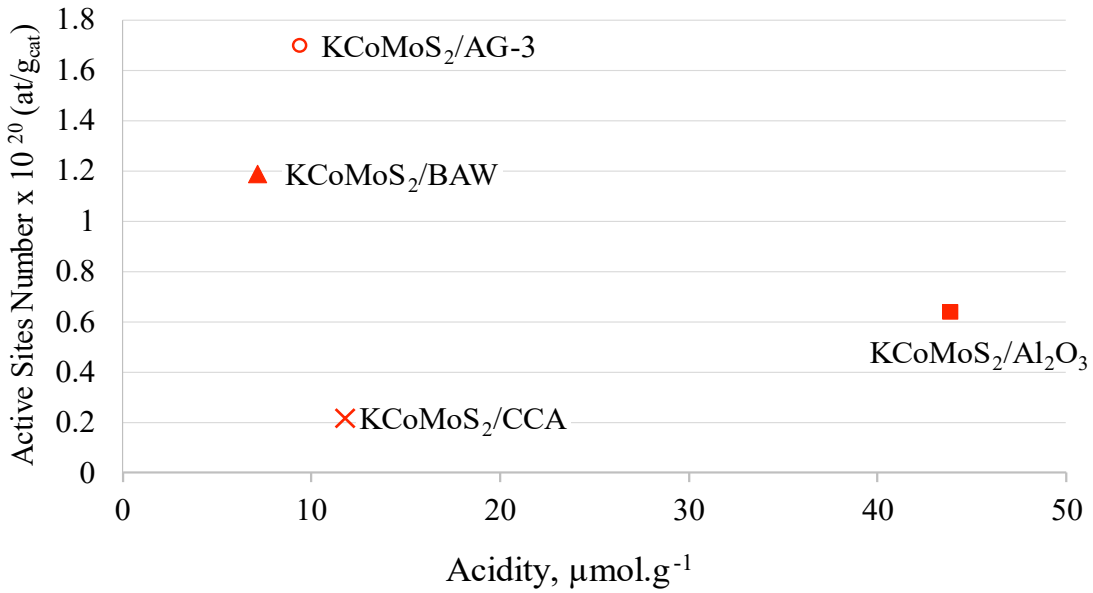

Figure 3.23. Number of promoted active sites vs catalyst acidity of K-$CoMoS_2$/Sup catalysts (Sup = Al_2O_3, CCA, BAW, AG-3).

Figure 3.24 shows the dependence of TOF number in ethanol conversion on the active phase dispersion. TOF decreased with increasing dispersity of the active phase. The carbon-supported catalysts had a greater TOF and lower dispersity than the alumina-based catalysts. As a result, the catalyst's efficiency improved. The reduction in dispersion of CoMoS active phases was favorable, since catalysts with reduced dispersion were more active than those with larger dispersion. Consequently, it is reasonable to suppose that the decrease in dispersity of CoMoS active phases hastened the formation of more active Type II multilayers of CoMoS active phase. As a consequence of decreased contact between the active phase and the support, the Type II CoMoS phase is more active in catalysts than the Type I CoMoS phase [27,170]. This phenomena may be explained by a "rim-edge" hypothesis [173], according to which HDS sites are mostly placed on the CoMoS slab

edges and HYD sites on the slab rims. The slab edges include HDS-producing sites, while the rims comprise both HYD- and HDS-producing sites. The majority of HYD is caused by sites located at spatial angles (edge points and rim crossings). The height/diameter ratio of crystallites may affect the HYD/HDS site ratio, hence enhancing the activity of the catalyst. While the rim-edge model was first developed for unpromoted catalysts, it is now able to explain experimentally observed correlations between active phase geometry and catalytic activity for modified and promoted bulk and supported $CoMoS_2$-based catalysts [156,174]. In **Figures 3.22** (a, b, c), the dependency of TOF on the number of active sites, stacking number, and average crystallite length is shown. Based on the Figures, acidity is not a crucial component for activated carbon-supported catalysts (it is low compared to alumina-supported catalysts); crystal length and maybe the distance between neighboring active sites can impact catalytic activity. Also, it should be highlighted that the intercalated K-MoS_2 phase observed by XPS (**Figure 3.19**) in the K-$CoMoS_2$/AG-3 sample had no effect on the catalytic activity. Using the rim-edge model [19,137], we can assume with a high degree of confidence that the sites determining the catalytic activity of alumina-based catalysts are primarily located on the rims, whereas the sites of activated carbon-based catalysts are located on the edges of promoted MoS_2 crystallites.

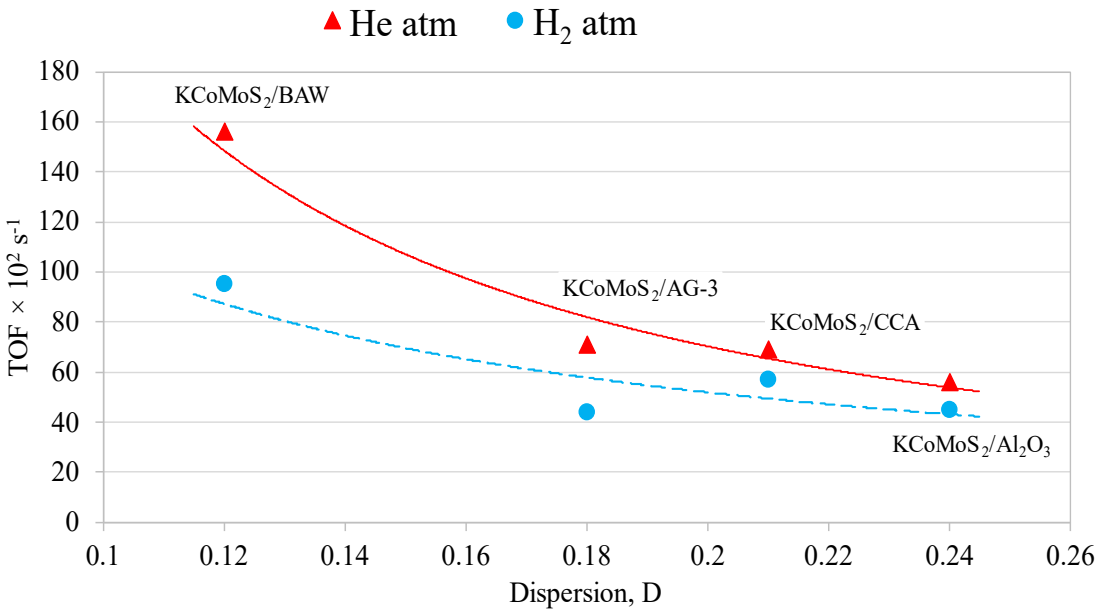

Figure 3.24. Dependence of the catalysts' TOF number in ethanol conversion on the active phase dispersion.

a)

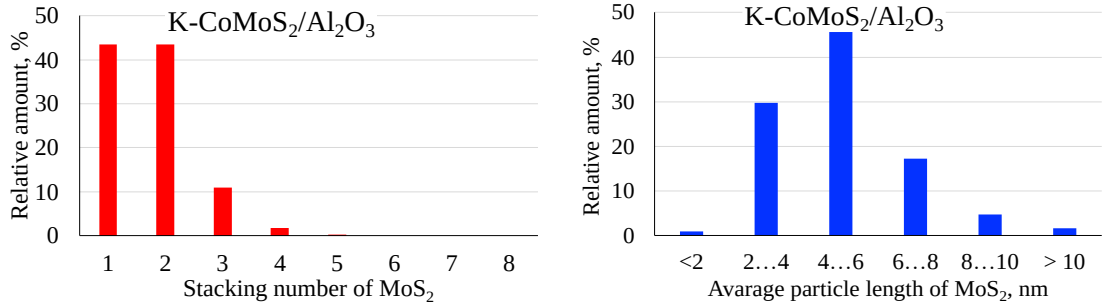

b)

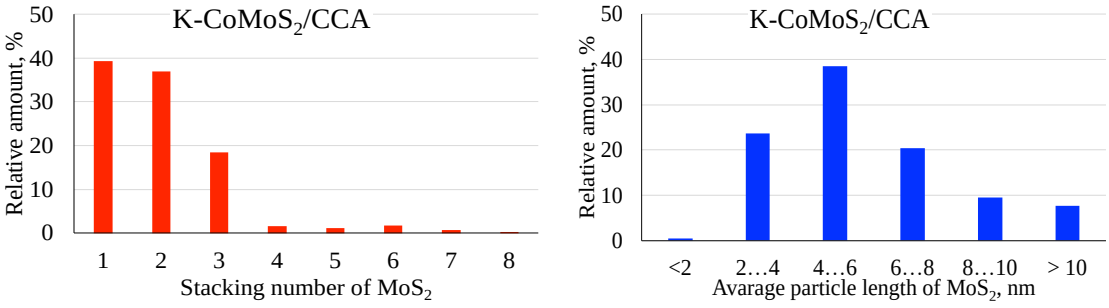

c)

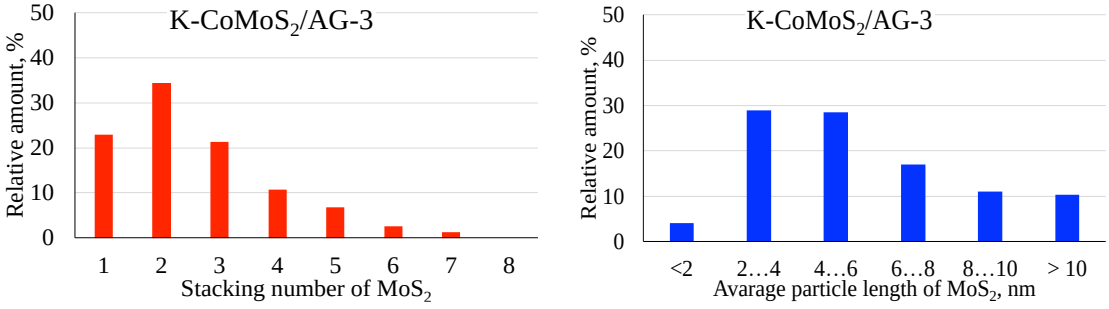

d)

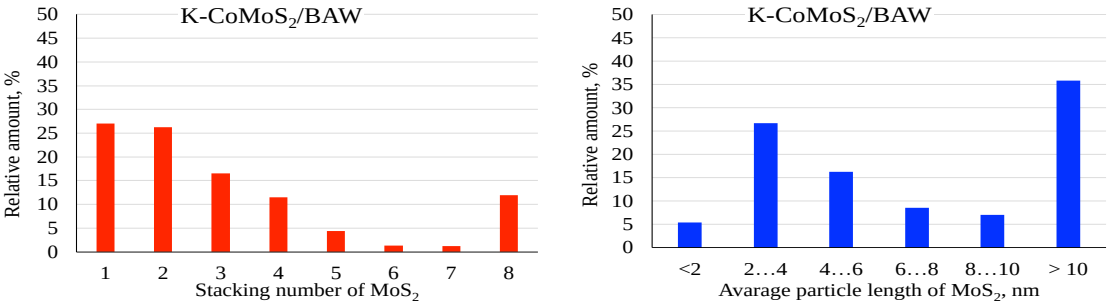

Figure 3.25. Slab length distribution and Slab degree of stacking distribution obtained from minimum 500 individual slabs per sample as recorded from TEM image; a) K-$CoMoS_2/Al_2O_3$; b) K-$CoMoS_2$/CCA; c) K-$CoMoS_2$/AG-3; d) K-$CoMoS_2$/BAW

Figure 3.25 illustrates that the kind of support had a substantial influence on the distribution of the active phase, which had a direct effect on the catalytic properties and performance. With an increase in the average length of crystallites (> 10) above K-$CoMoS_2$/BAW, a stacking number of around 8 layers was discovered. The same was seen with K-$CoMoS_2$/AG-3 as opposed to Al_2O_3-based catalysts. The formers were characterized by longer crystallites with a lower stacking degree. These results provide conclusive evidence that the catalyst support had a role in the total liquid yields seen in **Table 3.8**; total liquid yields increased as follows: K-$CoMoS_2$/Al_2O_3 < K-$CoMoS_2$/CCA < K-$CoMoS_2$/AG-3 < K-$CoMoS_2$/BAW.

3.5 The proposed scheme of ethanol conversion reactions on catalysts based on K-(Me)MoS_2 is shown in Figure 3.26.

The suggested reaction network for ethanol conversion is shown in **Figure 3.26**. Ethanol (a) was converted through primary dehydrogenation (branch 1) to an aldehyde-like adsorbed intermediate (b), existing in equilibrium with acetaldehyde in the gas phase. The adsorbed intermediate reacts further via three major branches: the hydrodeoxygenation branch (2), condensation branch (3), and secondary dehydrogenation branch (4). The main liquid product on all catalysts was ethyl acetate (p, secondary dehydrogenation branch). Other notable products were C_2-hydrocarbons (j, k; hydrodeoxygenation branch), ethyl acetoacetate (q, Claisen condensation subbranch), butanol (f, condensation branch), methane (fragmentation subbranch 4i), and acetaldehyde, the yields of which were dependent on catalyst composition. Despite the synthesis of ethyl acetate, no diethyl ester, diethoxy ethane, or acetic acid has been observed. CO was most likely produced by decarbonylation (fragmentation subbranch 4i), whereas CO_2 was obtained via water-gas-shift.

According to DFT calculations, hydrogenolysis of the C-O bond in the aldehyde-like intermediate proceeds with a lower activation energy than direct hydrogenolysis of ethanol [44,100]. This is corroborated by our finding that, in some experiments, ethanol hydrogenolysis was inhibited under increased hydrogen pressure during ethanol

conversion [83]. The hydrodeoxygenation branch starts with the production of an ethyl surface intermediate. Its primary products are hydrocarbons. The branch is especially prominent on $FeMoS_2$ and $NiMoS_2$ catalysts, where C_2-hydrocarbons are the primary products. Potassium strongly inhibits this branch. Potassium instead promotes the chain growth subbranch (2i), which produces propanol-1.

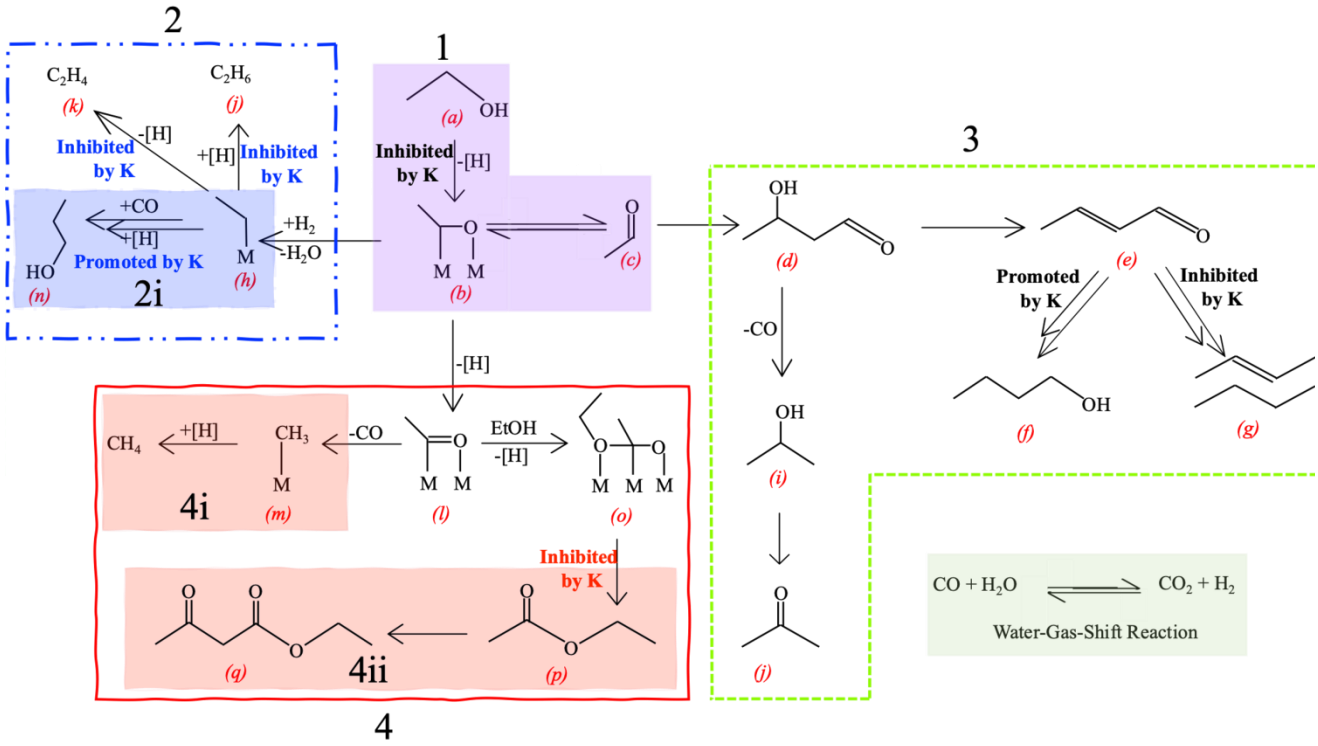

Figure 3.26. Reaction network of ethanol conversion over the K-(Me)MoS_2 supported catalysts (1 – Primary dehydrogenation; 2 – Primary dehydration; 2i – Chain growth branch; 3 – Aldol branch; 4 – Secondary dehydrogenation;4i – Fragmentation; 4ii – Claisen condensation)

Excess potassium modifier (alkali) was employed in catalyst synthesis. The ratio of K/Mo was 2. Only a minor amount of K participated in the formation of the K-sulfide phase. We assume that the remaining K binds to the acidic sites of the support and/or participates in the formation of sites with a basic character, for example, deposited on the surface of MoS_2 as K_2CO_3. This permitted the formation of ethyl acetoacetate (q) as a result of the Claisen condensation subbranch (4ii) catalyzed by the basic catalyst function. The synthesis of a significant number of C_4-products is most likely due to the aldol

condensation of acetaldehyde (condensation branch 3), which is also catalyzed by bases. Decarbonylation of the intermediate aldol would result in the synthesis of isopropanol (i) and acetone (j). Acetone may also be formed by the ketonization of carboxylic acid derivatives, specifically ethyl acetoacetate.

3.6 Perspectives of Using the Oxygenates from Ethanol Conversion

The resulting mixture of oxygenates contains mostly ethyl acetate and derivatives of higher alcohols, **Table 3.11**, which are widely used as high-performance solvents in the paint industry, as well as valuable high-octane motor gasoline components with good miscibility with traditional gasoline components and a reduced carbon footprint.

Table 3.11. Content of liquid oxygenates obtained over K-$CoMoS_2$/AG-3 and K-$CoMoS_2$/BAW catalysts and their characteristics

Compound	Content (% wt.)	Boiling temperature (^oC)	Density at 20 ^oC (kg/m^3)	Octane number
AcH	14.6-15.1	20	784	n.d.
EtAOc	58.3-60.8	77	902	122
EAA	6.6-8.3	180	1028	n.d.
BuAOc	1.1-1.7	126	881	96
Acetone	1.9	56	790	110
BuOH-1	6.9-8.0	117	810	100
PrOH-1	7.1-8.0	97	800	103

It is well known that bio-alcohols such as ethanol and butanol can reduce the life-cycle greenhouse emissions, due to their biological production processes. The main advantage of alcohol- based fuels is the reduction of CO and HC emissions when used in spark-ignition engines as a gasoline substitute [175][176][177]. The substitution of ethanol (up to 10% by volume) by n-butanol (up to 16% by presents a series of benefits such as a higher heating value or a lower hygroscopic tendency compared to ethanol

blends, which makes n-butanol a promising fuel for spark ignition engines [178][179]. The higher heating value for butanol–gasoline blends would reduce the engine fuel consumption. When butanol is blended with gasoline, the vapor pressure decreases, and consequently, the blends fulfil EN 228. Recently it was found [180][181] that in terms of thermal efficiency, combustion characteristics and emission behavior the blends of acetone-butanol–ethanol have might be much better suited for use as an alternative fuel in spark-ignition engines, relative to n-butanol.

Earlier [181] it was found that the addition of ethyl acetate to ethanol-gasoline blends creates lots of advantages including: increasing in water tolerance, prevention of phase separation, increasing octane rating, decreasing vapor pressure and vapor lock index values. Ethyl acetate causes increase in the area formed due to azeotrope formation but approximately do not affect 50 % vol. of evaporated temperature. These advantages encourage the use of ethyl acetate as a potential ethanol-gasoline stabilizer or as extender. Since the ethanol conversion products contain reactive acetaldehyde and acetone, in order to improve their properties as a direct component of gasoline, it seems to be advantageous to react with alcohols to form high-octane acetals/ketals. Thus, the resulting oxygenates and their derivatives can have a mixing octane number higher than 113.

Conclusions

1. K-modified and promoted MoS_2 catalysts were synthesized and investigated using commercial mesoporous Al_2O_3, carbon-coated Al_2O_3 (CCA), new fibrous and microporous activated carbons as supports.

2. K incorporation into the composition of the catalyst (Me)MoS_2 resulted in the conversion of ethanol to improved selectivity for alcohols C_{3+} and other oxygenates, an increase in the ratio of liquid to gaseous products, and inhibition of ethanol dehydration into ethylene and intermolecular dehydration into diethyl ether

3. The carbon-supported catalysts were characterized by a higher TOF number and a lower dispersion of K-$CoMoS_2$ particles than catalysts on Al_2O_3 and CCA. A decrease in the dispersion of the active phases of K-$CoMoS_2$ had a positive effect on the

conversion of ethanol into oxygenates (catalysts with lower dispersion were more active than catalysts with higher dispersion, and carbon-based catalysts were more active than Al_2O_3-based catalysts).

4. Catalysts deposited on granular activated carbon had an active phase consisting of multilayer crystallites that promote the formation of oxygenates, and carbon fiber-based catalysts had active phases with fewer stacked layers that promote the formation of hydrocarbons.

5. The probability of dehydration and dehydrogenation reactions increased with an increase in the acidic properties of the catalyst, and for aldol-type condensation reactions it decreased. This fact is due to the formation of larger agglomerates consisting of hundreds and thousands of clusters of molybdenum sulfide on support with low acidity, as well as the formation of highly dispersed single clusters inside mesopores on surfaces with high acidity.

6. Sulfides K-(Me)MoS_2 deposited on granular activated carbons with high microporosity are effective catalysts for ethanol dehydrogenation and can be recommended for practical use for the synthesis of ethyl acetate, acetaldehyde and C_{3+} alcohols.

Recommendations

In this work, an effort was made to construct a Co (Ni, Fe)-promoted K-modified MoS_2 catalyst based on activated carbon materials that is extremely efficient. The study shed light on the catalyst composition required for optimal performance during the synthesis of oxygenates from ethanol. The novel catalysts demonstrated ethanol reaction activity. Despite this, the following recommendations might be made to give direction for future study in this field:

- It is widely known that catalytic activity and product selectivities are dependent on the technique of catalyst synthesis and the metal precursors used in catalyst composition. This study focused only on sequential pore volume impregnation. Future research can examine the effect of preparation techniques such as the sol gel

technique and micro- emulsion techniques, as well as the incorporation of additives such as chelating agents ethylenediamine tetraacetic acid (EDTA), nitrilotriacetic acid (NTA), etc., on the catalytic performance of activated carbon supported MoS_2-based catalysts for ethanol conversion.

- Deposition of carbon on the surface of the catalyst may lead to its deactivation. Although a long-term assessment of the AC-supported K-$CoMoS_2$ catalyst's stability was undertaken to determine the catalyst's tendency for deactivation, the quantity of carbon deposits was not quantified in this study. To determine the extent of coking the catalyst has endured as a consequence of time-on-stream, it will be interesting to assess both the fresh and spent catalysts.

Nomenclature and Abbreviations

BuOH-1	Butanol-1
CCA	Carbon Coated Alumina
CUS	Coordinative unsaturated sites
DEE	Diethyl ether
EAA	Ethyl acetoacetate
EDX	Energy Dispersive X-ray
EtAOc	Ethyl acetate
EtOH	Ethanol
HC	Hydrocarbon
HDN	Hydrodenitrogenation
HDO	Hydrodeoxygenation
HDS	Hydrodesulfurization
HYD	Hydrogenation
NSA	Normalized surface area
PrOH-1	Propanol-1
RVP	Reid Vapor Pressure

SEM	Scanning Electron Microscopy
TMS	Transition metal sulfides
TOF	Turnover Frequency
WGS	Water-gas-shift
XPS	X-ray photoelectron spectroscopy
XRF	X-ray fluorescence

Research Outcome

The main content of the dissertation is presented in the following works:

1. **Tshepo D. Dipheko**, Vladimir V. Maximov, Mohamed E. Osman, Oleg L. Eliseev, Alexander G. Cherednichenko, Tatiana F. Sheshko and Victor M. Kogan. Synthesis of Oxygenated Hydrocarbons from Ethanol over Sulfided KCoMo-based Catalysts: Influence of Novel Fiber and Powder Activated Carbon Supports // Catalysts. – 2022. – V. 12. – P. 1497. (Scopus and Web of Science Q2)
2. **Tshepo D. Dipheko**, Vladimir V. Maximov, Evgeny A. Permyakov, Mohamed Ezeldin Osman, Alexander G. Cherednichenko, Victor. M. Kogan., Ethanol Dehydrogenation over (K)(Co)MoS_2-Catalysts Supported on Activated Carbon: Effect of Active Phase Composition // South African Journal of Chemical Engineering. – 2022. – V. 42. – P. 290 – 305. (Scopus Q1)
3. **Tshepo D. Dipheko**, Vladimir V. Maximov, Mohamed E. Osman, Evgeny A. Permyakov, Alexander V. Mozhaev, Pavel A. Nikulshin, Alexander G. Cherednichenko, Victor M. Kogan. Catalytic Conversion of Ethanol Over Supported $KCoMoS_2$ Catalysts for Synthesis of Oxygenated Hydrocarbons // Fuel. – 2022. – V. 330. – P. 125512. (Scopus and Web of Science Q1)
4. **Dipheko T.D.,** Maximov V.V., Permyakov E.A., Cherednichenko A.G., Kogan V. M. Influence of the composition of the active phase and carrier materials on (K)(Co)MoS_2 catalysts for the conversion of ethanol into various oxygenates // Advances in Chemistry and Chemical technology. – 2022. - V. 36. – №. 13(262). – P. 181 – 182. (RISC)
5. **Tshepo D. Dipheko**, Oleg L. Eliseev, Yurii A.Agafonov, Maria V. Tsapkina, Vladimir V. Maximov, Mohamed E. Osman, Alexander G. Cherednichenko,

Victor M. Kogan. Promotion of cobalt catalyst for Fischer–Tropsch synthesis by molybdenum as protection against sulfur poisoning // Mendeleev Communications – 2021. – V. 31(6). – P. 872 – 874. (Scopus and Web of Science Q3)

Abstracts and materials presented at international conferences:

6. **T.D. Dipheko**.; V.V. Maximov.; E.A. Permyakov.; A.G. Cherednichenko.; V.M. Kogan. Effect of Supports on MoS_2-based Catalysts for Ethanol Conversion to Long-chain Alcohols and Other Oxygenates // International scientific conference "Catalysis for a Sustainable World", RUDN, Moscow, Russia. RUDN, Moscow, Russia. 15-18 December **2020.** Pg. 22-24./соавторов из РУДН 3.

7. Kogan V.M., Osman M.E., **Dipheko T.D**., Maximov V.V., Dorokhov V.S., Permyakov E.A., Sheshko T.F., Cherednichenko A.G. Alkali-modified transition matel sulfide catalysts supported on carbon materials for syngas conversion into higher alcohols and other oxygenates: Mechanistic aspects // Catalysis for a Sustainable World Conference, RUDN University, 2020, 35-37.

8. **Tshepo D. Dipheko**, Vladimir V. Maximov, Mohamed E. Osman, Evgeny A. Permyakov, Alexander G. Cherednichenko, Victor M. Kogan. Ethanol Dehydrogenation over Carbon Supported (K)(Co, Ni, Fe)MoS_2-based Catalysts // 10th Edition of Global Conference on Catalysis, Chemical Engineering & Technology, 28 – 30 March **2022**, Chicago, IL 60606, USA.

9. **Tshepo D. Dipheko**, Vladimir V. Maximov, Mohamed E. Osman, Evgeny A. Permyakov, Alexander G. Cherednichenko, Victor M. Kogan. Role of Catalyst Supports and Active Phase Composition for Synthesis of Oxygenated Hydrocarbons from Ethanol over (K)(Co)MoS_2 Catalysts // The Sixth International Scientific Conference "Advances in Synthesis and Complexing". RUDN University, September 26-30, 2022. P 382.

10. Osman M.E., Maximov V.V., **Dipheko T.D**., Sheshko T.F., Cherednichenko A.G., Nikulshin P.A., Kogan V.M. Study the role of carbon and nano-composite hybrid materials as a support for transitional metal sulfide-based catalysts for higher alcohols

synthesis from syngas // 11th Edition of International Conference on Catalysis, Chemical Engineering and Technology, Japan, May 16-17, 2022.

11. Osman M.E., Maximov V.V., **Dipheko T.D**., Sheshko T.F., Cherednichenko A.G., Kogan V.M. HAS from syngas over supported and modified TMS catalysts: Effect of novel fiber and powder commercial activated carbon supports // The Sixth International Scientific Conference “Advances in Synthesis and Complexing”. RUDN University, September 26-30, 2022. P 402.

12. Osman M.E., Maximov V.V., **Dipheko T.D**., Sheshko T.F., Cherednichenko A.G., Kogan V.M. Production of higher alcohols from syngas and ethanol using K-modified TMS–catalysts supported on graphene nanosheets. The Sixth International Scientific Conference “Advances in Synthesis and Complexing”. RUDN University, September 26-30, 2022. P 403

13. Repev N.A., Osman M.E., Konopatsky A.S., Maximov V.V., **Dipheko T.D**., Kogan V.M. Catalytic activity of supported-$KCoMoS_2$ catalysts in HAS from Syngas: Impact of sulfidation method // The Sixth International Scientific Conference “Advances in Synthesis and Complexing”. RUDN University, September 26-30, 2022. P 441

14. **Dipheko T.D.**, Maximov V.V., Permyakov E.A., Cherednichenko A.G., Kogan V. M. Influence of the composition of the active phase and carrier materials on (K)(Co)MoS_2 catalysts for the conversion of ethanol into various oxygenates // III Interuniversity Conference of Young scientists with international participation "New materials and chemical technologies". Moscow, Russia, December 26 – 27, 2022. P. 181 – 182.

Appendix

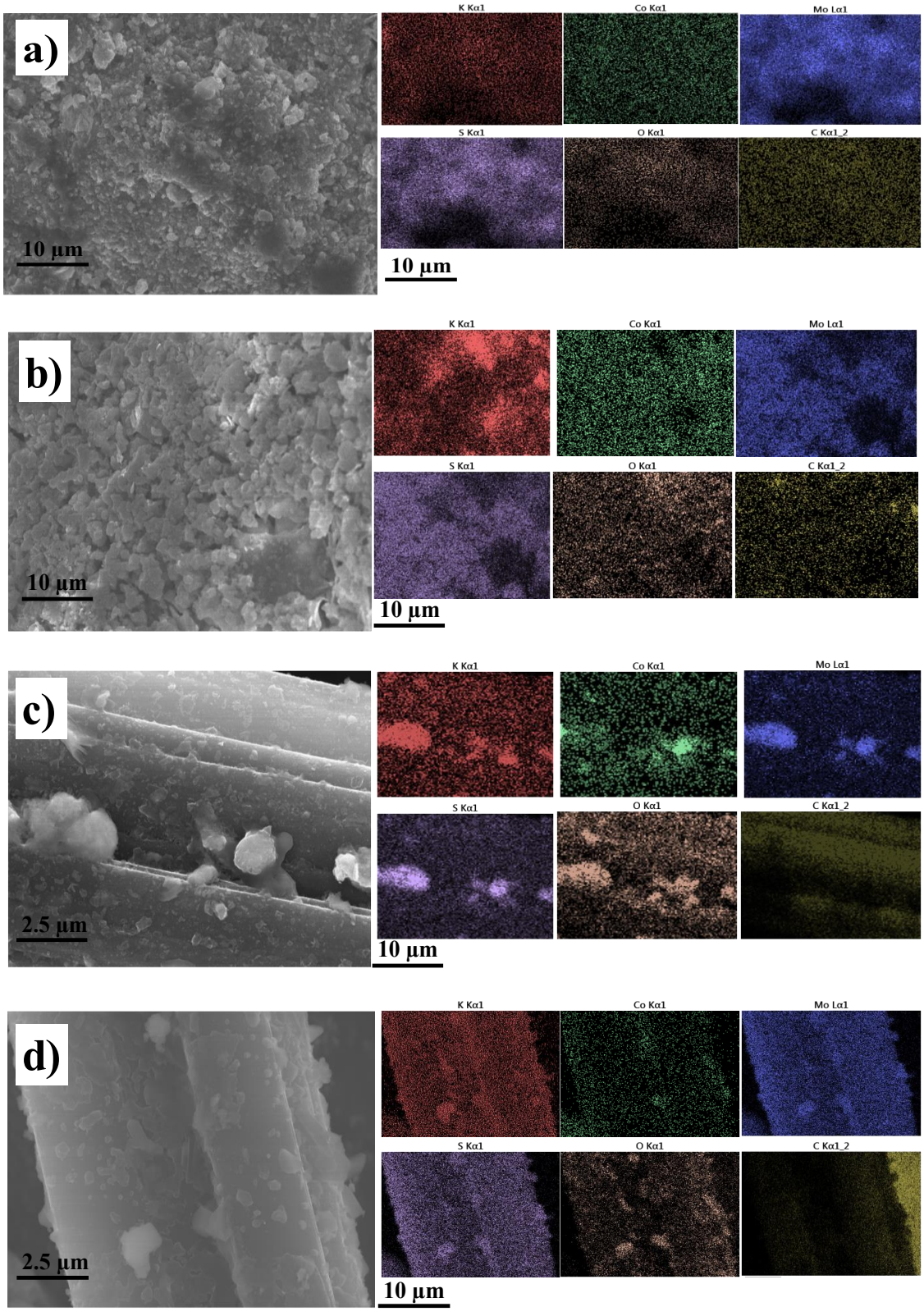

Figure S3.1. SEM/EDX spectrum mapping of K-$CoMoS_2$/DAS (**a**), K-$CoMoS_2$/YPK-1 (**b**), K-$CoMoS_2$/AHM (**c**) and K-$CoMoS_2$/TCA (d)

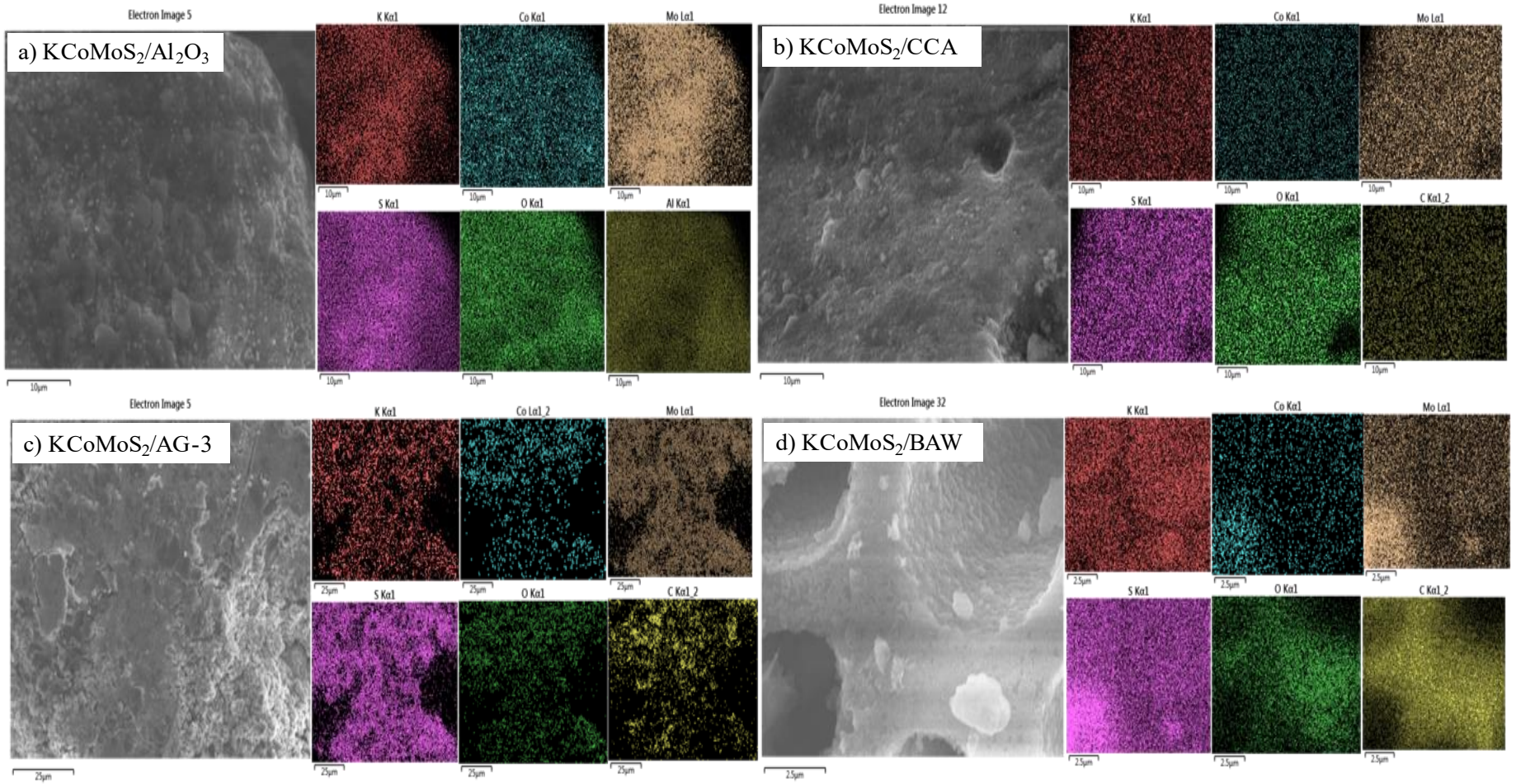

Figure S3.2. SEM/EDX of K-$CoMoS_2$/Sup with elements: Mo, K, S, Co, O, Al, C. [Sup: a) Al_2O_3; b) CCA; c) AG-3; d) BAW].

a)

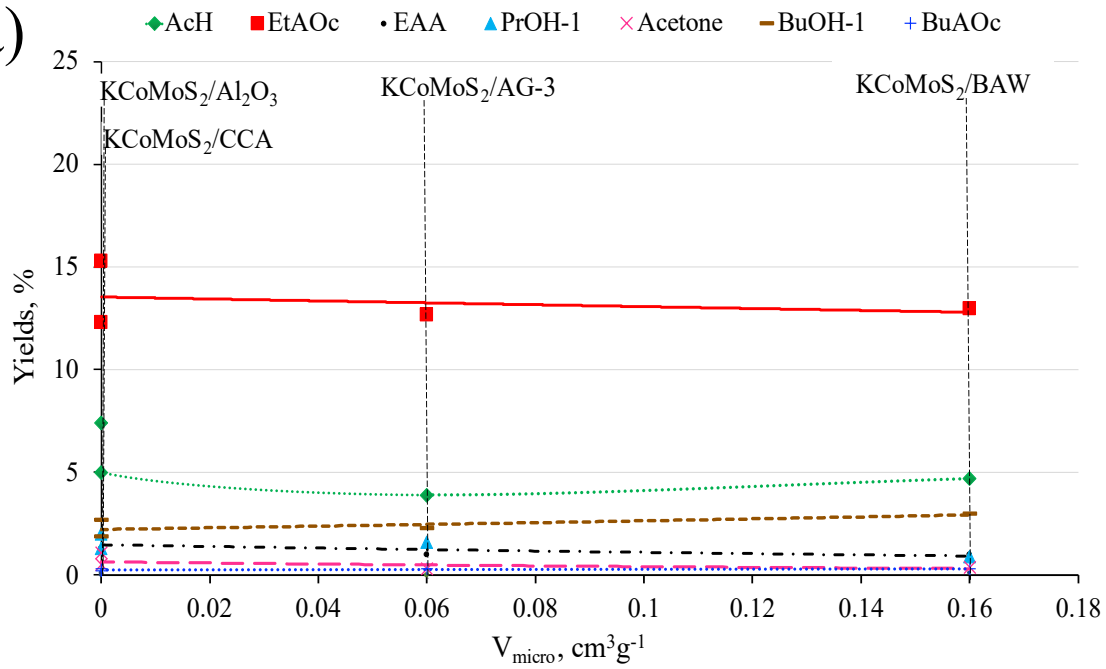
AcH
EtAOc
EAA
PrOH-1
Acetone
BuOH-1
BuAOc
KCoMoS2/Al2O3
KCoMoS2/CCA
KCoMoS2/AG-3
KCoMoS2/BAW
Yields, %
Vmicro, cm3g-1

b)

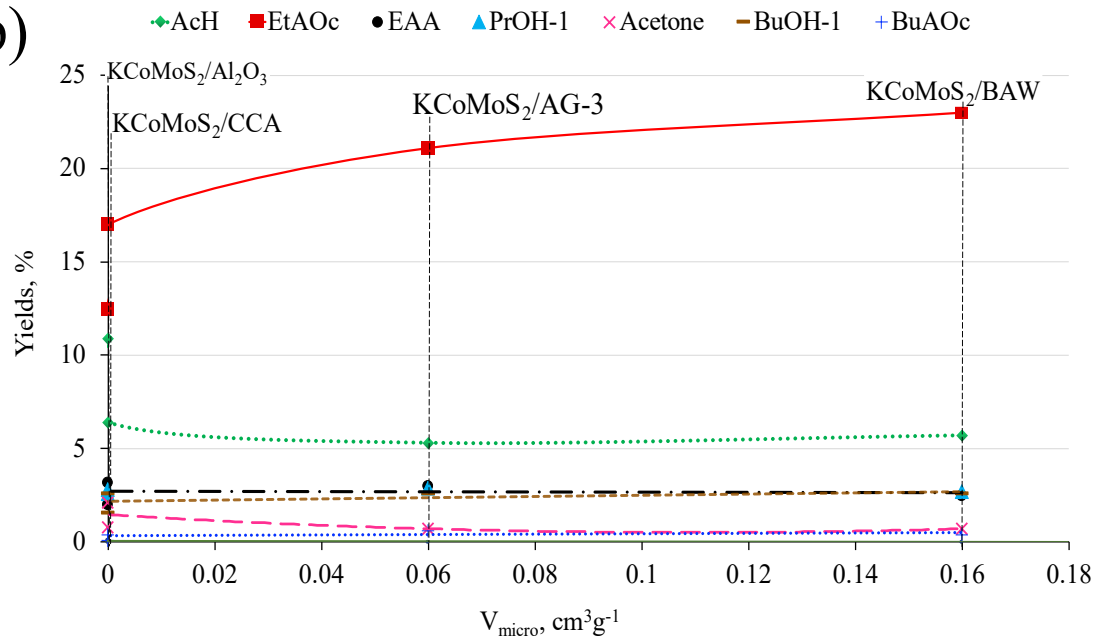
AcH
EtAOc
EAA
PrOH-1
Acetone
BuOH-1
BuAOc
KCoMoS2/Al2O3
KCoMoS2/CCA
KCoMoS2/AG-3
KCoMoS2/BAW
Yields, %
Vmicro, cm3g-1

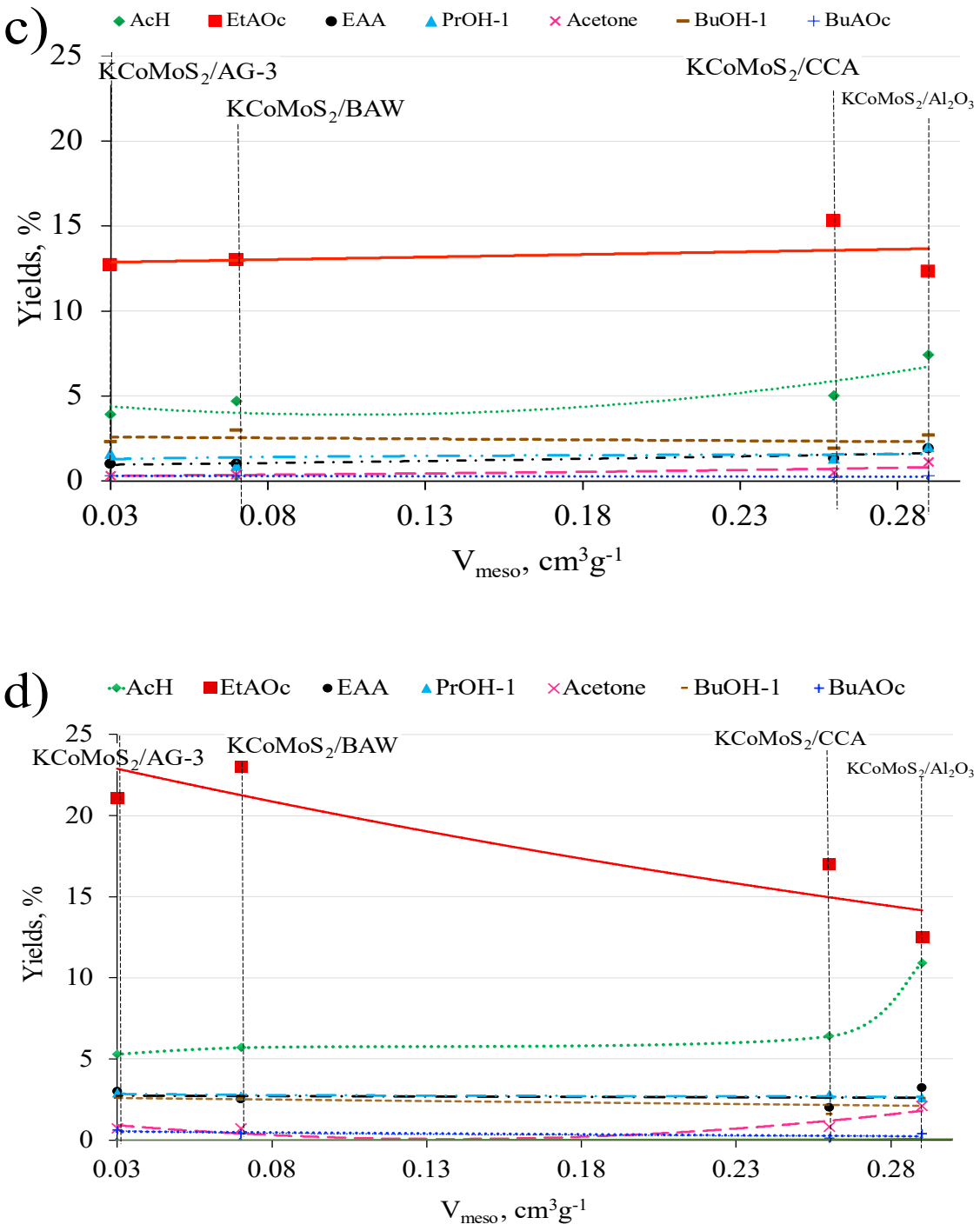

Figure S3.3. Dependence of textural characteristics and main liquid products: a) pore volume (micropore) under H_2; b) pore volume (micropore) under He atm. c) change in the pore volume under H_2 atm; d) change in the pore volume under He atm.

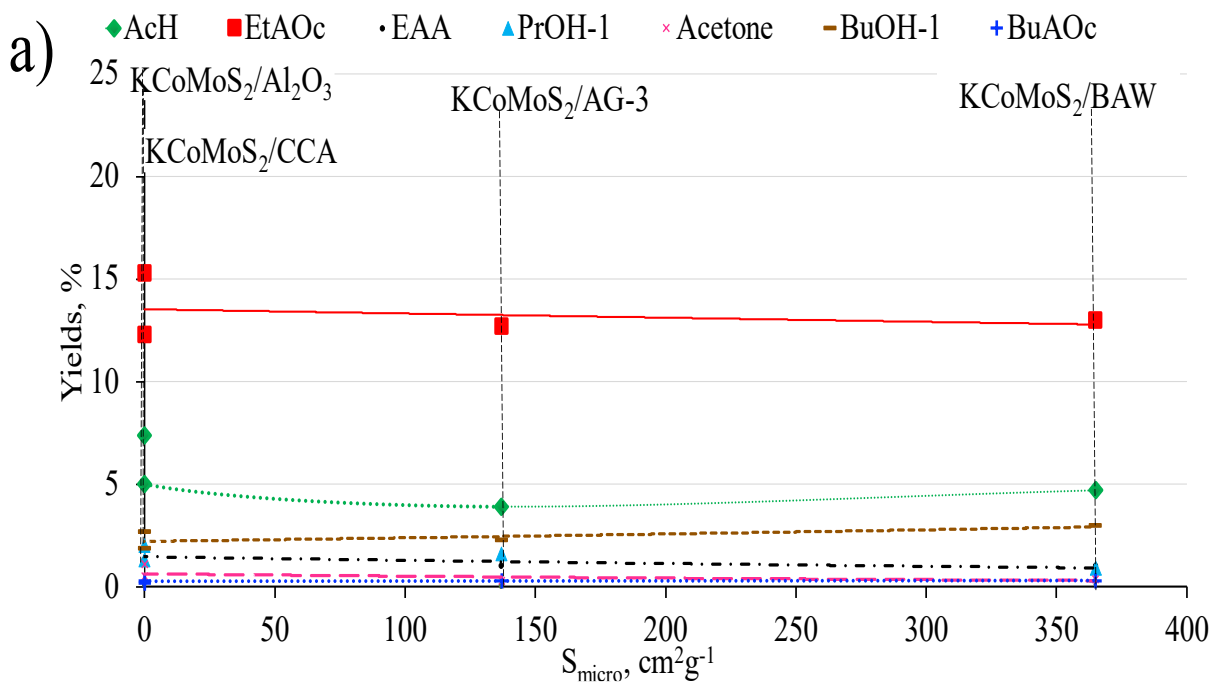
a)
AcH
EtAOc
EAA
PrOH-1
Acetone
BuOH-1
BuAOc
KCoMoS2/Al2O3
KCoMoS2/CCA
KCoMoS2/AG-3
KCoMoS2/BAW
Yields, %
Smicro, cm2g-1

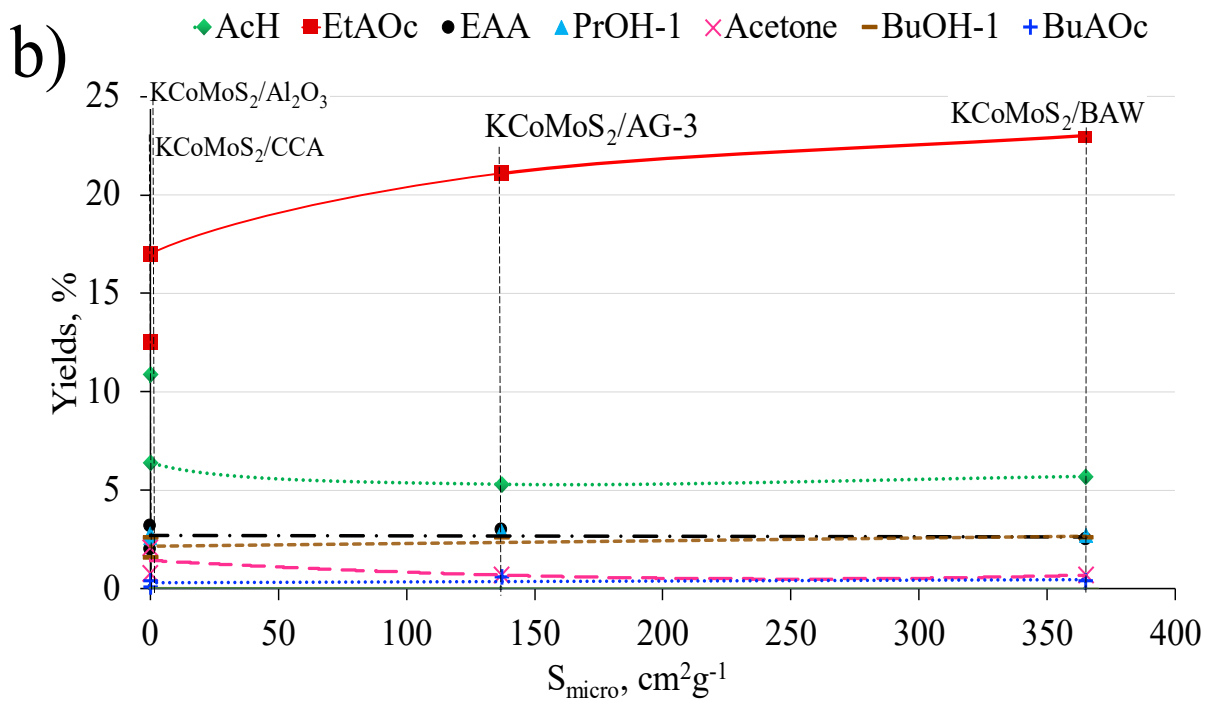
b)
AcH
EtAOc
EAA
PrOH-1
Acetone
BuOH-1
BuAOc
KCoMoS2/Al2O3
KCoMoS2/CCA
KCoMoS2/AG-3
KCoMoS2/BAW
Yields, %
Smicro, cm2g-1

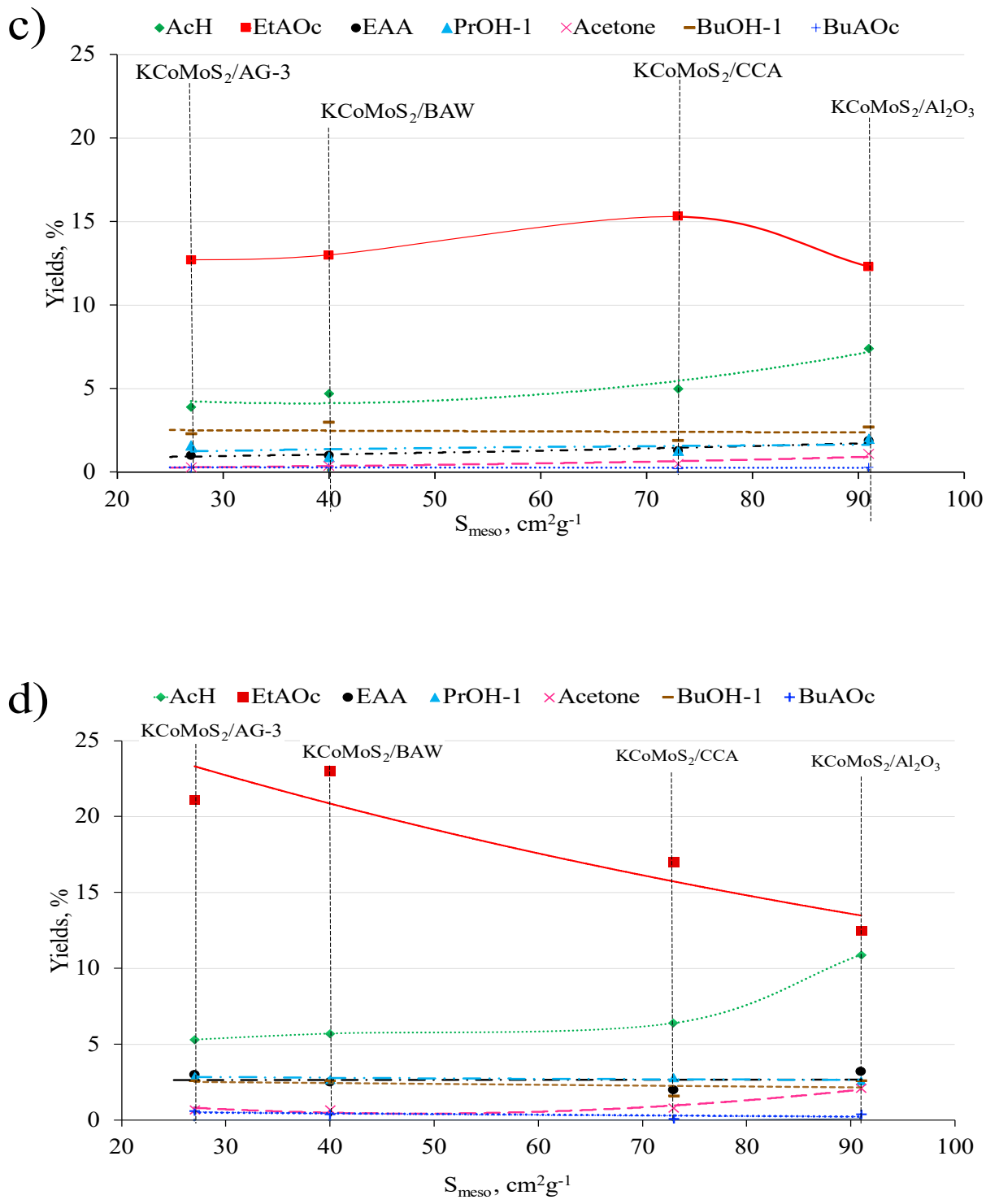

Figure S3.4. Dependence of textural characteristics and main liquid products: a) surface areas (micropore) under H_2 atm; b) surface area (micropore) under He atm. c) change in SSA under H_2 atm; d) change in SSA under He atm

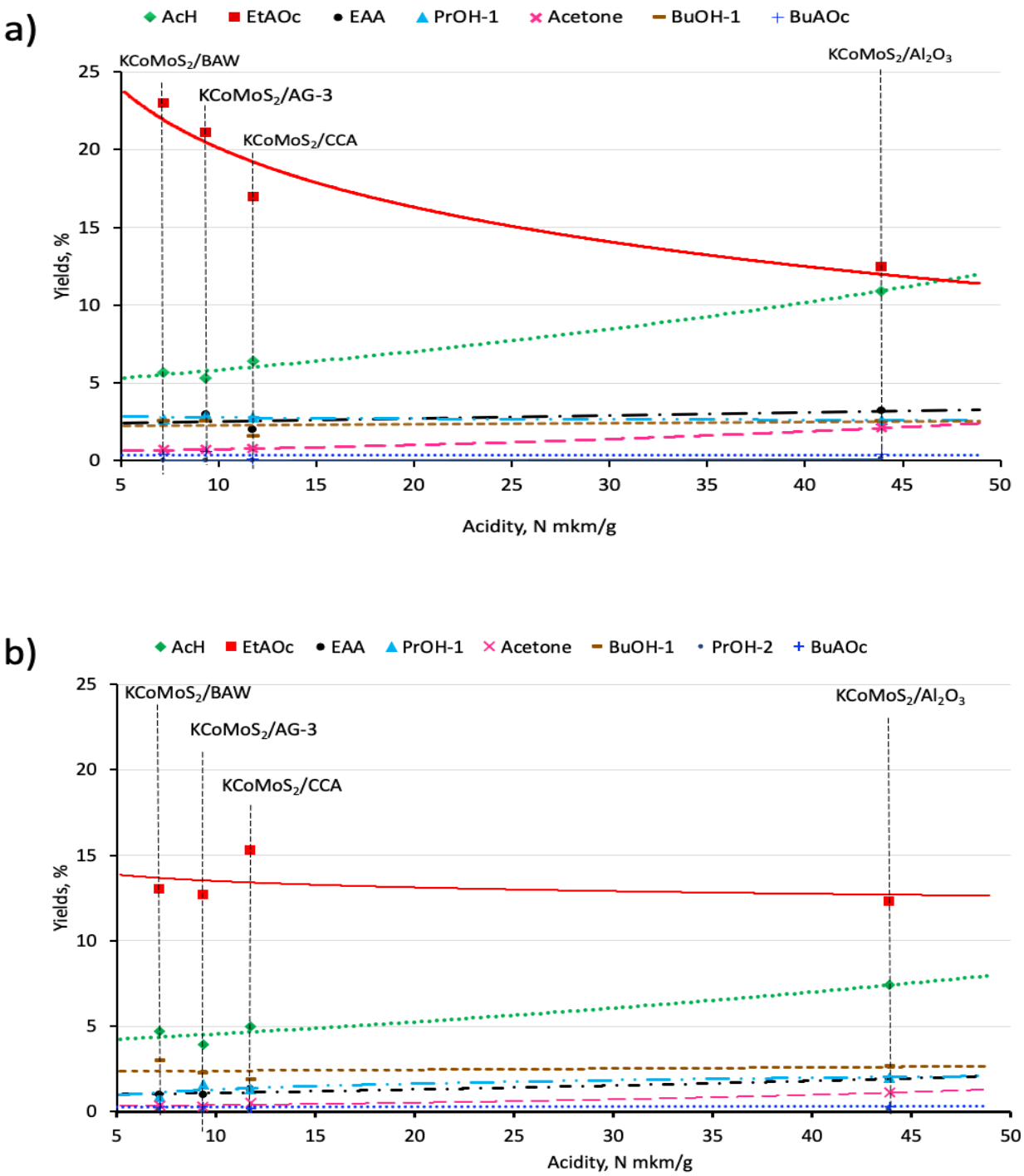

Figure S3.5. Dependence of liquid product yields on catalyst acidity under: (a) He and (b) H_2 atm.

References

[1] Fiorentino G, Ripa M, Ulgiati S. Chemicals from biomass: technological versus environmental feasibility. A review. // Biofuels, Bioprod Biorefining 2017;11:195–214. https://doi.org/10.1002/BBB.1729.

[2] Shamaila S, Sajjad AKL, Ryma N ul A, Farooqi SA, Jabeen N, Majeed S, et al. Advancements in nanoparticle fabrication by hazard free eco-friendly green routes. // Appl Mater Today 2016;5:150–99. https://doi.org/10.1016/J.APMT.2016.09.009.

[3] Hu W, Li D, Yang Y, Li T, Chen H, Liu P. Copper ferrite supported gold nanoparticles as efficient and recyclable catalyst for liquid-phase ethanol oxidation. // J Catal 2018;357:108–17. https://doi.org/10.1016/J.JCAT.2017.11.011.

[4] László L, Mika L, Cséfalvaycséfalvay † Edit, Ron Á, Németh N. Catalytic Conversion of Carbohydrates to Initial Platform Chemicals: // Chemistry and Sustainability. Chem Rev 2017. https://doi.org/10.1021/acs.chemrev.7b00395.

[5] Çelik MB, Özdalyan B, Alkan F. The use of pure methanol as fuel at high compression ratio in a single cylinder gasoline engine. // Fuel 2011;90:1591–8. https://doi.org/10.1016/J.FUEL.2010.10.035.

[6] Turner D, Xu H, Cracknell RF, Natarajan V, Chen X. Combustion performance of bio-ethanol at various blend ratios in a gasoline direct injection engine. // Fuel 2011;90:1999–2006. https://doi.org/10.1016/J.FUEL.2010.12.025.

[7] Dagle RA, Winkelman AD, Ramasamy KK, Lebarbier Dagle V, Weber RS. Ethanol as a Renewable Building Block for Fuels and Chemicals. // Ind Eng Chem Res 2020;59:4843–53. https://doi.org/10.1021/acs.iecr.9b05729.

[8] Abdulrazzaq HT, Schwartz TJ. Catalytic conversion of ethanol to commodity and specialty chemicals. // Elsevier Inc.; 2018. https://doi.org/10.1016/B978-0-12-811458-2.00001-8.

[9] Ob-Eye J, Praserthdam P, Jongsomjit B. Dehydrogenation of ethanol to acetaldehyde over different metals supported on carbon catalysts. // Catalysts

2019;9. https://doi.org/10.3390/catal9010066.

[10] Čičmanec P, Ganjkhanlou Y, Kotera J, Hidalgo JM, Tišler Z, Bulánek R. The effect of vanadium content and speciation on the activity of VO x /ZrO_2 catalysts in the conversion of ethanol to acetaldehyde. // Appl Catal A, Gen J 2018;564:208–17. https://doi.org/10.1016/j.apcata.2018.07.040.

[11] Sánchez AB, Homs N, Miachon S, Dalmon JA, Fierro JLG, Ramírez De La Piscina P. Direct transformation of ethanol into ethyl acetate through catalytic membranes containing Pd or Pd-Zn: Comparison with conventional supported catalysts. // Green Chem 2011;13:2569–75. https://doi.org/10.1039/c1gc15559h.

[12] Ndou AS, Plint N, Coville NJ. Dimerisation of ethanol to butanol over solid-base catalysts. // Appl Catal A Gen 2003;251:337–45. https://doi.org/10.1016/S0926-860X(03)00363-6.

[13] Nanda S, Golemi-Kotra D, McDermott JC, Dalai AK, Gökalp I, Kozinski JA. Fermentative production of butanol: Perspectives on synthetic biology. // N Biotechnol 2017;37:210–21. https://doi.org/10.1016/J.NBT.2017.02.006.

[14] Wu X, Fang G, Tong Y, Jiang D, Liang Z, Leng W, et al. Catalytic Upgrading of Ethanol to n-Butanol: Progress in Catalyst Development. // ChemSusChem 2018;11:71–85. https://doi.org/10.1002/CSSC.201701590.

[15] Angelici C, Weckhuysen BM, Bruijnincx PCA. Chemocatalytic conversion of ethanol into butadiene and other bulk chemicals. // ChemSusChem 2013;6:1595–614. https://doi.org/10.1002/cssc.201300214.

[16] Sun Z, Vasconcelos AC, Bottari G, Stuart MCA, Bonura G, Cannilla C, et al. Efficient catalytic conversion of ethanol to 1-butanol via the guerbet reaction over copper- and nickel-doped porous. // ACS Sustain Chem Eng 2017;5:1738–46. https://doi.org/10.1021/acssuschemeng.6b02494.

[17] Sun J, Wang Y. Recent advances in catalytic conversion of ethanol to chemicals. // ACS Catal 2014;4:1078–90. https://doi.org/10.1021/cs4011343.

[18] Topsøe H, Clausen BS, Massoth FE. Hydrotreating Catalysis. Catalysis 1996:1–269. https://doi.org/10.1007/978-3-642-61040-0_1.

[19] Daage M, Chianelli RR. Structure-Function Relations in Molybdenum Sulfide Catalysts: The "Rim-Edge" Model. // J Catal 1994;149:414–27. https://doi.org/10.1006/JCAT.1994.1308.

[20] Chianelli RR, Daage M, Ledoux MJ. Fundamental Studies of Transition-Metal Sulfide Catalytic Materials. // Adv Catal 1994;40:177–232. https://doi.org/10.1016/S0360-0564(08)60658-6.

[21] Chianelli RR, Berhault G, Raybaud P, Kasztelan S, Hafner J, Toulhoat H. Periodic trends in hydrodesulfurization: In support of the Sabatier principle. // Appl Catal A Gen 2002;227:83–96. https://doi.org/10.1016/S0926-860X(01)00924-3.

[22] Gunturu AK, Kugler EL, Cropley JB, Dadyburjor DB. A kinetic model for the synthesis of high-molecular-weight alcohols over a sulfided Co-K-Mo/C catalyst. // Ind Eng Chem Res 1998;37:2107–15. https://doi.org/10.1021/ie970391z.

[23] Silbernagel BG, Pecoraro TA, Chianelli RR. Electron spin resonance of supported and unsupported molybdenum hydrotreating catalysts. I. Model system studies. // J Catal 1982;78:380–8. https://doi.org/10.1016/0021-9517(82)90321-9.

[24] Delmon B. New technical challenges and recent advances in hydrotreatment catalysis. A critical updating review. // Catal Letters 1993;22:1–32.

[25] S. Kasztelan, H.Toulhoat, J. Grimblot JPB. A geometrical model of the active phase of hydrotreating catalysts. // Appl Catal 1984;13:127–59. https://doi.org/https://doi.org/10.1016/S0166-9834(00)83333-3.

[26] Grønborg SS, Salazar N, Bruix A, Rodríguez-Fernández J, Thomsen SD, Hammer B, et al. Visualizing hydrogen-induced reshaping and edge activation in MoS_2 and Co-promoted MoS_2 catalyst clusters n.d. https://doi.org/10.1038/s41467-018-04615-9.

[27] Topsøe H. The role of Co – Mo – S type structures in hydrotreating catalysts 2007;322:3–8. https://doi.org/10.1016/j.apcata.2007.01.002.

[28] Topsøie H, Candia R, Topsøe N -Y, Clausen BS, Topsøe H. On The State of the Co-MO-S Model. // Bull Des Sociétés Chim Belges 1984;93:783–806. https://doi.org/10.1002/BSCB.19840930820.

[29] Ho TC. Catalysis Reviews Science and Engineering Hydrodenitrogenation Catalysis Hydrodenitrogenation Catalysis. // Catal Rev Sci Eng 1988;30:1:117–60. https://doi.org/10.1080/01614948808078617.

[30] Moses PG. TRANSITION METAL SULPHIDE CATALYSTS: A DFT STUDY OF STRUCTURE AND REACTIVITY. 2008.

[31] Raybaud P. Understanding and predicting improved sulfide catalysts: Insights from first principles modeling. // Appl Catal A Gen 2007;322:76–91. https://doi.org/10.1016/J.APCATA.2007.01.005.

[32] Sun M, Nelson AE, Adjaye J. Ab initio DFT study of hydrogen dissociation on MoS2, NiMoS, and CoMoS: mechanism, kinetics, and vibrational frequencies. // J Catal 2005;233:411–21. https://doi.org/10.1016/J.JCAT.2005.05.009.

[33] Andersen A, Kathmann SM, Lilga MA, Albrecht KO, Hallen RT, Mei D. Adsorption of potassium on MoS_2(100) surface: A first-principles investigation. // J Phys Chem C 2011;115:9025–40. https://doi.org/10.1021/JP110069R.

[34] Besenbacher F, Brorson M, Clausen BS, Helveg S, Hinnemann B, Kibsgaard J, et al. Recent STM, DFT and HAADF-STEM studies of sulfide-based hydrotreating catalysts: Insight into mechanistic, structural and particle size effects. // Catal Today 2008. https://doi.org/10.1016/j.cattod.2007.08.009.

[35] Bara C, Devers E, Digne M, Lamic-Humblot AF, Pirngruber GD, Carrier X. Surface Science Approaches for the Preparation of Alumina-Supported Hydrotreating Catalysts. // ChemCatChem 2015;7:3422–40. https://doi.org/10.1002/CCTC.201500436.

[36] Permyakov EA, Dorokhov VS, Maximov V V., Nikulshin PA, Pimerzin AA, Kogan VM. Computational and experimental study of the second metal effect on the structure and properties of bi-metallic MeMoS-sites in transition metal sulfide catalysts. // Catal Today 2018;305:19–27. https://doi.org/10.1016/j.cattod.2017.10.041.

[37] Dumeignil F, Paul J, Veilly E, Qian EW, Ishihara A, Payen E, et al. Description of coordinatively unsaturated sites regeneration over MoS_2 -based HDS catalysts using ^{35}S experiments combined with computer simulations. // Appl Catal A Gen 2009;289:51–8. https://doi.org/10.1016/j.apcata.2005.04.025.

[38] Mross WD, Mross W-D. Alkali Doping in Heterogeneous Catalysis. // CATAL REV-SCI ENG 1983;25:591–637. https://doi.org/10.1080/01614948308078057.

[39] Tatsumi T, Muramatsu A, Tominaga H o. Supported molybdenum catalysts for alcohol synthesis from CO-H_2. // Appl Catal 1987;34:77–88. https://doi.org/10.1016/S0166-9834(00)82447-1.

[40] Hagen J. Concepts of Modern Catalysis and Kinetics Catalysis from A to Z Principles and Practice of Heterogeneous Catalysis Catalytic Membranes and Membrane Reactors Spectroscopy in Catalysis (Industrial Catalysis). 2006.

[41] Ishutenko D, Nikulshin P, Pimerzin A. Relation between composition and morphology of K(Co)MoS active phase species and their performances in hydrotreating of model FCC gasoline. // Catal Today 2016;271:16–27. https://doi.org/10.1016/J.CATTOD.2015.11.025.

[42] Xu J, Gong X, Hu R, Liu Z wen, Liu Z tie. Highly active K-promoted Cu/β-Mo_2C catalysts for reverse water gas shift reaction: Effect of potassium. // Mol Catal 2021;516:2468–8231. https://doi.org/10.1016/J.MCAT.2021.111954.

[43] Maximov V V., Permyakov EA, Dorokhov VS, Wang A, Kooyman PJ, Kogan VM. Effect of Promoter Nature on Synthesis Gas Conversion to Alcohols over (K)$MeMoS_2/Al_2O_3$ Catalysts. // ChemCatChem 2020;12:1443–52.

https://doi.org/10.1002/cctc.201901698.

[44] Shi XR, Jiao H, Hermann K, Wang J. CO hydrogenation reaction on sulfided molybdenum catalysts. // J Mol Catal A Chem 2009;312:7–17. https://doi.org/10.1016/J.MOLCATA.2009.06.025.

[45] Chen YY, Dong M, Qin Z, Wen XD, Fan W, Wang J. A DFT study on the adsorption and dissociation of methanol over MoS 2 surface. // J Mol Catal A Chem 2011;338:44–50. https://doi.org/10.1016/j.molcata.2011.01.024.

[46] Klier K, Herman RG, Nunan JG, Smith KJ, Bogdan CE, Young CW, et al. Mechanism of methanol and higher oxygenate synthesis. vol. 36. 1988. https://doi.org/10.1016/S0167-2991(09)60506-1.

[47] Liu Z, Li X, Close MR, Kugler EL, Petersen JL, Dadyburjor DB. Screening of Alkali-Promoted Vapor-Phase-Synthesized Molybdenum Sulfide Catalysts for the Production of Alcohols from Synthesis Gas. 1997.

[48] Youchang X, Naasz BN, Somorjai GA. Alcohol synthesis from Co and H_2 over molybdenum sulfide. The effect of pressure and promotion by potassium carbonate. // Appl Catal 1986;27:233–41. https://doi.org/10.1016/S0166-9834(00)82920-6.

[49] Benavente E, Santa Ana MA, Mendizábal F, González G. Intercalation chemistry of molybdenum disulfide. // Coord Chem Rev 2002;224:87–109. https://doi.org/10.1016/S0010-8545(01)00392-7.

[50] Escobar-Alarcón L, Klimova T, Escobar-Aguilar J, Romero S, Morales-Ramírez C, Solís-Casados DA. Preparation and characterization of Al_2O_3–MgO catalytic supports modified with lithium. // Fuel 2013;110:278–85. https://doi.org/10.1016/J.FUEL.2012.10.013.

[51] Iranmahboob J, Toghiani H, Hill DO. Dispersion of alkali on the surface of Co-MoS_2/clay catalyst: a comparison of K and Cs as a promoter for synthesis of alcohol. // Appl Catal A Gen 2003;247:207–18. https://doi.org/10.1016/S0926-860X(03)00092-9.

[52] Ferrari D, Budroni G, Bisson L, Rane NJ, Dickie BD, Kang JH, et al. Effect of potassium addition method on MoS2 performance for the syngas to alcohol reaction. // Appl Catal A Gen 2013;462–463:302–9. https://doi.org/10.1016/j.apcata.2013.05.006.

[53] Lee JH, Hamrin CE, Davis BH. Deamination of 2-octylamine with metal nitride and oxide catalysts. // Appl Catal A Gen 1994;111:11–27. https://doi.org/10.1016/0926-860X(94)80064-2.

[54] Xiao H, Li D, Li W, Sun Y. Study of induction period over K_2CO_3/MoS_2 catalyst for higher alcohols synthesis. // Fuel Process Technol 2010;91:383–7. https://doi.org/10.1016/j.fuproc.2009.07.004.

[55] Costa D, Arrouvel C, Breysse M, Toulhoat H, Raybaud P. Edge wetting effects of γ-Al_2O_3 and anatase-TiO_2 supports by MoS_2 and CoMoS active phases: A DFT study. // J Catal 2007;246:325–43. https://doi.org/10.1016/J.JCAT.2006.12.007.

[56] Surisetty VR, Eswaramoorthi I, Dalai AK. Comparative study of higher alcohols synthesis over alumina and activated carbon-supported alkali-modified MoS2 catalysts promoted with group VIII metals. // Fuel 2012;96:77–84. https://doi.org/10.1016/J.FUEL.2011.12.054.

[57] Luk HT, Forster T, Mondelli C, Siol S, Curulla-Ferré D, Stewart JA, et al. Carbon nanofibres-supported KCoMo catalysts for syngas conversion into higher alcohols. // Catal Sci Technol 2018;8:187–200. https://doi.org/10.1039/c7cy01908d.

[58] Ferdous D, Dalai AK, Adjaye J, Kotlyar L. Surface morphology of $NiMo/Al_2O_3$ catalysts incorporated with boron and phosphorus: Experimental and simulation. // Appl Catal A Gen 2005;294:80–91. https://doi.org/10.1016/J.APCATA.2005.07.025.

[59] Surisetty VR, Dalai AK, Kozinski J. Synthesis of higher alcohols from synthesis gas over Co-promoted alkali-modified MoS_2 catalysts supported on MWCNTs. // Appl Catal A Gen 2010;385:153–62. https://doi.org/10.1016/j.apcata.2010.07.009.

[60] Li D, Yang C, Qi H, Zhang H, Li W, Sun Y, et al. Higher alcohol synthesis over a La promoted Ni/K_2CO_3/MoS_2 catalyst. // Catal Commun 2004;5:605–9. https://doi.org/10.1016/j.catcom.2004.07.011.

[61] Li Z, Fu Y, Bao J, Jiang M. Effect of cobalt promoter on Co – Mo – K / C catalysts used for mixed alcohol synthesis. // Appl Catal 2001;220:21–30. https://doi.org/https://doi.org/10.1016/S0926-860X(01)00646-9.

[62] Iranmahboob J, Hill DO, Toghiani H. K_2CO_3/Co-MoS_2/clay catalyst for synthesis of alcohol: influence of potassium and cobalt. // Appl Catal A Gen 2002;231:99–108. https://doi.org/10.1016/S0926-860X(01)01011-0.

[63] Ma X, Lin G, Zhang H. Co-Mo-K sulfide-based catalyst promoted by multiwalled carbon nanotubes for higher alcohol synthesis from syngas. // Chinese J Catal 2006;27:1019–27. https://doi.org/10.1016/S1872-2067(06)60053-3.

[64] Nikulshin PA, Mozhaev A V., Pimerzin AA, Konovalov V V., Pimerzin AA. CoMo/Al_2O_3 catalysts prepared on the basis of Co 2Mo 10-heteropolyacid and cobalt citrate: Effect of Co/Mo ratio. // Fuel 2012;100:24–33. https://doi.org/10.1016/J.FUEL.2011.11.028.

[65] Xiang M, Li D, Xiao H, Zhang J, Qi H, Li W, et al. Synthesis of higher alcohols from syngas over Fischer-Tropsch elements modified K/β-Mo_2C catalysts. // Fuel 2008;87:599–603. https://doi.org/10.1016/J.FUEL.2007.01.041.

[66] Xiang M, Li D, Li W, Zhong B, Sun Y. K/Fe/β-Mo2C: A novel catalyst for mixed alcohols synthesis from carbon monoxide hydrogenation. // Catal Commun 2007;8:88–90. https://doi.org/10.1016/J.CATCOM.2006.05.036.

[67] Phung TK. Copper-based catalysts for ethanol dehydrogenation and dehydrogenative coupling into hydrogen, acetaldehyde and ethyl acetate. // Int J Hydrogen Energy 2021. https://doi.org/10.1016/j.ijhydene.2021.11.253.

[68] Wang QN, Shi L, Lu AH. Highly Selective Copper Catalyst Supported on Mesoporous Carbon for the Dehydrogenation of Ethanol to Acetaldehyde. //

ChemCatChem 2015;7:2846–52. https://doi.org/10.1002/cctc.201500501.

[69] Morales M V., Asedegbega-Nieto E, Bachiller-Baeza B, Guerrero-Ruiz A. Bioethanol dehydrogenation over copper supported on functionalized graphene materials and a high surface area graphite. // Carbon N Y 2016;102:426–36. https://doi.org/10.1016/j.carbon.2016.02.089.

[70] Franckaerts J, Froment GF. Kinetic study of the dehydrogenation of ethanol. // Chem Eng Sci 1964;19:807–18. https://doi.org/10.1016/0009-2509(64)85092-2.

[71] Jang W-J, Shim J-O, Kim H-M, Yoo S-Y, Roh H-S. A review on dry reforming of methane in aspect of catalytic properties. // Catal Today 2019;324:15–26. https://doi.org/10.1016/j.cattod.2018.07.032.

[72] Riittonen T, Toukoniitty E, Madnani DK, Leino A-R, Kordas K, Szabo M, et al. One-Pot Liquid-Phase Catalytic Conversion of Ethanol to 1-Butanol over Aluminium Oxide-The Effect of the Active Metal on the Selectivity. // Catalysts 2012;2:68–84. https://doi.org/10.3390/catal2010068.

[73] Sushkevich VL, Ivanova II, Ordomsky V V, Taarning E. Design of a Metal-Promoted Oxide Catalyst for the Selective Synthesis of Butadiene from Ethanol n.d. https://doi.org/10.1002/cssc.201402346.

[74] Dowson GRM, Haddow MF, Lee J, Wingad RL, Wass DF. Catalytic conversion of ethanol into an advanced biofuel: Unprecedented selectivity for n-butanol. // Angew Chemie - Int Ed 2013;52:9005–8. https://doi.org/10.1002/ANIE.201303723.

[75] Marcu I-C, Tanchoux N, Fajula F, Didier Tichit •. Catalytic Conversion of Ethanol into Butanol over M–Mg–Al Mixed Oxide Catalysts (M 5 Pd, Ag, Mn, Fe, Cu, Sm, Yb) Obtained from LDH Precursors. // Catal Letters 2013;143:23–30. https://doi.org/10.1007/s10562-012-0935-9.

[76] Van Veen JAR, Gerkema E, Van Der Kraan AM, Knoester A. A real support effect on the activity of fully sulphided CoMoS for the hydrodesulphurization of thiophene. // J Chem Soc Chem Commun 1987;0:1684–6.

https://doi.org/10.1039/C39870001684.

[77] Candia R, Sørensen O, Villadsen Jør, Topsøe N -Y, Clausen BS, Topsøe H. Effect of Sulfiding Temperature on Activity and Structures of CO-MO/Al_2O_3 Catalysts. ii. // Bull Des Sociétés Chim Belges 1984;93:763–74. https://doi.org/10.1002/BSCB.19840930818.

[78] Bouwens SMAM, Barthe-Zahir N, De Beer VHJ, Prins R. The role of Ni in sulfided carbon-supported Ni□Mo hydrodesulfurization catalysts. // J Catal 1991;131:326–34. https://doi.org/10.1016/0021-9517(91)90268-9.

[79] Duchet JC, van Oers EM, de Beer VHJ, Prins R. Carbon-supported sulfide catalysts. // J Catal 1983;80:386–402. https://doi.org/10.1016/0021-9517(83)90263-4.

[80] Vissers JPR, Scheffer B, de Beer VHJ, Moulijn JA, Prins R. Effect of the support on the structure of Mo-based hydrodesulfurization catalysts: Activated carbon versus alumina. // J Catal 1987;105:277–84. https://doi.org/10.1016/0021-9517(87)90058-3.

[81] Christensen JM, Mortensen PM, Trane R, Jensen PA, Jensen AD. Effects of H_2S and process conditions in the synthesis of mixed alcohols from syngas over alkali promoted cobalt-molybdenum sulfide. // Appl Catal A Gen 2009;366:29–43. https://doi.org/10.1016/j.apcata.2009.06.034.

[82] Christensen JM, Jensen PA, Schiødt NC, Jensen AD. Coupling of Alcohols over Alkali-Promoted Cobalt-Molybdenum Sulfide. // ChemCatChem 2010;2:523–6. https://doi.org/10.1002/cctc.200900239.

[83] Dorokhov VS, Permyakov EA, Nikulshin PA, Maximov V V., Kogan VM. Experimental and computational study of syngas and ethanol conversion mechanisms over K-modified transition metal sulfide catalysts. // J Catal 2016;344:841–53. https://doi.org/10.1016/j.jcat.2016.08.005.

[84] Taborga Claure M, Lee LC, Goh JW, Gelbaum LT, Agrawal PK, Jones CW. Assessing C_3–C_4 alcohol synthesis pathways over a MgAl oxide supported K/MoS_2

catalyst via $^{13}C_2$-ethanol and $^{13}C_2$-ethylene co-feeds. // J Mol Catal A Chem 2016;423:224–32. https://doi.org/10.1016/j.molcata.2016.06.025.

[85] París RS. Catalytic conversion of biomass-derived synthesis gas to liquid fuels. 2013.

[86] Chiang SW, Chang CC, Shie JL, Chang CY, Ji DR, Tseng JY, et al. Synthesis of alcohols and alkanes from CO and H_2 over MOS_2/γ-AL_2O_3 catalyst in a packed bed with continuous flow. // Energies 2012;5:4147–64. https://doi.org/10.3390/en5104147.

[87] Zaman S, Smith KJ. A Review of Molybdenum Catalysts for Synthesis Gas Conversion to Alcohols: Catalysts, Mechanisms and Kinetics. 2012;54:41–132. https://doi.org/10.1080/01614940.2012.627224.

[88] Li H, Chen T, Wang G. Effects of Ethanol Co - feeding in Higher Alcohols Synthesis from Syngas over K - MoS_2 Catalyst. // Catal Letters 2021. https://doi.org/10.1007/s10562-021-03869-1.

[89] Sangeetha DN, Santosh MS, Selvakumar M. Flower-like carbon doped MoS_2/Activated carbon composite electrode for superior performance of supercapacitors and hydrogen evolution reactions. // Alloys Compd 2020;831. https://doi.org/10.1016/J.JALLCOM.2020.154745.

[90] Yan Y, Xia B, Xu Z, Wang X. Recent development of molybdenum sulfides as advanced electrocatalysts for hydrogen evolution reaction. // ACS Catal 2014;4:1693–705. https://doi.org/10.1021/CS500070X/ASSET/IMAGES/LARGE/CS-2014-00070X_0008.JPEG.

[91] Benck JD, Hellstern TR, Kibsgaard J, Chakthranont P, Jaramillo TF. Catalyzing the Hydrogen Evolution Reaction (HER) with Molybdenum Sulfide Nanomaterials 2014. https://doi.org/10.1021/cs500923c.

[92] Kibsgaard J, Jaramillo TF, Besenbacher F. Building an appropriate active-site motif

into a hydrogen-evolution catalyst with thiomolybdate $[Mo_3S_{13}]_2-$ clusters. // Nat Chem 2014 63 2014;6:248–53. https://doi.org/10.1038/nchem.1853.

[93] Wang ZZ, Han WF, Liu HZ. Hydrothermal synthesis of sulfur-resistant MoS_2 catalyst for methanation reaction // Catal Commun 2016;84:120–3. https://doi.org/10.1016/J.CATCOM.2016.06.016.

[94] Li Y, Wang R, Chang L. Study of reactions over sulfide catalysts in $CO–CO_2–H_2–H_2O$ system. // Catal Today 1999;51:25–38. https://doi.org/10.1016/S0920-5861(99)00005-X.

[95] Anderson AB, Yu J. Methane conversion and Fischer—Tropsch catalysis over MoS_2: Predictions and interpretations from molecular orbital theory // J Catal 1989;119:135–45. https://doi.org/10.1016/0021-9517(89)90141-3.

[96] Zaman S, Smith KJ. A review of molybdenum catalysts for synthesis gas conversion to alcohols: Catalysts, mechanisms and kinetics // Catal Rev - Sci Eng 2012;54:41–132. https://doi.org/10.1080/01614940.2012.627224.

[97] Williams S. Synthesis Gas Conversion to Aliphatic Alcohols : Study of MoS_2 catalytic systems Synthesis Gas Conversion to Aliphatic Alcohols : Study of MoS_2 catalytic systems 2010.

[98] Luk HT, Mondelli C, Ferré DC, Stewart JA, Pérez-Ramírez J. Status and prospects in higher alcohols synthesis from syngas // Chem Soc Rev 2017;46:1358–426. https://doi.org/10.1039/c6cs00324a.

[99] Hong X, Chan K, Tsai C, Nørskov JK. How Doped MoS2 Breaks Transition-Metal Scaling Relations for CO_2 Electrochemical Reduction. ACS Catal 2016;6:4428–37. https://doi.org/10.1021/ACSCATAL.6B00619/ASSET/IMAGES/LARGE/CS-2016-006192_0008.JPEG.

[100] Huang M, Cho K. Density functional theory study of CO hydrogenation on a MoS_2 surface. // J Phys Chem C 2009;113:5238–43. https://doi.org/10.1021/jp807705y.

[101] Cheng E, McCullough L, Noh H, Farha O, Hupp J, Notestein J. Isobutane Dehydrogenation over Bulk and Supported Molybdenum Sulfide Catalysts. Ind Eng Chem Res 2020;59:1113–22. https://doi.org/10.1021/acs.iecr.9b05844.

[102] McCullough LR, Childers DJ, Watson RA, Kilos BA, Barton DG, Weitz E, et al. Acceptorless Dehydrogenative Coupling of Neat Alcohols Using Group VI Sulfide Catalysts. // ACS Sustain Chem Eng 2017;5:4890–6. https://doi.org/10.1021/acssuschemeng.7b00303.

[103] Chianelli RR, Berhault G, Torres B. Unsupported transition metal sulfide catalysts: 100 years of science and application. // Catal Today 2009;147:275–86. https://doi.org/10.1016/J.CATTOD.2008.09.041.

[104] Sun M, Adjaye J, Nelson AE. Theoretical investigations of the structures and properties of molybdenum-based sulfide catalysts. // Appl Catal A Gen 2004;263:131–43. https://doi.org/10.1016/j.apcata.2003.12.011.

[105] Grigorieva A.M., Mukhin V.M. KVN. Production and research of active carbons based on lignin. Chem Ind Today 2012;9:30–5.

[106] Christensen JM, Mortensen PM, Trane R, Jensen PA, Jensen AD. Effects of H2S and process conditions in the synthesis of mixed alcohols from syngas over alkali promoted cobalt-molybdenum sulfide. // Appl Catal A Gen 2009;366:29–43. https://doi.org/10.1016/J.APCATA.2009.06.034.

[107] K. S. W. Sing, D. H. Everett, R. A. W. Haul, L. Moscou, R. A. Pierotti JR and TS. Reporting Physisorption Data for Gas/Solid Systems with Special Reference to the Determination of Surface Area and Porosity. // Pure Appl Chem 1985;57:603–19.

[108] Nikulshin PA, Ishutenko DI, Mozhaev AA, Maslakov KI, Pimerzin AA. Effects of composition and morphology of active phase of $CoMo/Al_2O_3$ catalysts prepared using Co_2Mo_{10}-heteropolyacid and chelating agents on their catalytic properties in HDS and HYD reactions. // J Catal 2014;312:152–69. https://doi.org/10.1016/j.jcat.2014.01.014.

[109] Breysse M, Afanasiev P, Geantet C, Vrinat M. Overview of support effects in hydrotreating catalysts. // Catal Today 2003;86:5–16. https://doi.org/10.1016/S0920-5861(03)00400-0.

[110] Sato AG, Volanti DP, Meira DM, Damyanova S, Longo E, Bueno JMC. Effect of the ZrO_2 phase on the structure and behavior of supported Cu catalysts for ethanol conversion. // J Catal 2013;307:1–17. https://doi.org/10.1016/j.jcat.2013.06.022.

[111] Carrasco-Marín F, Mueden A, Moreno-Castilla C. Surface-treated activated carbons as catalysts for the dehydration and dehydrogenation reactions of ethanol. // J Phys Chem B 1998;102:9239–44. https://doi.org/10.1021/jp981861l.

[112] Dugulan AI, van Veen JAR, Hensen EJM. On the structure and hydrotreating performance of carbon-supported CoMo- and NiMo-sulfides. // Catal B Environ 2013;142–143:178–86. https://doi.org/10.1016/j.apcatb.2013.05.013.

[113] Hydroprocessing CC. Carbons and Carbon-supported Catalysts in Hydroprocessing. vol. 2009. 2009. https://doi.org/10.1016/s1351-4180(09)70100-x.

[114] Kogan VM, Rozhdestvenskaya NN. ^{35}S tracer study of the effect of support on the nature of the active sites of Co(Ni)Mo sulphide catalysts supported on Al_2O_3 and activated carbon. // Oil Gas Sci Technol 2006;61:547–59. https://doi.org/10.2516/ogst:2006028a.

[115] Vradman L, Landau M V., Kantorovich D, Koltypin Y, Gedanken A. Evaluation of metal oxide phase assembling mode inside the nanotubular pores of mesostructured silica. // Microporous Mesoporous Mater 2005;79:307–18. https://doi.org/10.1016/j.micromeso.2004.11.023.

[116] Wacharasindhu S, Likitmaskul S, Punnakanta L, Chaichanwatanakul K, Angsusingha K, Tuchinda C. INTERNATIONAL UNION OF PURE AND APPLIED CHEMISTRY. J Med Assoc Thail 1998;81:420–30.

[117] Chen T, Wang R, Li L, Li Z, Zang S. MOF-derived Co_9S_8/MoS_2 embedded in tri-

doped carbon hybrids for efficient electrocatalytic hydrogen evolution. // J Energy Chem 2020;44:90–6. https://doi.org/10.1016/j.jechem.2019.09.018.

[118] Szymański GS, Rychlicki G. Catalytic conversion of propan-2-ol on carbon catalysts. Carbon N Y 1993;31:247–57. https://doi.org/10.1016/0008-6223(93)90028-9.

[119] Kozlowski JT, Davis RJ. Heterogeneous catalysts for the guerbet coupling of alcohols. // ACS Catal 2013;3:1588–600. https://doi.org/10.1021/cs400292f.

[120] Jiang Y, Lu J, Sun K, Ma L, Ding J. Esterification of oleic acid with ethanol catalyzed by sulfonated cation exchange resin: Experimental and kinetic studies. Energy Convers Manag 2013;76:980–5. https://doi.org/10.1016/j.enconman.2013.08.011.

[121] Jin L, Zhang Y, Dombrowski JP, Chen CH, Pravatas A, Xu L, et al. ZnO/$La_2O_2CO_3$ layered composite: A new heterogeneous catalyst for the efficient ultra-fast microwave biofuel production. // Appl Catal B Environ 2011;103:200–5. https://doi.org/10.1016/j.apcatb.2011.01.027.

[122] Carotenuto G, Tesser R, Di Serio M, Santacesaria E. Kinetic study of ethanol dehydrogenation to ethyl acetate promoted by a copper/copper-chromite based catalyst. // Catal Today 2013;203:202–10. https://doi.org/10.1016/j.cattod.2012.02.054.

[123] Granger P, Ordonez S, Ramirez Reina T, Ketabchi E, Pastor-Pérez L, Arellano-García H. Influence of Reaction Parameters on the Catalytic Upgrading of an Acetone, Butanol, and Ethanol (ABE) Mixture: Exploring New Routes for Modern Biorefineries. // Front Chem | WwwFrontiersinOrg 2020;1:906. https://doi.org/10.3389/fchem.2019.00906.

[124] Fatimah I, Rubiyanto D, Taushiyah A, Najah FB, Azmi U, Sim YL. Use of ZrO_2 supported on bamboo leaf ash as a heterogeneous catalyst in microwave-assisted biodiesel conversion. // Sustain Chem Pharm 2019;12:100129.

https://doi.org/10.1016/j.scp.2019.100129.

[125] Santos VP, Van Der Linden B, Chojecki A, Budroni G, Corthals S, Shibata H, et al. Mechanistic insight into the synthesis of higher alcohols from syngas: The role of K promotion on MoS_2 catalysts. // ACS Catal 2013;3:1634–7. https://doi.org/10.1021/cs4003518.

[126] Harris S, Chianelli RR. Catalysis by transition metal sulfides: A theoretical and experimental study of the relation between the synergic systems and the binary transition metal sulfides. // J Catal 1986;98:17–31. https://doi.org/10.1016/0021-9517(86)90292-7.

[127] Liu C, Virginie M, Griboval-Constant A, Khodakov AY. Potassium promotion effects in carbon nanotube supported molybdenum sulfide catalysts for carbon monoxide hydrogenation. // Catal Today 2016;261:137–45. https://doi.org/10.1016/J.CATTOD.2015.07.003.

[128] Matsumura Y, Hashimoto K, Yoshida S. Selective dehydrogenation of ethanol to acetaldehyde over silicalite-1. // J Catal 1990;122:352–61. https://doi.org/10.1016/0021-9517(90)90289-V.

[129] DeWilde JF, Czopinski CJ, Bhan A. Ethanol dehydration and dehydrogenation on γ-Al_2O_3: Mechanism of acetaldehyde formation. // ACS Catal 2014;4:4425–33. https://doi.org/10.1021/CS501239X/SUPPL_FILE/CS501239X_SI_001.PDF.

[130] Liu C, Virginie M, Griboval-Constant A, Khodakov A. Impact of potassium content on the structure of molybdenum nanophases in alumina supported catalysts and their performance in carbon monoxide hydrogenation. // Appl Catal A Gen 2015;504:565–75. https://doi.org/10.1016/j.apcata.2015.01.031.

[131] Lu J, Luo Y, He D, Xu Z, He S, Xie D, et al. An exploration into potassium (K) containing MoS_2 active phases and its transformation process over MoS_2 based materials for producing methanethiol. // Catal Today 2020;339:93–104. https://doi.org/10.1016/j.cattod.2019.01.012.

[132] Dorokhov VS, Kamorin MA, Rozhdestvenskaya NN, Kogan VM. Synthesis and conversion of alcohols over modified transition metal sulphides. // Comptes Rendus Chim 2016;19:1184–93. https://doi.org/10.1016/j.crci.2015.11.018.

[133] He Z, Que W. Molybdenum disulfide nanomaterials: Structures, properties, synthesis and recent progress on hydrogen evolution reaction. // Appl Mater Today 2016;3:23–56. https://doi.org/10.1016/j.apmt.2016.02.001.

[134] Aray Y, Rodríguez J, Coll S, Rodríguez-Arias EN, Vega D. Nature of the Lewis acid sites on molybdenum and ruthenium sulfides: An electrostatic potential study. // J Phys Chem B 2005;109:23564–70. https://doi.org/10.1021/jp054097t.

[135] Kibsgaard J, Lauritsen J V., Lægsgaard E, Clausen BS, Topsøe H, Besenbacher F. Cluster-support interactions and morphology of MoS_2 nanoclusters in a graphite-supported hydrotreating model catalyst. // J Am Chem Soc 2006;128:13950–8. https://doi.org/10.1021/ja0651106.

[136] Hensen EJM, Kooyman PJ, Van der Meer Y, Van der Kraan AM, De Beer VHJ, Van Veen JAR, et al. The relation between morphology and hydrotreating activity for supported MoS_2 particles. // J Catal 2001;199:224–35. https://doi.org/10.1006/jcat.2000.3158.

[137] Chianelli RR, Berhault G, Torres B. Unsupported transition metal sulfide catalysts: 100 years of science and application. // Catal Today 2009;147:275–86. https://doi.org/10.1016/j.cattod.2008.09.041.

[138] Torres B, Berhault G, Chianelli RR. Metal Sulfides. Encycl Catal 2010. https://doi.org/10.1002/0471227617.EOC140.PUB2.

[139] Surisetty VR, Dalai AK, Kozinski J. Influence of porous characteristics of the carbon support on alkali-modified trimetallic Co-Rh-Mo sulfided catalysts for higher alcohols synthesis from synthesis gas. // Appl Catal A Gen 2011;393:50–8. https://doi.org/10.1016/j.apcata.2010.11.026.

[140] Das D, Mishra HK, Parida KM, Dalai AK. Preparation, physico-chemical

characterization and catalytic activity of sulphated ZrO_2-TiO_2 mixed oxides. // J Mol Catal A Chem 2002;189:271–82.

[141] Zaki T. Catalytic dehydration of ethanol using transition metal oxide catalysts. // J Colloid Interface Sci 2005;284:606–13. https://doi.org/10.1016/j.jcis.2004.10.048.

[142] Leofanti G, Padovan M, Tozzola G, Venturelli B. Surface area and pore texture of catalysts. // Catal Today 1998;41:207–19. https://doi.org/10.1016/S0920-5861(98)00050-9.

[143] Roop Chand Bansal MG. ACTIVATED CARBON ADSORPTION. vol. 3. 1st ed. 6000 Broken Sound Parkway NW, Suite 300 Boca Raton, FL 33487-2742: // CRC Press, Taylor & Francis Group; 1970. https://doi.org/10.1007/BF02276400.

[144] Boahene PE, Surisetty VR, Sammynaiken R, Dalai AK. Higher alcohol synthesis using K-doped CoRhMoS_2/MWCNT catalysts: Influence of pelletization, particle size and incorporation of binders. // Top Catal 2014;57:538–49. https://doi.org/10.1007/s11244-013-0210-3.

[145] Legras A, Kondor A, Heitzmann MT, Truss RW. Inverse gas chromatography for natural fibre characterisation: Identification of the critical parameters to determine the Brunauer–Emmett–Teller specific surface area. // J Chromatogr A 2015;1425:273–9. https://doi.org/10.1016/J.CHROMA.2015.11.033.

[146] Dorokhov VS, Ishutenko DI, Nikul'Shin PA, Eliseev OL, Rozhdestvenskaya NN, Kogan VM, et al. The mechanism of synthesis gas conversion to alcohols catalyzed by transition metal sulfides. // Dokl Chem 2013;451:191–5. https://doi.org/10.1134/S0012500813070057.

[147] Osman ME, Maximov V V, Dorokhov VS, Mukhin VM, Sheshko TF, Kooyman PJ, et al. Carbon-Supported K$CoMoS_2$ for Alcohol Synthesis from Synthesis Gas. // Catalysts 2021;11:1321. https://doi.org/10.3390/catal11111321.

[148] Osman ME, Maximov V V, Dipheko TD, Sheshko TF, Cherednichenko AG, Kogan VM. Effect of textural characteristics on the catalytic performance of supported

$KCoMoS_2$ in the synthesis of higher alcohols from syngas. // Mendeleev Commun 2022;32:510–3. https://doi.org/10.1016/j.mencom.2022.07.026.

[149] Liakakou ET, Heracleous E, Triantafyllidis KS, Lemonidou AA. K-promoted NiMo catalysts supported on activated carbon for the hydrogenation reaction of CO to higher alcohols: Effect of support and active metal. // Appl Catal B Environ 2015;165:296–305. https://doi.org/10.1016/j.apcatb.2014.10.027.

[150] Surisetty VR, Dalai AK, Kozinski J. Alcohols as alternative fuels: An overview. // Appl Catal A Gen 2011;404:1–11. https://doi.org/10.1016/j.apcata.2011.07.021.

[151] Dorokhov VS, Ishutenko DI, Nikul'shin PA, Kotsareva K V., Trusova EA, Bondarenko TN, et al. Conversion of synthesis gas into alcohols on supported cobalt-molybdenum sulfide catalysts promoted with potassium. // Kinet Catal 2013;54:243–52. https://doi.org/10.1134/s0023158413020043.

[152] Dipheko TD, Maximov V V., Osman ME, Permyakov EA, Mozhaev A V., Nikulshin P, et al. Catalytic Conversion of Ethanol Over Supported $KCoMoS_2$ Catalysts for Synthesis of Oxygenated Hydrocarbons. // Fuel 2022;330:125512. https://doi.org/10.2139/ssrn.4058830.

[153] Osman ME, Dipheko TD, Maximov V V, Sheshko TF, Markova EB, Trusova EA, et al. Higher alcohols synthesis from syngas and ethanol over $KCoMoS_2$ – catalysts supported on graphene nanosheets. // Chem Eng Commun 2022. https://doi.org/10.1080/00986445.2022.2116323.

[154] Rychlicki G, Terzyk AP. Catalytic conversion of ethanol on carbon catalysts. // Carbon N Y 1994;32:265–71.

[155] Santacesaria E, Carotenuto G, Tesser R, Di Serio M. Ethanol dehydrogenation to ethyl acetate by using copper and copper chromite catalysts. // Chem Eng J 2012;179:209–20. https://doi.org/10.1016/j.cej.2011.10.043.

[156] Kogan VK, Pavel A. Nikulshin PA, Nadezhda N. Rozhdestvenskaya NN. Evolution and interlayer dynamics of active sites of promoted transition metal sulfide catalysts

under hydrodesulfurization conditions. // Fuel 2012;100:2–16. https://doi.org/10.1016/j.fuel.2011.11.016.

[157] Daage M, Chianelli RR, Ruppert AF. Structure-Function Relations in Layered Transition Metal Sulfide Catalysts. // Stud Surf Sci Catal 1993;75:571–84. https://doi.org/10.1016/S0167-2991(08)64039-2.

[158] Li M, Li H, Jiang F, Chu Y, Nie H. The relation between morphology of (Co)MoS_2 phases and selective hydrodesulfurization for CoMo catalysts. // Catal Today 2010;149:35–9. https://doi.org/10.1016/J.CATTOD.2009.03.017.

[159] Freni S, Mondello N, Cavallaro S, Cacciola G, Parmon VN, Sobyanin VA. Hydrogen production by steam reforming of ethanol: A two step process. // React Kinet Catal Lett 2000;71:143–52. https://doi.org/10.1023/A:1010311005595.

[160] Shabaker JW, Davda RR, Huber GW, Cortright RD, Dumesic JA. Aqueous-phase reforming of methanol and ethylene glycol over alumina-supported platinum catalysts. // J Catal 2003;215:344–52. https://doi.org/10.1016/S0021-9517(03)00032-0.

[161] León M, Díaz E, Ordóñez S. Ethanol catalytic condensation over Mg-Al mixed oxides derived from hydrotalcites. // Catal Today 2011;164:436–42. https://doi.org/10.1016/j.cattod.2010.10.003.

[162] Inui K, Kurabayashi T, Sato S, Ichikawa N. Effective formation of ethyl acetate from ethanol over Cu-Zn-Zr-Al-O catalyst. // J Mol Catal A Chem 2004;216:147–56. https://doi.org/10.1016/J.MOLCATA.2004.02.017.

[163] Anashkin Y V., Ishutenko DI, Maximov V V., Pimerzin AA, Kogan VM, Nikulshin PA. Effect of carrier properties on the activity of supported KCoMoS catalysts in the synthesis of alcohol from syngas. // React Kinet Mech Catal 2019;127:301–14. https://doi.org/10.1007/s11144-019-01580-2.

[164] Raybaud P. CATALYSIS BY TRANSITION METAL SULPHIDES. Paris, France: IFP Energies nouvelles; 2013.

[165] Pimerzin A, Mozhaev A, Varakin A, Maslakov K, Nikulshin P. Comparison of citric acid and glycol effects on the state of active phase species and catalytic properties of CoPMo/Al_2O_3 hydrotreating catalysts. // Applied Catal B, Environ 2017;205:93–103. https://doi.org/10.1016/j.apcatb.2016.12.022.

[166] Ishutenko D, Mozhaev A, Salnikov V, Nikulshin P. Selective hydrodesulfurization of model fluid catalytic cracking gasoline over sulfided Al_2O_3-supported Anderson heteropolyoxomolybdate-based catalysts. // React Kinet Mech Catal 2016;119:615–27. https://doi.org/10.1007/s11144-016-1083-9.

[167] Cordova A, Blanchard P, Lancelot C, Frémy G, Lamonier C. Probing the nature of the active phase of molybdenum-supported catalysts for the direct synthesis of methylmercaptan from syngas and H<inf>2</inf>S. // ACS Catal 2015;5:2966–81. https://doi.org/10.1021/cs502031f.

[168] Chen Y, Wei J, Duyar MS, Ordomsky V V., Khodakov AY, Liu J. Carbon-based catalysts for Fischer-Tropsch synthesis. Chem Soc Rev 2021;50:2337–66. https://doi.org/10.1039/d0cs00905a.

[169] Toyoda T, Minami T, Qian EW. Mixed alcohol synthesis over sulfided molybdenum-based catalysts. // Energy and Fuels 2013;27:3769–77. https://doi.org/10.1021/ef400262a.

[170] Topsøe, H., Clausen, B. S., & Massoth FE. Hydrotreating Catalysis. // vol. 11. Springer, Berlin, Heidelberg; 1996. https://doi.org/https://doi.org/10.1007/978-3-642-61040-0_1.

[171] Nikulshin PA, Tomina NN, Pimerzin AA, Kucherov A V., Kogan VM. Investigation into the effect of the intermediate carbon carrier on the catalytic activity of the HDS catalysts prepared using heteropolycompounds. // Catal Today 2010;149:82–90. https://doi.org/10.1016/j.cattod.2009.11.016.

[172] Dandekar A, Baker RTK, Vannice MA. Characterization of activated carbon, graphitized carbon fibers and synthetic diamond powder using TPD and DRIFTS.

// Carbon N Y 1998;36:1821–31. https://doi.org/10.1016/S0008-6223(98)00154-7.

[173] Li X, Feng L, Zhang L, Dadyburjor DB, Kugler EL. Alcohol Synthesis over Pre-Reduced Activated Carbon-Supported Molybdenum-Based Catalysts. // Mol 2003, Vol 8, Pages 13-30 2003;8:13–30. https://doi.org/10.3390/80100013.

[174] Li M, Li H, Jiang F, Chu Y, Nie H. The relation between morphology of (Co) MoS 2 phases and selective hydrodesulfurization for CoMo catalysts 2010;149:35–9. https://doi.org/10.1016/j.cattod.2009.03.017.

[175] Lapuerta M, Ballesteros R, Barba J, Lefebvre G, Sáez-Martínez FJ. Strategies to Introduce n-Butanol in Gasoline Blends n.d. https://doi.org/10.3390/su9040589.

[176] Alsiyabi A, Stroh S, Saha R. Investigating the effect of E30 fuel on long term vehicle performance, adaptability and economic feasibility. // Fuel 2021;306:121629. https://doi.org/10.1016/J.FUEL.2021.121629.

[177] Kaya G. Experimental comparative study on combustion, performance and emissions characteristics of ethanol-gasoline blends in a two stroke uniflow gasoline engine. // Fuel 2022;317. https://doi.org/10.1016/J.FUEL.2021.120917.

[178] Brito M, Martins F. Life cycle assessment of butanol production. // Fuel 2017;208:476–82. https://doi.org/10.1016/J.FUEL.2017.07.050.

[179] He BQ, Liu M Bin, Yuan J, Zhao H. Combustion and emission characteristics of a HCCI engine fuelled with n-butanol-gasoline blends. // Fuel 2013;108:668–74. https://doi.org/10.1016/J.FUEL.2013.02.026.

[180] Mletzko J, Ehlers S, Kather A. Comparison of natural gas combined cycle power plants with post combustion and oxyfuel technology at different CO_2 capture rates. // Energy Procedia 2016;86:2–11. https://doi.org/10.1016/J.EGYPRO.2016.01.001.

[181] Amine M, Awad EN, Ibrahim V, Barakat Y. Effect of ethyl acetate addition on phase stability, octane number and volatility criteria of ethanol-gasoline blends. // Egypt J Pet 2018;27:567–72. https://doi.org/10.1016/j.ejpe.2017.08.007.